PROTON RESONANCE SPECTROSCOPY IN ^{32}S

DUFEI FANG

Triangle Universities Nuclear Laboratory

1987

Proton Resonance Spectroscopy in ^{32}S

by

Fang Dufei

This research was performed at Triangle Unversities Nuclear Laboratory as a part of a joint collaboration between TUNL and Fudan University

Supervisors:

Prof. E. G. Bilpuch, Duke University

Prof. G. E. Mitchell, North Carolina State University

Prof. Yang Fujia, Fudan University

Dissertation submitted in partial fulfillment of the reqirements for degree of Doctor of Philosophy in the Department of Nuclear Science in the Graduate School of Fudan University

1987

ABSTRACT

Excitation functions for proton elastic scattering and for proton-induced reactions on ^{31}P were measured with the KN Van de Graaff accelerator and associated high resolution system at TUNL. Differential cross sections for $^{31}P(p, p_0)$, (p, p_1), (p, α_0) and (p, α_1) were measured in the range E_p = 1.00 to 4.01 MeV. The data were measured at five angles with an overall resolution of about 350 eV.

The measured excitation functions were analyzed with a multi-level, multi-channel R-matrix formalism. A total of 143 resonances were analyzed and the resonance parameters extracted. Resonance parameters include resonance energy, total angular momentum, parity, partial elastic and reaction widths, channel spin or orbital angular momentum mixing ratios, and for some resonances the relative signs of width amplitudes. A number of resonances have strong level-level interference effects.

Seven isobaric analog resonances were identified in ^{32}S. The proton spectroscopic factors for these resonances obtained from the present experiment are in a good agreement with spectroscopic factors from the (d, p) measurement. The resonance strengths were compared with shell model predictions. Good agreement was found when strengths for the two isospin values were summed. The elastic scattering strength functions were obtained to investigate the nucleon-nucleus dependence on isospin, spin-spin and spin-orbit interactions. The measured s-wave strength function ratio $S_{J=1}/S_{J=0}$ = 1.4. Several resonances have strong α_0 decay; for one resonance relatively strong isospin forbidden α_0 decay was observed. The thermonuclear reaction rates for the $^{28}Si(\alpha, p_0)^{31}P$ reaction were evaluated from the $^{31}P(p, \alpha_0)^{28}Si$ resonance parameters obtained in the present experiment, by using the principle of detailed balance. The reaction rates in the region T_9 = 2 – 5 are in good agreement with predictions.

ACKNOWLEDGMENTS

I would like to thank the director of TUNL, honorary professor of Fudan University, Dr. E. G. Bilpuch, for his support and encouragement during this research. I would like to thank my adviser Dr. F. J. Yang for his encouragement during my graduate studies. I am very grateful to Dr. G. E. Mitchell for his guidance and encouragement, and especially for his assistance in the preparation of this dissertation.

The assistance and patience of C. R. Westerfeldt during the course of these experiments is heartily appreciated, for his major part in the maintenance and development of the accelerator and computer systems. Special thanks are due Dr. J. R. Vanhoy, for his numerous helpful discussions and for his assistance in performing the experiment. I would like to thank Dr. J. F. Shriner Jr. for helpful discussions. The assistance and help of B. J. Warthen, W. K. Brooks, J. S. Bull, L. H. James, K. J. Keeter and B. W. Smith in every part of this experiment are deeply appreciated. Additional thanks go to K. J. Keeter for her assistance in the preparation of this dissertation.

The assistance of S. E. Edwards, R. Rummel, P. Carter and P. Mulkey in the maintenance of electronics and accelerator system is appreciated. The superior work of the machine shop, headed by A. W. Lovette, is appreciated.

I would like to thank again Dr. Bilpuch and Dr. Yang for providing me with the opportunity of promoting the relationship between TUNL and Fudan University. Special thanks go to all members of the High Resolution Research group and to Dr. J. R. Vanhoy's wife Mary Alice, for their kindness in teaching me not only physics and technology but also the great America culture.

To my family I offer my appreciation for their support and guidance through out my life. I want to thank Wu Shiming for her love and encouragement in the past two years.

This work was supported in part by the United States Department of Energy.

TABLE OF CONTENTS

LIST OF FIGURES

LIST OF TABLES

Chapter I

Introduction

The measurement of compound nuclear resonances has been an important subfield of nuclear physics since the first neutron resonances were observed. The analysis of neutron resonances led to the compound nucleus theory. Charged particle resonance studies lagged far behind neutron measurements. Although many resonances were observed in charged particle reactions, the observation and analysis of detailed structure required the development of high energy resolution beams and advanced computing facilities.

The KN Van de Graaff accelerator at Triangle Universities Nuclear Laboratory (TUNL) is devoted to study of high resolution proton resonance reactions. Early studies provided the first measurement of the fine structure of isobaric analog resonances (Keyworth, 1968). An extensive series of experiments on the fine structure of analog states was performed; these experiments are summarized in a review by Bilpuch *et al.* (1976). Later measurements emphasized statistical properties of the resonances; these are summarized in a review by Mitchell *et al.* (1985). All of these measurements were for zero spin target nuclei in the $2s$-$1d$ and $1f$-$2p$ shells.

In recent years a program investigating odd-mass target nuclei in the $2s$-$1d$ shell was initiated. Although the analysis is much more complicated than for zero spin targets, a wealth of spectroscopic information is obtained. These results are inportant for such topics as stretched states, astrophysical reaction rates, analog states, and spin-spin interactions, as well as for comparison with nuclear structure calculations. Previous targets measured include: ^{29}Si (ground state $J^{\pi} = 1/2^{+}$), ^{27}Al ($5/2^{+}$), ^{25}Mg ($5/2^{+}$), ^{39}K ($3/2^{+}$) and ^{23}Na ($3/2^{+}$).

In the present experiment, ^{32}S is studied by proton scattering from ^{31}P. The level scheme of ^{32}S is shown in figure 1.1. The structure of ^{32}S below E_x = 10.2 MeV has been studied well in previous experiments; there have been few new results since the last compilation by Endt and Van de Leun (1978). The most extensive study of the nucleus ^{32}S up to an excitation energy of 10.98 MeV was through the ^{31}P(^{3}He, d)^{32}S reaction by Kalifa *et al.* (1978). Few experimental data have

Figure 1.1 Level diagram for ^{32}S. Excitation functions are shown for the $^{32}P(p,p_0)$ and (p, α_0) reactions measured in the present experiment. Note that the $^{28}Si + \alpha$ breakup threshold is fairly low.

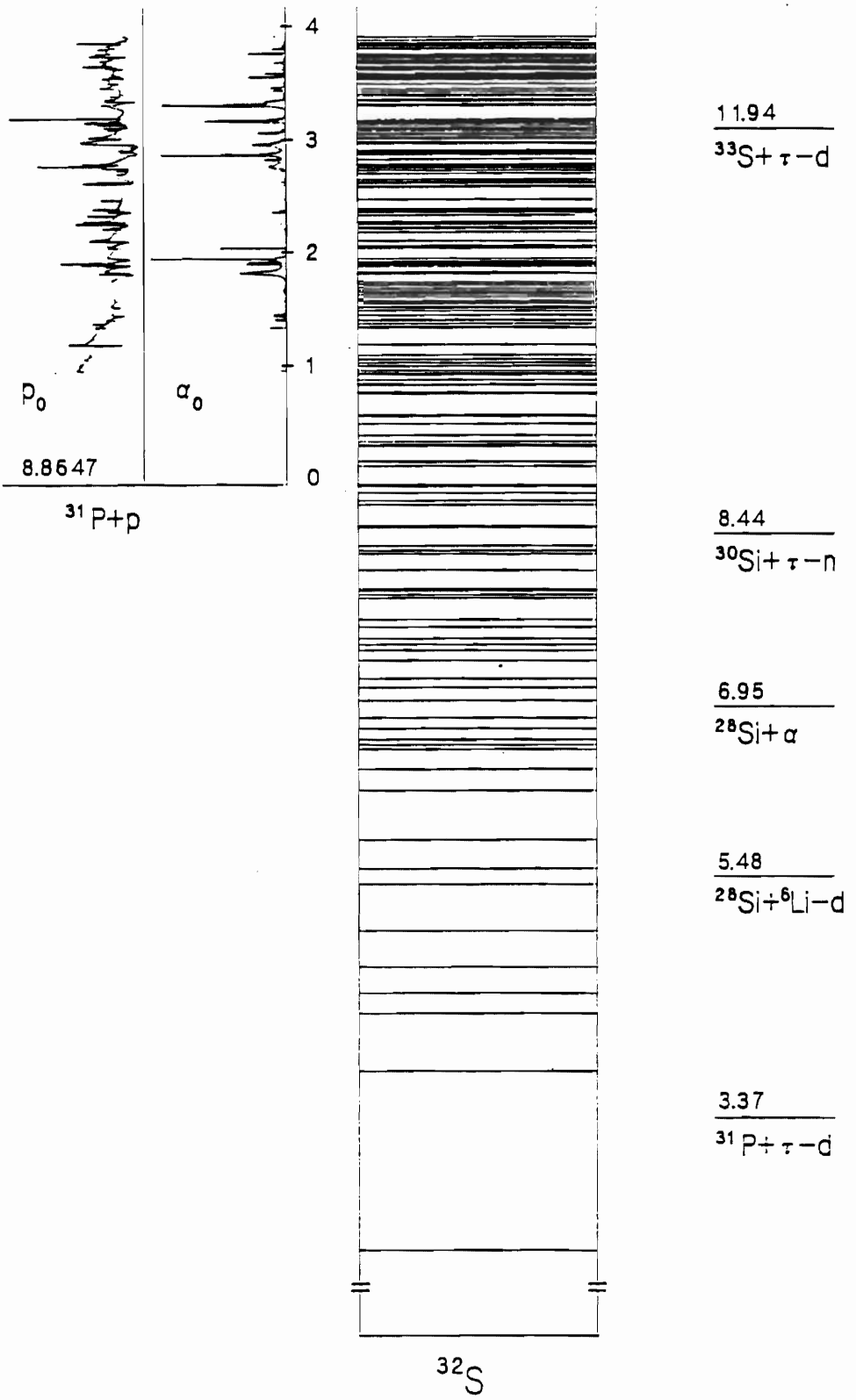
4
3
2
1
0
p_0
α_0
8.8647
$^{31}P+p$
11.94
$^{33}S+\tau-d$
8.44
$^{30}Si+\tau-n$
6.95
$^{28}Si+\alpha$
5.48
$^{28}Si+^{6}Li-d$
3.37
$^{31}P+\tau-d$
^{32}S

been measured in the region above E_x = 11.00 MeV to the $^{16}O + ^{16}O$ threshold at 16.54 MeV. Above this threshold many experiments have been performed with heavy ion reactions. The present high resolution measurement fills an important gap in the existing data.

The spectroscopic information on ^{32}S obtained in the present experiment helps to test a wide range of nuclear models and theories, including the shell model, optical model, α-cluster model and statistical model. An extensive list of theoretical references is given in Endt and Van de Leun's compilation. A shell model calculation was performed for the positive parity levels in ^{32}S up to E_x = 14.60 MeV by Kalifa *et al.* (1978). They found that in the lower energy region ($E_x \leq$ 10.98 MeV) the shell model works very well. However, there were no data to compare with these calculations at higher energies.

The study of the spin-spin interaction in the optical potential has long been an interesting topic. In principle this interaction can be investigated by comparison of *s*-wave resonance strengths for different J values, which can be obtained by proton or neutron scattering from odd-mass targets. Thus, one of the aims of the present experiment is to help establish the systematic behavior of these strength functions.

The resonances with strong alpha decay in ^{32}S are very interesting. As shown in figure 1.1, the proton separation energy is fairly high (8.864 MeV), while the $\alpha + ^{28}Si$ threshold is quite low (5.96 MeV). The $^{31}P(p, \alpha_0)$ channel is open throughout the entire energy range of the present experiment. Information about resonances with large alpha parentage provides a test for cluster models. For astrophysics, the reaction $^{28}Si(\alpha, p)^{31}P$ plays an important role during a certain phase of stellar evolution, which involves the structure of ^{32}S in the range E_x = 9.44 to 14.44 MeV. Direct (α, p) measurement is very difficult because of the huge Coulomb barrier at low incident energies for the α particles. The structure in this region can be investigated by measurement of the inverse reaction – $^{31}P(p, \alpha)^{28}Si$ – and use of the principle of detailed balance.

In this dissertation, the theoretical background for the data analysis is briefly discussed and the general formulae are presented in chapter II. The high resolution system, experimental equipment and the data acquisition procedures are described in chapter III. Analysis of resonances

in the $^{31}P(p, x)$ reactions with the R-matrix formalism is discussed in chapter IV. The experimental data and the parameters for 143 resonances are also presented in chapter IV. The new spectroscopic information for ^{32}S in the excitation energy range E_x = 9.83 to 12.74 MeV is presented and discussed in chapter V. A summary is given in chapter VI.

Chapter II

Theoretical Background

A. R-matrix Formulation

1. Introduction

In the description of nuclear reactions, the reaction mechanism can be related to the duration of the process. For example, 10^{-20}- 10^{-22} seconds is a typical nuclear transit time for a low energy nucleon. Processes such as potential scattering and stripping reactions occur on this time scale, and are referred to as direct reactions. On the other hand, the existence of narrow resonances for low energy incident nucleons indicates a much slower process. From the relation $\tau = \hbar/\Gamma$, typical times of ~ 10^{-15} seconds are obtained.

The compound nucleus mechanism was proposed by Niels Bohr (Bohr 1936) to explain the long-lived virtual nuclear states formed in low energy neutron scattering. The basic assumption is that the incident nucleon "melts" into the target nucleus after collision and the neutron energy is rapidly distributed among the nucleons in the target nucleus. The compound system undergoes many microscopic processes before one of the nucleons or composite particles gains enough energy to escape from the system. Time-dependent perturbation theory was initially used to describe this process. This treatment leads to the famous Breit-Wigner single resonance formula, which describes very well reactions proceeding through an isolated compound state. This approach is analogous to the treatment of atomic radiative decay. However, there were serious questions concerning the application of this method to nuclear reactions. Since the nuclear potential is very strong, the perturbation approximation is clearly not valid. In addition, unlike the atomic case, the appropriate form of the nuclear potential was completely unknown.

In 1938, Kapur and Peierls (1938) constructed a framework for analysis without the requirement that the form of the nuclear potential be known and without a perturbation approach. Later Wigner and Eisenbud (1947) produced a similar but more widely utilized formalism which

has come to be known as R-matrix theory. The R-matrix theory has proved more convenient for the analysis of compound nuclear processes. In 1958 Lane and Thomas published a comprehensive review. The Lane and Thomas formulation and notation have become standard and will be used in this dissertation.

In the following section the basic outline and features of R-matrix theory are presented without proof. Certain features of the theory which are most important for analysis of compound nuclear reactions (differential cross sections, level expansions, etc.) are emphasized.

2. R-matrix

To simplify the nuclear reaction problem, all nuclear processes are limited to two-body interactions: the compound nucleus is formed by an incident projectile and target nucleus, and there are only two fragments as reaction products. Radiative capture is neglected due to its small cross section compared to other processes, and no microscopic picture of the compound nucleus is considered. For a specific compound state, there are many ways to form the state as well as many decay modes. In general the process can be expressed as:

$$\begin{array}{lll} a + A & & c + C \\ b + B & X^* & d + D \\ \cdots & & \cdots \end{array} \qquad (2.1)$$

where X* denotes an excited compound nuclear state. The fragment emitted by the compound nucleus with the larger mass is called the residual nucleus. The residual nucleus can be in an excited state, in which case it will decay by emitting a particle or electromagnetic radiation. In this study only γ decay for the residual nucleus will be considered. The lifetime of the compound nucleus is so long that it "forgets" how it was formed, and only general information such as the total angular momentum J and the parity π of the state is retained. The formation of the compound nucleus and its decay are independent of each other. Each formation or decay mode is referred to as a specific particle pair.

To describe the two-body nuclear reaction, one needs a set of quantum numbers which describe the system:

1. Particle pair $\alpha = \{a_1,a_2\}$ (what kind of particles, and in what energy state),
2. Total spin of the pair $S = I_1+I_2$, where the vectors I_1 and I_2 are the spins of particles a_1 and a_2, respectively,
3. Angular momentum l of relative motion of the particle pair a_1 and a_2, and
4. Total spin of the compound state J and its projection M, and the parity π.

These particle pairs could correspond to formation (entrance) or decay (exit), i.e., the left and right hand sides of (2.1). The quantum numbers listed above could vary for a specific compound state, except for the J^{π} value. Each fixed set of quantum numbers $\{\alpha,s,l,J,M\}$ leading to or from the compound nuclear system is defined as a nuclear reaction channel and labelled as c. Energetically allowed channels for the compound state are called open channels. One can also choose an alternate quantum set such as $c = \{\alpha,s,\upsilon,l,m\}$ where υ and m are the projections of s and l. The following discussion will use the $\{\alpha,s,\upsilon,l,m\}$ scheme. The results can be transformed to the $\{\alpha,s,l,J,M\}$ scheme when necessary.

For each channel c, there is an interaction radius a_c for the particle pair $\{a_1,a_2\}$. This radius is an approximate measure of the extension of the nuclear force. When the distance r_c between a_1 and a_2 is larger than a_c, one assumes that there is no strong nuclear interaction between the particle pair $\{a_1,a_2\}$:

$$a_c = r_0(A_1^{1/3} + A_2^{1/3}),$$

where A_1 and A_2 are the masses of a_1 and a_2. The nucleon radius r_0 is independent of A_1 and A_2.

The R-matrix treatment of the compound nucleus is almost model independent. The basic idea is to divide the system configuration space into interior and exterior regions. In the exterior region the particle pair $\{a_1,a_2\}$ has only a Coulomb interaction (for charged particles). Within the channel radius a_c, each channel forms a subspace of the interior region in which particles have strong interactions. The reaction channels are normally assumed to be independent of each other, although channel-channel correlations have been observed (Mitchell *et al.* 1985). These subspaces should be orthogonal, and the space of the interior region is a direct sum of the subspaces. The surface which divides the whole space into interior and exterior regions is the sum of the channel surfaces S_c determined by the channel radius a_c:

$$\boldsymbol{S} = \sum_c \boldsymbol{s}_c \ .$$

Since one assumes there is no nuclear force in the exterior region, the description of the behavior of the pair $\{a_1,a_2\}$ in this region is relatively easy to formulate. For example, the solution to the two body Coulomb interaction problem is well known. The interactions occurring in the interior region are usually much more complicated, but their effects on the exterior region can be expressed by their boundary conditions on the surface $\boldsymbol{S}_c$. In the following section the wave functions in the exterior and interior regions will be discussed and the relationship between the two wave functions will be emphasized.

The external total wave function for the charged particle pair satisfies the equation

$$H\psi = (-\frac{\hbar^2}{2m}\nabla^2 + \frac{Z_1 Z_2 e^2}{r})\psi = E\psi \ ,$$

where m is the reduced channel mass defined as $m = m_1 m_2/(m_1+m_2)$, Z_1 and Z_2 are the charge numbers of particles a_1 and a_2, and H and E are the total Hamiltonian and energy of the system. The total energy for channel c is the sum of the internal energies of a_1 and a_2 and the relative motion energy. The wave function for channel c can be expressed for particles a_1 and a_2 by the internal wave functions $\psi_{\alpha 1 I 1 \upsilon 1}$, $\psi_{\alpha 2 I 2 \upsilon 2}$ and the relative motion wave function χ_c, where I_1 and ν_1 are the spin and its projection:

$$\psi_c = \chi_c \, \psi_{\alpha_1 I_1 \upsilon_1} \psi_{\alpha_2 I_2 \upsilon_2} \ .$$

One can also choose the channel spin quantum number $s = I_1 + I_2$ (the notation $s = s_t + s_p$ is used later in this chapter) to label the internal wave function; the wave function is the coupling of $\psi_{\alpha 1 I 1 \upsilon 1}$ and $\psi_{\alpha 2 I 2 \upsilon 2}$:

$$\psi_{\alpha s \upsilon} = \sum_{I_1 I_2 \upsilon_1 \upsilon_2} <I_1 I_2 \upsilon_1 \upsilon_2 | s \upsilon > \psi_{\alpha_1 I_1 \upsilon_1} \psi_{\alpha_2 I_2 \upsilon_2} \ .$$

The wave function $\psi_{\alpha s \upsilon}$ is defined as the channel spin wave function, where υ is the projection of channel spin s. The relative motion wave function can be separated into radial and angular parts:

$$\chi_c \sim r^{-1} u_{\alpha s l}(r) i^l Y_m^l(\Omega_\alpha) \ .$$

The wave function $u_{\alpha s l}(r)$ obeys the radial Schrodinger equation:

$$-\frac{\hbar^2}{2m}\left[\frac{d^2}{dr^2} - \frac{l(l+1)}{r^2}\right] u_{\alpha s l} + \left(\frac{Z_1 Z_2 e^2}{r^2} - E\right) u_{\alpha s l} = 0 \ . \qquad (2.2)$$

This is a well-known differential equation, and its general solutions are the regular and irregular Coulomb wave functions F_l and G_l. Any wave function satisfying (2.2) can be expanded as a superposition of these two functions. If we choose the compound system as the origin of the coordinates, the incoming and outgoing total wave functions are

$$\mathcal{I}_c = v_c^{-1/2} \phi_c I_c$$

$$\mathcal{O}_c = v_c^{-1/2} \phi_c O_c \ ,$$

where $\phi_c = i^l r^{-1} Y_l^m(\Omega_\alpha) \psi_{\alpha s l}$, v_c is the relative velocity of the particles and $v_c^{1/2}$ is the normalization factor, with

$$I_{\alpha l} = (G_l - iF_l) e^{i\omega_{\alpha l}} \qquad (2.3a)$$

$$O_{\alpha l} = (G_l + iF_l) e^{-i\omega_{\alpha l}} \ . \qquad (2.3b)$$

Note that $I_{\alpha l} = O_{\alpha l}^*$, which shows the time reversal symmetry of the system. The factor $\omega_{\alpha l}$ is the Coulomb phase shift:

$$\omega_{\alpha l} = \sum_{n=1}^{l} \tan^{-1}\left(\frac{\eta_\alpha}{n}\right) , \qquad \text{with} \qquad \eta_\alpha = \frac{Z_1 Z_2 e^2}{\hbar v} \ .$$

Some combinations of I and O on the surface $\mathcal{S}$ which separates the interior and exterior region are especially interesting:

$$L_l = \left(\frac{\rho}{O_l}\frac{dO_l}{d\rho}\right)_{r=a_c} = S_l(\rho) + iP_l(\rho) \qquad (2.4)$$

$$\Omega_l = e^{-i\phi_l} = \left(\frac{I_l}{O_l}\right)^{1/2}_{r=a_c} \ , \qquad (2.5)$$

where

$$\rho = kr = (\frac{2mE}{\hbar^2})^{1/2} r \ .$$

The quantities S_l, P_l and ϕ_l are defined as the shift function, penetrability and hard sphere phase shift, respectively. It is straightforward to obtain S, P and ϕ in terms of F and G :

$$S_l(\rho) = \frac{\rho (F_l F_l' + G_l G_l')}{F_l^2 + G_l^2} \Big|_{r=a_c} \qquad (2.6a)$$

$$P_l(\rho) = \rho (F_l^2 + G_l^2)^{-1} \Big|_{r=a_c} \qquad (2.6b)$$

$$\phi_l = \tan^{-1}(F_l / G_l) \ . \qquad (2.6c)$$

The general wave function is the superposition of the incoming and outgoing wave functions in the exterior region:

$$\psi^G = \sum_c (x_c O_c + y_c I_c) \ , \qquad (2.7)$$

where x_c and y_c are the amplitudes of the outgoing and incoming wave functions, respectively. For a given nuclear reaction system, y_c is fixed while x_c is determined by the properties of the system. The amplitude $x_{c'}$ can be expressed in terms of y_c :

$$x_{c'} = -\sum_c U_{cc'} y_c \qquad \text{or} \qquad X = -UY \ ,$$

where the second equation is in matrix form. If there is only one incident channel c, which is the usual case, one can assume $y_c = 1$ and obtain

$$\psi_c^G = I_c - \sum_{c'} U_{c'c} O_{c'} \ . \qquad (2.8)$$

The collision matrix $U_{c'c}$ gives the amplitudes of the transition probability from channel c to channel c'. The properties of the collision matrix are determined by the physical properties of the nucleus and the reaction process, and will be discussed in more detail later in this chapter. By writing out all the quantum numbers explicitly, one obtains

$$\psi_{\alpha s v}^G = \frac{i}{kr} (\frac{\pi}{\nu})^{1/2} \sum_{\alpha' s' l' m' v' l} (2l+1)^{1/2} [\delta_{cc'} I_{c'} - U_{cc'} O_{c'}] Y_{l'm'} \chi_{s'v'} \ . \qquad (2.9)$$

The general wave function for charged particle scattering can also be expressed as the superposition of distorted (by the Coulomb force) incident plane waves ψ_{inc} and outgoing spherical waves:

$$\psi^{G}_{\alpha s v} \sim \psi_{\text{inc}} + \frac{1}{r}\left(\frac{1}{v_c}\right)^{1/2} A e^{\,i(kr-\eta ln2kr+\sigma)}, \qquad (2.10)$$

where $\sigma = \omega_{\alpha l}$, and A is the scattering amplitude to be used to calculate the cross section. The problem is to express A in terms of the collision matrix U. McCarthy (1968) gives the expression for the incident wave functions in a Coulomb field, which is expanded as a sum of the partial waves:

$$\psi^{\text{inc}}_{\alpha s v} \sim \left(\frac{1}{v_c}\right)^{1/2} e^{\,i\,(kz-\eta ln(r-z)-\sigma)} \psi_{\alpha' s' l} - \frac{1}{r}\left(\frac{\pi}{v_c}\right)^{1/2} C(\theta) e^{\,i(kr-\eta ln2kr+\sigma)}, \qquad (2.11)$$

where

$$C(\theta) = (4\pi)^{-1/2} \frac{\eta}{\sin^2(\theta/2)} e^{-i2\eta Ln(\sin^2(\theta/2))}. \qquad (2.11b)$$

The incident wave function can also be expressed in terms of the functions $I_{\alpha l}$ and $O_{\alpha l}$:

$$\psi^{\text{inc}}_{\alpha s v} = \sum_{l} (2l+1)^{1/2} i^{l} (I_{\alpha l} - e^{\,2i\omega_{\alpha l}} O_{\alpha l}) Y_{l0}\, \psi_{\alpha s l}\,. \qquad (2.12)$$

By adding and subtracting (2.12) to the right hand side of equation (2.9), one can obtain an alternate expression for the general wave function

$$\psi^{G}_{\alpha s v} = \psi^{\text{inc}}_{\alpha s v} + i\frac{l}{kr}\left(\frac{\pi}{v}\right)^{1/2} \sum_{\alpha' s' l' m' v' l} (2l+1)^{1/2} [\, e^{\,2i\omega_{\alpha' l'}} \delta_{cc'} - U_{c'c}\,] O_{\alpha' l'} Y_{l' m'}\, \psi_{s' v'}\,. \qquad (2.13)$$

For large distances where the physical measurement is performed, $O_{\alpha' l'}$ can be asymptotically written as

$$O_{\alpha l} \sim e^{\,i(kr-\eta Ln2kr+\sigma)}.$$

By substituting $O_{\alpha l}$ in (2.13) and comparing with (2.10), one obtains the explicit expression for the scattering amplitude which describes the nuclear process with entrance channel $c = \{\alpha s v\}$ and exit channel $c' = \{\alpha' s' v'\}$,

$$A_{\alpha's'\nu',\alpha s\nu}(\Omega_{\alpha'}) = -\lambda\ (\pi)^{1/2} C(\theta)\delta_{c'c} + i\lambda\ (\pi)^{1/2}$$

$$\sum_{l'm'l} (2l+1)^{1/2} [\, e^{2i\omega_{\alpha' l'}} \delta_{c'c} - U_{c'c}\,] Y_{l'm'}\, \psi_{\alpha's'\nu'} \ . \quad (2.14)$$

The differential cross sections are defined as $d\sigma_{\alpha s\nu,\ \alpha's'\nu'} = |A_{\alpha's'\nu',\alpha s\nu}(\Omega_{\alpha'})|^2 d\Omega_{\alpha'}$. For an unpolarized incident projectile and an unpolarized target, the differential cross section is a sum over the s' projections ν' and an average over ν:

$$d\sigma_{\alpha s,\alpha's'} = (2s+1)^{-1} \sum_{\nu\nu'} |A_{\alpha's'\nu',\alpha s\nu}(\Omega_{\alpha'})|^2 d\Omega_{\alpha'} \ . \quad (2.15)$$

Up to this point, only the formal scattering theory which expresses the cross section in terms of the collision matrix has been considered. The collision matrix contains the dynamical information about the nucleus. In the next section the construction of the collision matrix will be discussed.

3. Collision Matrix

In the interior region, the Schrodinger equation is much more complicated to solve since the exact form of the nuclear potential is unknown. To obtain the general features of the internal wave functions, one treats the compound nuclear states as standing wave bound states with a certain boundary condition:

$$HX_\lambda = E_\lambda X_\lambda \qquad r < a_c \quad (2.16a)$$

$$\int_S (X_\lambda^* \nabla X_\lambda - X_\lambda \nabla X_\lambda^*) dS = 0 \ . \quad (2.16b)$$

In fact, the compound nuclear states are not truly standing wave bound states and eventually will decay. However, since the compound nuclear states have a long lifetime, these states can be approximately treated as standing wave bound states with the boundary conditions (2.16b). In other words, the eigenstate X_λ of the interior Hamiltonian H is defined by the boundary conditions on the surface S.

From Liouville's theorem, one knows that the equation has a complete set of orthogonal

eigenstates $\{X_\lambda\}$. Thus in the interior region the wave function for describing channel c at any particular excitation energy E can be expressed as a sum of the eigenstates $\{X_\lambda\}$:

$$\psi_c(E) = \sum_\lambda A_{\lambda c} X_\lambda \qquad \text{with} \qquad A_{\lambda c} = \int_\tau X_\lambda^* \psi_c(E) dr^3, \tag{2.17}$$

where τ is the volume of the nucleus. The Schrodinger equation is not actually solved, but it is not necessary to know the exact form of the wave functions. Instead, one only needs to know the properties of the wave functions on the surface S, at which the interior wave function will be smoothly linked with the exterior wave functions. To do this, it is convenient to define a set of orthogonal surface wave functions $\{\phi_c\}$. Thus the value of the interior wave functions and their derivatives on the surface

$$V_c = \left(\frac{\hbar^2}{2ma_c}\right)^{1/2} u_c(a_c) \tag{2.18a}$$

$$D_c = \left(\frac{a_c\hbar^2}{2m}\right)^{1/2} \left(\frac{du_c}{dr}\right)_{r=a_c} \tag{2.18b}$$

can be expanded to the surface integration of surface function $\{\phi_c\}$ and the total wave interior wave function ψ:

$$V_c = \left(\frac{\hbar^2}{2ma_c}\right)^{1/2} \int \phi_c^* \psi \, ds$$

$$D_c = \left(\frac{\hbar^2}{2ma_c}\right)^{1/2} \int_s \phi_c^* \nabla(r\psi) ds \;=\; V_c + \left(\frac{a_c\hbar^2}{2m}\right) \int_s \phi_c^* \nabla\psi \, ds \;,$$

and the wave function ψ and its derivative on the surface can be expressed as

$$\psi = \sum_c \left(\frac{2ma_c}{\hbar^2}\right) V_c \phi \tag{2.19a}$$

$$\nabla\psi = \sum_c \left(\frac{2m}{a_c\hbar^2}\right)^{1/2} (D_c - V_c)\phi_c \;. \tag{2.19b}$$

The value and derivative functions for eigenstates are very important:

$$\gamma_{\lambda c} \equiv \left(\frac{\hbar^2}{2ma_c}\right)^{1/2} \int_s \phi_c^* X_\lambda \, ds \tag{2.20a}$$

$$\delta_{\lambda c} \equiv \gamma_{\lambda c} + (\frac{a_c \hbar^2}{2m})^{1/2} \int_s \phi_c^* \nabla X_\lambda dS \ . \qquad (2.20b)$$

The amplitude $\gamma_{\lambda c}$ is directly related to the resonance partial width. The squared quantities $\gamma_{\lambda c}{}^2$ are the reduced resonance widths. The boundary condition is defined as

$$B_c \equiv \frac{D_c}{V_c} = \frac{\delta_c}{\gamma_c} \ , \qquad (2.21)$$

where B_c is the logarithmic derivative on the surface S and is energy independent. The quantity B_c is used to link the interior and exterior wave functions. When B_c is chosen to be a real number, the eigenfunction $\{X_\lambda(r)\}$ is real. Therefore from (2.20a) the reduced width $\gamma_{\lambda c}{}^2$ is an energy-independent real number with the dimensions of energy.

The wave functions in the interior region for any energy can be expanded as in (2.17). Consider the expression

$$X_\lambda^* H\psi - \psi H X_\lambda^* = (E - E_\lambda) X_\lambda^* \psi \ . \qquad (2.22)$$

Assuming that the potential part of the Hamiltonian H is self adjoint, integrating (2.22) over the volume of the interior region, and by using Green's theorem, one obtains

$$\begin{aligned}(E-E_\lambda)A_\lambda &= -\frac{\hbar^2}{2m}\int_s (X_\lambda^* \nabla\psi - \psi \nabla X_\lambda^*) ds \\ &= \sum_c (D_c - B_c V_c)\gamma_{\lambda c} \ . \end{aligned} \qquad (2.23)$$

In deriving the second step of (2.23), the relations (2.19) and (2.20) were used. Substituting A_λ into the equation (2.17), the internal wave function $\psi(E)$ is found to be

$$\psi(E) = \sum_c [\sum_\lambda \frac{X_\lambda \gamma_{\lambda c}}{E_\lambda - E}] D_c^0 \ , \qquad (2.24)$$

where $D_c{}^0 = D_c - B_c V_c$. By multiplying both sides of (2.24) by the surface function $\phi_c{}^*$ and integrating over the surface S, one obtains the relationship between V_c and $D_c{}^0$:

$$V_{c'} = \sum_c R_{cc'} D_c^0 , \quad \text{with} \quad R_{cc'} = \sum_\lambda \frac{\gamma_{\lambda c}\gamma_{\lambda c'}}{E_\lambda - E} \ . \qquad (2.25)$$

The matrix $\mathbf{R} = (R_{cc'})$ is referred to as the R matrix. Equation (2.25) is a fundamental relation which is determined by the physical properties of the nuclear system. To smoothly link the exterior wave function to the interior wave function, one calculates V_c and D_c (with formula (2.18)) for the exterior wave function ψ^{ex}, and requires that V_c and D_c satisfy the relation (2.25). Substituting the expression for the exterior wave function (2.7) into (2.18), one has

$$V_c = (\frac{\hbar}{2})^{1/2}(\rho_c^{1/2} O_c x_c + \rho_c^{-1/2} I_c y_c)$$

$$D_c = (\frac{\hbar}{2})^{1/2}(\rho_c^{1/2} O'_c x_c + \rho_c^{1/2} I'_c y_c) ,$$

where $\rho_c = k_c a_c$. Substituting V_c and D_c into relation (2.25) and expressing the equation in the matrix form, one has

$$(\rho^{-1/2}\mathbf{O}\mathbf{x} + \rho^{-1/2}\mathbf{I}\mathbf{y}) = \mathbf{R}[(\rho^{1/2}\mathbf{O}'\mathbf{x} + \rho^{1/2}\mathbf{I}'\mathbf{y}) - \mathbf{B}(\rho^{-1/2}\mathbf{O}\mathbf{x} + \rho^{-1/2}\mathbf{I}\mathbf{y})$$

or $$[\rho^{-1/2}\mathbf{O} - \mathbf{R}\rho^{1/2}(\mathbf{O}' - \rho^{-1}\mathbf{B}\mathbf{O})]\mathbf{x} = -[\rho^{-1/2}\mathbf{I} - \mathbf{R}\rho^{1/2}(\mathbf{I} - \rho^{-1}\mathbf{B}\mathbf{I})]\mathbf{y} \quad . \quad (2.26)$$

Comparing with $\mathbf{x} = -\mathbf{U}\mathbf{y}$, one obtains the relationship between the **R** matrix and the **U** matrix. In other words, the collision matrix can be expressed in terms of the **R** matrix:

$$\mathbf{U} = \Omega\mathbf{P}^{1/2}[\mathbf{1} - \mathbf{R}(\mathbf{L} - \mathbf{B})]^{-1}[\mathbf{1} - \mathbf{R}(\mathbf{L}^{*} - \mathbf{B})]\mathbf{P}^{-1/2}\Omega , \quad (2.27)$$

where Ω, **P**, **L** and **B** are diagonal matrices whose elements are defined by (2.4), (2.5), (2.6) and (2.21). Writing out expression (2.27) more explicitly, one has

$$U_{cc'} = e^{i(\omega_c+\omega_{c'}-\phi_c-\phi_{c'})}[\delta_{cc'} + 2iP_c^{1/2}\frac{1}{\mathbf{1} - \mathbf{R}(\mathbf{L}-\mathbf{B})}R_{cc'}P_{c'}^{1/2}] . \quad (2.28)$$

Consider equation (2.28) for the simplest case: single-channel and single-level elastic scattering. If $c' = c$, then

$$U_{cc} = e^{2i(\omega-\phi)}[\,1 - \frac{2iP\gamma^2}{E_\lambda - E - \gamma^2(S-B) - iP\gamma^2}] . \quad (2.29)$$

By defining the laboratory width $\Gamma \equiv 2P\gamma^2$, and the energy shift $\Delta_\lambda \equiv \gamma^2(S-B)$, the expression takes the form of the well-known Breit-Wigner formula

$$U_{cc} = e^{2i(\omega-\phi)}[\,1 - \frac{i\Gamma}{(E_\lambda - E - \Delta_\lambda) - i\Gamma/2}] .$$

From the definition of Γ, the laboratory width depends on the penetrability P and the reduced width γ^2. The reduced width is a quantity describing the resonance in the nucleus, while the penetrability is a kinematic factor determined by the barrier effects, which are contributed by the centrifugal term and the Coulomb term in the nuclear potential (see (2.2)). For s-wave neutron scattering, the width Γ is simply $2kr\gamma^2$. The resonance energy is not exactly equal to E_λ, since there is an energy shift Δ_λ. It is this energy shift which is the origin of the label shift function for S. For a single resonance, Δ_λ is approximately constant (a more detailed discussion is given in Chapter IV). For analysis convenience, Δ_λ is set to zero for each resonance.

In the derivation of the general expression (2.28), first principles were avoided in calculating energy eigenvalues and resonance widths from the nuclear potential. Instead, quantities involving the nuclear interior were written in terms of the value and derivative of the wave functions at the boundary, and these quantities were expressed in terms of the well-known exterior wave functions. Thus information about the nuclear potential is implicit in these quantities. In the comparison between theory and experiment, one measures laboratory widths and resonance energies, uses the standard nuclear radius for the matching radius a_c, chooses a convenient value for the boundary condition B_c, and fits the experimentally measured cross sections with the theoretical calculations.

4. Cross Sections

For the determination of differential cross sections, one needs to connect the theoretical calculation to the experimental observables; namely, one needs to transform the collision matrix U from the scheme $\{\alpha slmv\}$ to the scheme $\{\alpha sJlM\}$. To obtain the relationship between the two, one considers the wave function (2.8) in the exterior region in the scheme $\{\alpha sJlM\}$, which has the form

$$\psi_{JM} = I_{\alpha slM} - \sum_{\alpha' s' l'} U^{J}_{\alpha' s' l',\, \alpha s l}\, O_{\alpha' s' l' JM} \quad . \tag{2.30}$$

The wave functions in the two schemes have the relation

$$\psi_{vm} = \sum_{JM} <slvm \mid JM > \psi_{JM} \ , \qquad (2.31)$$

where $<slvm \mid JM>$ is the Clebsch-Gordon coefficient. Substituting equation (2.30) into (2.31), and comparing with equation (2.8), one has

$$U_{\alpha's'l'v'm',\ \alpha slvm} = \sum_{JM} <slvm \mid JM > U^{J}_{\alpha's'l',\ \alpha sl} \ <s'l'v'm' \mid JM > . \quad (2.32)$$

In the derivation of equation (2.32), the unitary property of Clebsch-Gordon coefficients is used. Substituting this **U** matrix transformation into the scattering amplitude expression (2.14), one obtains:

$$A_{\alpha's'v',\ \alpha sv}(\Omega_{\alpha'}) = \pi^{1/2} k_{\alpha}^{-1} [\ -C_{\alpha'}(\theta_{\alpha'})\delta_{\alpha's'v',\ \alpha sv}$$

$$+ i \sum_{JMll'm'} (2l+1)^{1/2} <slv\ 0 \mid JM > <s'l'v'm' \mid JM > T^{J}_{\alpha's'l',\ \alpha sl} \ Y^{(l')}_{m'}(\Omega_{\alpha'})] \ ,$$

where

$$T^{J}_{\alpha's'l',\ \alpha sl} = e^{2i\omega_{\alpha l'}} \delta_{\alpha's'l',\ \alpha sl} - U^{J}_{\alpha's'l',\ \alpha sl} \ .$$

To derive the expression for the differential cross section, one needs to calculate the absolute square of the amplitude (equation (2.15)). Using two sets of quantum numbers $\{J_1 M_1 l_1 l_1' m_1\}$ and $\{J_2 M_2 l_2 l_2' m_2\}$, one obtains the final result:

$$\frac{d\sigma_{\alpha s,\ \alpha' s'}}{d\Omega_{\alpha'}} = \pi k_{\alpha}^{-2} \mid C_{\alpha'}(\theta_{\alpha'}) \mid^2 \delta_{\alpha's',\ \alpha s}$$

$$+ [k_{\alpha}^{2}(2s+1)]^{-1} \sum_{L} B_L(\alpha's',\ \alpha s) P_L(cos\theta_{\alpha'})$$

$$+ \pi^{1/2} [k_{\alpha}^{2}(2s+1)]^{-1} \sum_{Jl} (2J+1)\delta_{\alpha's'l',\ \alpha sl} \mathrm{Re}[iT^{J}_{\alpha's'l',\ \alpha sl} \ C_{\alpha'}(\theta_{\alpha'}) P_L(cos\theta_{\alpha'})] \ ,$$

where

$$B_L(\alpha's',\ \alpha s) = \tfrac{1}{4}(-)^{s-s'} \sum_{J_1 J_2 l_1 l_2 l_1' l_2'} \bar{Z}(l_1 J_1 l_2 J_2,\ sL) \bar{Z}(l_1' J_1 l_2' J_2,\ s'L)$$

$$\times (T^{J_1}_{\alpha's'l_1',\ \alpha sl_1})(T^{J_2}_{\alpha's'l_2',\ \alpha sl_2})^{*} \ , \qquad (2.33)$$

and $C(\theta)$ is defined by equation (2.11b).

This multi-level multi-channel expression for the differential cross section is the foundation for the computer code MULTI6, which will be used for analysis of the experimental data. The first term of expression (2.33) is the contribution of pure Coulomb scattering, the second term represents resonance scattering and reactions, and the last term is the interference between the two, which will generate different shapes at different angles for elastic scattering (see Chapter IV). Here the summation of the coupling coefficients uses the $\bar{Z}$ coefficients of Biedenharn *et al.* (1952); the $\bar{Z}$ coefficients can be expressed in terms of Racah coefficients (Lane and Thomas (1958)).

The expression (2.28) for the collision matrix **U** involves inversion of the matrix $(\mathbf{1}-\mathbf{RL}^0)$, where $\mathbf{L}^0 = \mathbf{L}-\mathbf{B}$. The matrix dimension is the number of open channels. It is impossible to carry out the theoretical analysis for the general multi-channel and multi-level case, unless some assumptions are made. This is mainly because of the difficulty in inverting the matrix $(\mathbf{1}-\mathbf{RL}^0)$. This problem reflects the difficulty of solving many equations in many unknowns that is implied in the fundamental R-matrix relation (2.25). However, one can obtain the general features of R-matrix theory by examining simplified cases. Consider two types of simplified cases, few channels with many levels and few levels with many channels. As discussed before, for the one channel case, the collision matrix has the form of equation (2.29). For the two channel case, it is relatively easy to formulate the expression; omitting the phase factor, the components of the collision matrix are:

$$U_{11} \sim 1 + 2iP_1[R_{11} - L_2^{\,0}(R_{11}R_{22} - R_{12}^2)]d^{-1}$$

$$U_{22} \sim 1 + 2iP_2[R_{22} - L_1^{\,0}(R_{11}R_{22} - R_{12}^2)]d^{-1}$$

$$U_{12} = U_{21} \sim 2iP_1^{1/2}R_{12}P_2^{1/2}d^{-1}, \qquad (2.34)$$

where 1, 2 denote channel 1 and channel 2, and d is the determinant of the 2×2 matrix:

$$d = (1-R_{11}L_1^{\,0})(1-R_{22}L_2^{\,0}) \ .$$

For the few level, many channel case, it is usually convenient to replace the problem of inverting the matrix $(\mathbf{1}-\mathbf{RL}^0)$ by the equivalent problem of inverting another matrix; in other words, one can transform the collision matrix **U** from the form which involves the inversion of a channel matrix to

the form which involves a level matrix. Thus the dimension of the matrix to be inverted is reduced. This procedure is referred to as level expansion.

Assume the matrix ($\mathbf{1}-\mathbf{RL}^0$) can be written as

$$[(\mathbf{1}-\mathbf{RL}^0)^{-1}]_{c''c'} = \delta_{c''c'} + \sum_{\lambda\lambda'} \gamma_{\lambda c''}\gamma_{\lambda' c'} L^0_{c'} A_{\lambda\lambda'} \quad . \tag{2.35}$$

The matrix $\mathbf{A} = (A_{\lambda\lambda'})$ is the level matrix and λ is the level index. To obtain the expression for $A_{\lambda\lambda'}$, one multiplies both sides of equation (2.35) by $[\mathbf{1}-\mathbf{RL}^0]_{cc''}$, and sums over the index c'',

$$\sum_{\lambda\lambda'} (\gamma_{\lambda c}\gamma_{\lambda' c'} L^0_{c'})[\, A_{\lambda\lambda'} - \frac{\delta_{\lambda\lambda'}}{E_\lambda - E} - \sum_{\lambda'' c''} \frac{\gamma_{\lambda c''}\gamma_{\lambda'' c''} L^0_{c''} A_{\lambda''\lambda}}{E_\lambda - E}\,] = 0 \quad . \tag{2.36}$$

Since equation (2.36) is satisfied for all reduced widths $\gamma_{\lambda c}$ and $\gamma_{\lambda' c'}$, the quantity within the parentheses should be equal to zero, or

$$(A^{-1})_{\lambda\lambda'} = (E_\lambda - E)\delta_{\lambda\lambda'} - \sum_c L^0_c \gamma_{\lambda c}\gamma_{\lambda' c} \quad . \tag{2.37}$$

Using the definition of the laboratory width $\Gamma = 2P\gamma^2$, and assuming the energy shift is equal to zero, equation (2.37) can be written as

$$(A^{-1})_{\lambda\lambda'} = (E_\lambda - E)\delta_{\lambda\lambda'} - \frac{i}{2}\sum_c \Gamma^{1/2}_{\lambda c}\Gamma^{1/2}_{\lambda' c} \quad ,$$

and the collision matrix **U** can be written in terms of **A**

$$U_{cc'} = e^{-i(\phi_c + \phi_{c'})}[\delta_{cc'} + i\sum_{\lambda\lambda'} \Gamma^{1/2}_{\lambda c}\Gamma^{1/2}_{\lambda' c'} A_{\lambda\lambda'}] \quad . \tag{2.38}$$

Inversion of the matrix **A** can be performed without much difficulty by means of the usual procedures in the case of one, two and three levels. In the present experiment, since the target spin is non-zero, there are at least two channels possible for each level. Thus it is very convenient to analyze single resonances with the level expansion. For a single resonance, one has $\lambda = \lambda' = 1$, and

$$A = 1/\,[(E_\lambda - E) - \frac{i}{2}\Gamma_\lambda\,] \,,$$

where $\Gamma_\lambda = \Sigma_c \Gamma_{\lambda c}$ is the total width of the resonance. Substituting A into equation (2.35) and using

(2.38), one obtains the resonance term of the differential cross section for the single level case:

$$\left(\frac{d\sigma_{\alpha,\alpha'}}{d\Omega_{\alpha'}}\right) = \frac{1}{4k_{\alpha'}^2(2s_t+1)(2s_p+1)} \sum_{ss'l_1l_1'l_2l_2'L} (-)^{s-s'} \frac{\Gamma^{1/2}_{\alpha s l_1}\Gamma^{1/2}_{\alpha' s l_1'}\Gamma^{1/2}_{\alpha s l_2}\Gamma^{1/2}_{\alpha' s' l_2'}}{[(E_\lambda - E)^2 + (\Gamma_\lambda/2)^2]} \cos(\delta)$$

$$\times \bar{Z}(l_1 J l_2 J, sL)\bar{Z}(l_1' J l_2' J, s'L) P_L(\cos\theta_{\alpha'}) \ , \qquad (2.39)$$

where $\delta = \omega_{l1}+\omega_{l1'}-\omega_{l2}-\omega_{l2'}$, and the ω_l are the sum of the Coulomb and nuclear hard sphere phases and s_p and s_t are the spin of incident particle and target, respectively. For any single value of channel spin the sum over l values is coherent, while the sum over channel spins s and s' is incoherent.

For the two level case, one has:

$$A_{11} = \varepsilon_2/D \qquad A_{22} = \varepsilon_1/D$$

$$A_{12} = A_{21} = \xi_{12}/D \qquad D = \varepsilon_1\varepsilon_2 - \xi_{12}^2 \ ,$$

where $\varepsilon_\lambda = (E_\lambda - E) - i\Gamma_\lambda/2$, $\xi_{\lambda\mu} = i\Gamma_{\lambda\mu}/2 = i\sum_c P_c \gamma_{\lambda c}\gamma_{\mu c}$. The two level, many channel case will be used to study level-level interference effects in Chapter IV.

For the case of three or more levels, one can make a diagonal level approximation under some circumstances which are of practical interest; then the inversion of matrix **A** is trivial. However, without such an approximation the level expansion procedure is not simple and may be even more difficult than the usual channel formulation.

B. Angular Distributions of Reaction Products

For an isolated state of the compound nucleus, the angular distributions of the various decay channels contain both dynamical and geometrical information about the nucleus. The angular correlation method has long been one of the most powerful tools in nuclear spectroscopy studies.

The formation of the compound nucleus involves the vector coupling of three angular momenta: the spin of the target (s_t) and of incident particle (s_p) and the orbital angular momentum (l) associated with the relative motion between target and projectile. There are two conventional

ways of combining these vectors. One is the channel spin representation in which the spins of the target and incident particle are coupled first:

$$s = s_t + s_p \, .$$

The vector s is then combined with the orbital angular momentum l to form the spin J of the compound nucleus:

$$J = s + l \, .$$

The advantage of the channel spin (or LS coupling) scheme is that if the target and projectile are unpolarized, then the different values of s will contribute incoherently to the angular distribution. In the exit channel, vector decoupling ($J = s' + l'$) is treated in the same manner, except that the residual nucleus may be in an excited state.

The alternative coupling scheme is referred to as the particle representation. In this scheme the spins of the incoming and outgoing particles are combined with their corresponding orbital angular momenta to form the spin of the resonance:

$$j = s_p + l$$

$$J = s_t + j \, .$$

The two coupling schemes are shown schematically in figure 2.1. These two coupling schemes represent the same physical situation in two different representations. The physics results are the same, but there may be reasons for preferring one or the other representation in different situations. In this dissertation the channel spin representation is used unless specified otherwise.

For an angular distribution measurement for decay from a single resonance, one can use the expression (2.39) to calculate the correlation function:

$$W(\theta) \propto a_0 P_0(\cos\theta) + a_1 P_1(\cos\theta) + a_2 P_2(\cos\theta) + \ldots \, ,$$

where P_L is the L^{th} Legendre polynomial, and a_L is the sum of the $\bar{Z}$ coefficients and partial width products in expression (2.39) for the fixed L value. From the symmetry properties of the $\bar{Z}$ coefficients one can easily prove that all the a_L values for odd L are zero.

A more precise and straightforward method for calculating the angular distribution was described by Ferguson (1965). This method is particularly useful in the compound nuclear case with subsequent residual nucleus decay. In this method the nuclear system is assumed to be in a

Figure 2.1 Angular momentum coupling scheme in the channel spin representation and the particle representation.

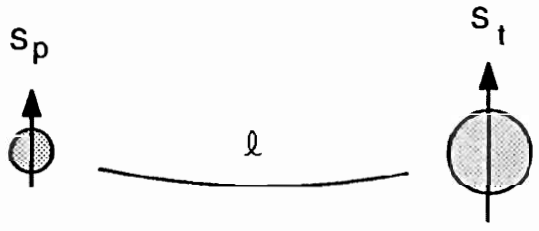

$$\vec{J} = \vec{s_t} + \vec{s_p} + \vec{\ell}$$

Channel Spin Representation

$$\vec{J} = (\vec{s_t} + \vec{s_p}) + \vec{\ell}$$

$$= \vec{S} + \vec{L}$$

Particle Representation

$$\vec{J} = \vec{s_t} + (\vec{s_p} + \vec{\ell})$$

$$= \vec{s} + \vec{j}$$

mixed state which can be described by a density matrix ρ. The expectation value of an operator O corresponding to a physical measurement of the system is

$$<O> = \mathrm{Tr}(O\rho) \ .$$

The operator for the angular correlation measurement specifies the parameters for the detection of the outgoing particles or radiation. Such an operator can be defined as the efficiency operator ε (Roman 1965). Thus the probability that an event will be recorded in the detector is

$$W = \mathrm{Tr}(\varepsilon\rho) \ .$$

Now the problem is to find a set of appropriate basis vectors for deriving the angular correlation function. It is usually convenient to derive this with the irreducible tensor approach. One can construct the density matrix by using eigenvectors $|a\alpha>$ of the angular momentum a, so that a set of irreducible tensors with parameters $\rho_{kn}(a_1a_2)$ can be defined by

$$\rho_{kn}(a_1a_2) = \sum_{\alpha_1\alpha_2} (-)^{a_2-\alpha_2}(a_1\alpha_1, a_2-\alpha_2 | kn)<a_1\alpha_1| \rho |a_2\alpha_2> \ , \qquad (2.40)$$

where $(a_1\alpha_1, a_2-\alpha_2 | kn)$ are Clebsch-Gordan coefficients, and $k = a_1-a_2$. For fixed value of k, a_1 and a_2, the set of $\rho_{kn}(a_1a_2)$ which has $(2k+1)$ components is referred to as a density tensor. An efficiency tensor can be constructed from the efficiency matrix in the same way. Thus the angular correlation function W can be expressed as

$$\begin{aligned} W &= \mathrm{Tr}(\rho\varepsilon) \\ &= \sum_{a_1\alpha_1a_2\alpha_2} <a_1\alpha_1|\rho|a_2\alpha_2><a_1\alpha_1|\varepsilon|a_2\alpha_2>^* \\ &= \sum_{a_1a_2kn} \rho_{kn}(a_1a_2)\varepsilon^*_{kn}(a_1a_2) \ . \qquad (2.41) \end{aligned}$$

In deriving the second step of (2.41) the symmetry properties of Clebsch-Gordan coefficients are used.

Expression (2.41) is the basic equation for the angular correlation. However, in practice the intermediate state cannot be observed directly; one always measures the reaction products in the laboratory frame, and the efficiency tensors (or matrices) are always associated with the measurement. Before deriving the angular correlation expression for the measurement, one needs

to label each stage of the successive nuclear processes. The three step nuclear reaction process can be illustrated schematically as in figure 2.2. A target nucleus **A** with spin s_t is bombarded by a beam of particles with spin s_p. The channel spin is given by $s = s_p + s_t$. Particles with orbital angular momentum l are absorbed to form the intermediate state **B** of spin J. The intermediate state breaks up by emitting particles or gamma rays with orbital angular momentum l' and leaves the system in exit channel spin s'. If the outgoing particles have spin s_p' and the residual nucleus **C** has spin s_t', then $s' = s_p' + s_t'$. The residual nucleus then decays electromagnetically (2^Lth pole) to the final state of spin **D**. If the experiment does not measure the spin of the residual nucleus **C** and spin of the emitted particle s_p'; and does not measure the electromagnetic radiation, then only the exit channel spin s' and angular momentum l' are involved. If the density and efficiency tensors are constructed in the laboratory coordinate system, the angular correlation function can be written as

$$W = \sum \rho_{k_s n_s}(s_1's_2')\rho_{k_l n_{l'}}(l_1'l_2')\varepsilon^{*}_{k_s n_{s'}}(s_1's_2')\varepsilon^{*}_{k_l n_{l'}}(l_1'l_2') \quad , \qquad (2.42)$$

where the summation is over $s'_1 s'_2 l'_1 l'_2 k_s n_s k_{l'} n_{l'}$, and the two efficiency tensors represent the detection of the exit channel spin and orbital angular momentum of the emitted particles, respectively.

To derive the relationship between the density tensors of the final state and the intermediate state, one first considers the purely geometric case in the exit channel: $J = s' + l'$. The coupled basis vectors $\{|JM>\}$ and the uncoupled basis vectors $\{|s'v'l'm'>\}$ are connected by

$$<s'v'l'm'| = \sum_M (s'v'l'm'|JM)<JM| \quad , \qquad (2.43)$$

where v', m' and M are the projections of s', l' and J. Tensors constructed by the definition (2.40) in these two bases have a relationship which is the well-known Wigner-Eckart theorem:

Figure 2.2 Angular momentum relations for a three step nuclear process in the channel spin representation.

Angular momentum relations for compound nuclear reactions

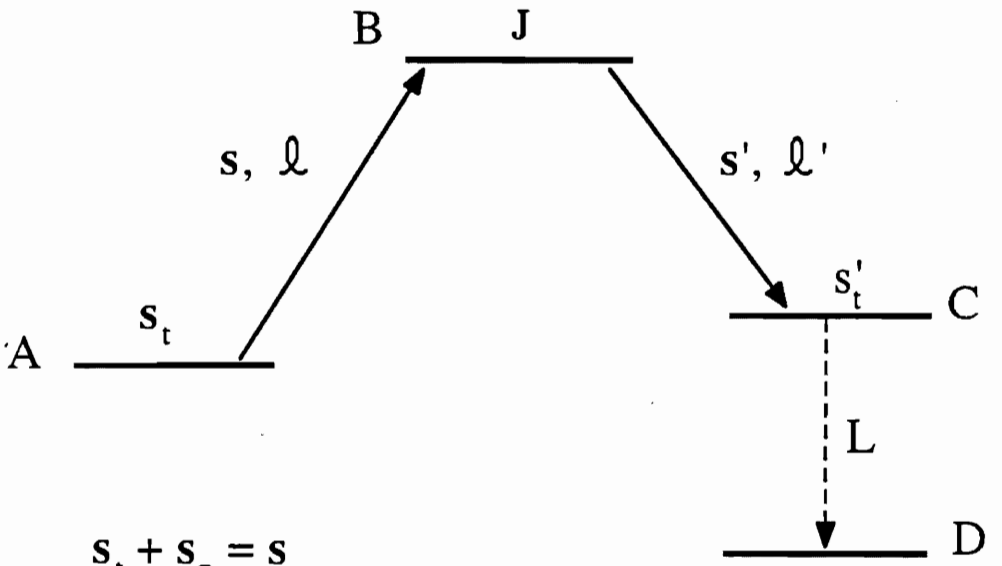

$$\mathbf{s}_t + \mathbf{s}_p = \mathbf{s}$$

$$\mathbf{s} + \boldsymbol{\ell} = \mathbf{J}$$

$$\mathbf{J} = \mathbf{s}' + \boldsymbol{\ell}'$$

$$\mathbf{s}' = \mathbf{s}_t' + \mathbf{s}_p'$$

$$\mathbf{s}_t' = \mathbf{D} + \mathbf{L}$$

$$T_{k_J n_J}(J_1 J_2) = \sum_{k_s n_{s'} k_{l'} n_{l'}} T_{k_s n_{s'}}(s'_1 s'_2) T_{k_{l'} n_{l'}}(l'_1 l'_2)(k_s n_{s'}, k_{l'} n_{l'} | k_J n_J)$$

$$\hat{J}_1 \hat{J}_2 \hat{k}_s \hat{k}_{l'} \begin{Bmatrix} s'_1 & l'_1 & J_1 \\ s'_2 & l'_2 & J_2 \\ k_{s'} & k_{l'} & k_J \end{Bmatrix}, \qquad (2.44)$$

where the quantity in the braces is a 9-j symbol, and $\hat{e} = (2e+1)$, $e = J_1, J_2$ ..., etc. This equation is basic to the theory. Since transformation (2.44) is real and unitary, the inverse of expression (2.44) is simply

$$T_{k_s n_{s'}}(s'_1 s'_2) T_{k_{l'} n_{l'}}(l'_1 l'_2) = \sum_{J_1 J_2 k_J n_J} T_{k_J n_J}(J_1 J_2)(k_s n_{s'}, k_{l'} n_{l'} | k_J n_J)$$

$$\hat{J}_1 \hat{J}_2 \hat{k}_s \hat{k}_{l'} \begin{Bmatrix} s'_1 & l'_1 & J_1 \\ s'_2 & l'_2 & J_2 \\ k_{s'} & k_{l'} & k_J \end{Bmatrix}. \qquad (2.45)$$

Now suppose the intermediate state undergoes a dynamical change by the emission of a particle or a photon. The nuclear process can be described as follows: under the perturbation of H_{int}, the system transforms from the initial state $<JM|$ to the final state $<s'v'l'm'|$. From standard quantum mechanics, one has

$$<s'v'l'm'| = \sum_M (s'v'l'm'|H_{\text{int}}|JM)<JM| \ . \qquad (2.46)$$

Another Wigner-Eckart theorem states that the interaction term in equation (2.46) can be written as

$$(s'v'l'm'|H_{\text{int}}|JM) = (s'v'l'm'|JM)<s'||l'||J>,$$

where $<s'||l'||J>$ is the reduced matrix element of the interaction term, which is independent of M, v' and m'. Thus one obtains

$$<s'v'l'm'| = <s'||l'||J> \sum_M (s'v'l'm'|JM)<JM| \ . \qquad (2.47)$$

Note that relations (2.42) and (2.47) differ only by a factor. It can be proven that the density tensors of the intermediate state B, exit channel spin state s' and the emitted particle l' have the relationship (2.45) with a dynamical modification:

$$T_{k_s n_{s'}}(s'_1 s'_2) T_{k_l n_{l'}}(l'_1 l'_2) = \sum_{J_1 J_2 k_J n_J} T_{k_J n_J}(J_1 J_2)(k_s n_{s'}, k_l n_{l'} \mid k_J n_J)$$

$$\hat{J}_1 \hat{J}_2 \hat{k}_s \hat{k}_{l'} \begin{Bmatrix} s'_1 & l'_1 & J_1 \\ s'_2 & l'_2 & J_2 \\ k_{s'} & k_{l'} & k_J \end{Bmatrix} \langle s'_1 \| l'_1 \| J_1 \rangle \langle s'_2 \| l'_2 \| J_2 \rangle^* \quad , \quad (2.48)$$

where

$$\hat{J}_2 \langle s'_2 \| l'_2 \| J_2 \rangle^* = (-1)^{s'_2 - J_2 - l'_2} \hat{s}'_2 \langle s'_2 \| l'_2 \| J_2 \rangle \quad .$$

Suppose the intermediate state **B** is appropriately prepared such that the density tensor $\rho_{kJnJ}(J_1 J_2)$ can be obtained. By applying the relation (2.48) to (2.42), one obtains:

$$W = \sum \rho_{k_J n_J}(J_1 J_2) \varepsilon^*_{k_{s'} n_{s'}}(s'_1 s'_2) \varepsilon^*_{k_{l'} n_{l'}} (l'_1 l'_2)(k_s n_{s'}, k_{l'} n_{l'} \mid k_J n_J)$$

$$\hat{J}_1 \hat{J}_2 \hat{k}_s \hat{k}_{l'} \begin{Bmatrix} s'_1 & l'_1 & J_1 \\ s'_2 & l'_2 & J_2 \\ k_{s'} & k_{l'} & k_J \end{Bmatrix} \langle s'_1 \| l'_1 \| J_1 \rangle \langle s'_2 \| l'_2 \| J_2 \rangle^* \quad , \quad (2.49)$$

where the reduced matrix elements $\langle s'_1 \| l'_1 \| J_1 \rangle$ and $\langle s'_2 \| l'_2 \| J_2 \rangle^*$ are related to the exit channel width of the compound nuclear state.

The density tensor for the intermediate state can be obtained in a similar way: represent the density tensor $\rho_{kJnJ}(J_1 J_2)$ in terms of density tensors of the incident particle, target and the orbital angular momentum of the incident particles. Formula (2.44) will be used twice, once for the channel spin coupling for the incident particle and the target spin, which is the purely geometric case, and the other for the intermediate state formation which has the dynamical modification. Again, there will be two reduced matrix elements $\langle J_1 \| l_1 \| s_1 \rangle$ and $\langle J_2 \| l_2 \| s_2 \rangle^*$, which are related to the entrance widths. Thus one obtains the final results:

$$W = \sum \rho_{k_s n_s}(s_1 s_2) \rho_{k_l n_l}(l_1 l_2) \varepsilon^*_{k_{s'} n_{s'}}(s'_1 s'_2) \varepsilon^*_{k_{l'} n_{l'}} (l'_1 l'_2)(k_s n_{s'}, k_l n_s \mid k_J n_J)(k_{s'} n_{s'}, k_{l'} n_{l'} \mid k_J n_J)$$

$$\hat{J}_1 \hat{J}_2 \hat{k}_s \hat{k}_l \hat{J}_1 \hat{J}_2 \hat{k}_{s'} \hat{k}_{l'} \begin{Bmatrix} s_1 & l_1 & J_1 \\ s_2 & l_2 & J_2 \\ k_s & k_l & k_J \end{Bmatrix} \begin{Bmatrix} s'_1 & l'_1 & J_1 \\ s'_2 & l'_2 & J_2 \\ k_{s'} & k_{l'} & k_J \end{Bmatrix}$$

$$<s_1 | l_1 \| J_1 ><s_2 | l_2 \| J_2 >^{*} <s'_1 | l'_1 \| J_2 ><s'_2 | l'_2 \| J_2 >^{*} . \qquad (2.50)$$

In practice, for many cases the incident particles and the target are not polarized, and the exit channel spin s' is not measured. In the present experiment, only the emitted particles from the intermediate state are observed. By choosing an appropriate coordinate system, one can calculate the density and efficiency tensors which are associated with the experimental arrangement (incident beam and target) and the measurement (the arrangement of the detectors). These results are also discussed by Vanhoy (1986). Since the incident particle and the target are not polarized, and exit channel spin is not measured, equation (2.50) will be greatly simplified. Table 2.1 lists those tensors which are needed to calculate the (p, p') and (p, α) angular distributions.

For a nuclear reaction of the type described above, the reduced matrix elements which cause the transition in the successive nuclear processes have the following relation with the scattering matrix U (Ferguson, 1965)

$$<sIJ | U | s'I'J > \sim <J \| l | s ><s' | l' \| J > ,$$

and for a single resonance with total angular momentum J the left hand side of the above relation can be expressed as (Biedenharn (1960))

$$<s_1 l_1 J_1 | U | s'_1 l'_1 J_1 > \sim \frac{i\Gamma^{1/2}_{s_1 l_1}\Gamma^{1/2}_{s'_1 l'_1}}{E_0 - E - i\Gamma/2} e^{i(\omega_{l_1} + \omega_{l'_1})} .$$

Substituting this expression and the tensors listed in Table 2.1 into equation (2.50), and using the definition of Z coefficients, one obtains the angular correlation function

$$W(\theta) = \sum (-)^{s+s'-2J} \left(\frac{1}{4\pi \hat{s}_p \hat{s}_t} \right)^2 \frac{\Gamma^{1/2}_{sl_1}\Gamma^{1/2}_{sl_2}\Gamma^{1/2}_{s'l'_1}\Gamma^{1/2}_{s'l'_2}}{[(E_0 - E)^2 + (\Gamma/2)^2]} \cos(\delta)$$

$$\bar{Z}(l_1 J l_2 J, sk)\bar{Z}(l'_1 J l'_2 J, s'k) P_k(\cos\theta) , \qquad (2.51)$$

where δ is the same as in equation (2.39).

For experiments involving measurement of electromagnetic transitions, one can follow the same procedure to obtain the expression for the angular correlation function $W(\theta)$.

Table 2.1 Density and Efficiency Tensors

Density tensors:

unpolarized incident particle of spin s_p

$$\rho_{kn}(s_p s_p') = \delta_{k0}\delta_{n0}\delta_{s_p s_p'}/\hat{s_p}$$

unpolarized target of spin s_t

$$\rho_{kn}(s_t s_t') = \delta_{k0}\delta_{n0}\delta_{s_t\, s_t'}/\hat{s}_t$$

entrance channel spin $s = s_t + s_p$ (unpolarized)

$$\rho_{kn}(s_1 s_2) = \delta_{k0}\delta_{n0}\delta_{s_1 s_2}\hat{s}(\hat{s_p}\hat{s_t})^{-2}$$

entrance orbital angular momentum l

$$\rho_{kn}(l_1 l_1') = (-)^{l_1'}\hat{l_1}\,\hat{l_1}'(l_1 0 l_1' 0 \mid k\ 0)\delta_{n0}/(4\pi)$$

Efficiency tensors:

emitted particle with l' in the direction of $\Omega(\theta, \phi)$

$$\varepsilon_{kn}(l'_1 l'_2) = \left(\frac{1}{4\pi}\right)^{1/2}(-)^{l'_2}\frac{\hat{l'_1}\hat{l'_2}}{\hat{k}}(l'_1 0 l'_2 0 \mid k\ 0)Y^{*}_{kn}(\theta, \phi)$$

unobserved exit channel spin s'

$$\varepsilon_{kn}(s'_1 s'_2) = \hat{s}\delta_{k0}\delta_{n0}\delta_{s'_1 s'_2}$$

C. Nucleon Transfer Reaction

The R-matrix theory is a formal theory of the compound nucleus. It does not deal with the dynamics of the interior region. For example, it can not predict the reduced widths of the resonances. To study the compound nuclear process microscopically, one needs to construct a specific model and the corresponding Hamiltonian. A nucleus may be characterized by a Hamiltonian of a single particle shell model which has the form

$$H = K + H_{\text{int}}$$

where K is the kinetic energy of the particle, H_{int} includes the nuclear potential V_N, Coulomb potential V_C, residual two body interaction term H_R and the spin-orbit interaction term H_S:

$$H_{\text{int}} = V_N + V_C + H_R + H_S \ .$$

In order to determine the eigenvalues and the eigenvectors of the Hamiltonian, that is, the energy levels and the corresponding wave functions, one needs to express the Hamiltonian in a matrix representation and diagonalize it. If a representation is found in which H is diagonal, the problem is obviously solved. The single particle shell model can provide a representation in which H is approximately diagonal. The shell model Hamiltonian is often defined to exclude the spin-orbit coupling and residual interaction term, that is

$$H_0 = K + H' ,$$

where $H' = V_N + V_C$. The eigenstates of H_0 are a complete orthogonal set of the antisymmetric functions which form the basis of the shell model representation.

Several operators commute with H. They represent the observables which are conserved, in other words, the corresponding quantum numbers are good. Among these the most important are the total angular momentum J and parity π. Usually the isospin T is approximately a good quantum number. Thus the matrix for the total Hamiltonian is the direct sum of the submatrices $K^{J\pi T}$, each corresponding to a set of values of J, π, and T, and these can be diagonalized separately. Nucleons in the same subshell are equivalent. This means that they have the same value of n, l, and j, if the particle representation is used (see the previous section of this chapter). A definite set of nlj is referred to as a configuration.

In the extreme single particle model, the compound nucleus (or the excited state) is formed by putting a particle in one of the unoccupied orbits. If the final nucleus can be well described by the single particle model, one can investigate the single particle state by adding a nucleon to a target nucleus, that is by nucleon transfer reactions such as (d, p).

To describe the single particle + nucleus system, one can choose a representation in which the state vector $|m>$ of the basis is given by

$$|m> = A\phi_i(x_i)\psi_\alpha(\xi_i),$$

where x_i includes all the coordinates of the single particle i, such as spin and isospin, and ξ_i includes all the coordinates of the other particles, ϕ_i is the single particle wave function and ψ_α is the "core" wave function and A is the antisymmetrization operator. This representation is often referred to as the weak coupling representation (Macfarlane and French, 1960). In practice, the dimension of the basis $\{|m>\}$ is chosen to be finite, and the submatrices $K^{J\pi T}$ are treated one at a time. The angular momentum and the isospin of ϕ_i and ψ_α are coupled such that the basis $\{|m>\}$ has the values J, π, and T.

The core state ψ_α is related to the states of the core nucleus, which is the nucleus [A] in the (d, p) reaction

$$[A](d, p)[A+1],$$

where the nuclei are specified by their mass numbers. The core may be described by a specific model. Usually the ground state state eigenfunction of [A] is chosen to be the core ground state function ψ_0. The other core wave functions for $\alpha \neq 0$ which describe the core excitation are linear combinations of the eigenstates of [A].

Consider an alternate representation in which the basis vectors $\{|\rho>\}$ are the observed (or physical) states in the [A+1] system. The state ρ can be simply made by adding a single particle to the nucleus [A] via (d, p) or (d, n). The basis $\{|\rho>\}$ is not necessarily equal to the basis $\{|m>\}$. In general, they are related by the unitary operator U:

$$|\rho> = U|m>.$$

Thus the vector $|\rho>$ can be considered as the eigenvector of the transformed Hamiltonian $H'=UHU^{-1}$. The matrix elements of H' are diagonal in the $|\rho>$ representation:

$$<\sigma|UH'U^{-1}|\rho> = E_\rho \delta_{\rho\sigma}$$

$$= <n|U^\dagger UH'U^{-1}U|m> .$$

This is identical to H in the original representation $|m>$. The matrix element of U in the $|m>$ representation is:

$$<n|U|m> = <n|\rho> . \tag{2.52}$$

Thus the eigenstate $|\rho>$ can be expressed in terms of $|m>$:

$$|\rho> = \sum_m |m><m|\rho>$$

$$= \sum_{i,\alpha} t_{i\alpha}^{(\rho)} A\phi_i(x_i)\psi_\alpha(\xi_i) , \tag{2.53}$$

where $t_{i\alpha}^{(\rho)}$ is the element of the U matrix in (2.52). Using completeness for the eigenstates, one obtains

$$\sum_\rho <m|\rho><\rho|m> \equiv \sum_\rho |t_{i\alpha}^{(\rho)}|^2 = 1 , \tag{2.54}$$

for all the sets of indices $i\alpha$.

The observed state ρ of the nucleus [A+1] is referred to as a single particle state if the expansion (2.53) is dominated by a single term $t_{i\alpha}^{(\rho)}$. It is particularly important for the case $\alpha = 0$, in which the state ρ can be quite well described by the single particle wave function ϕ_i. The most important quantity for nuclear spectroscopy (the spectroscopic factor) is defined as $S^\rho = |t_{i0}^{(\rho)}|^2$. Assuming the core nucleus remains in the ground state in the nucleon transfer reaction (referred to as an inert core), and using the distorted wave Born approximation (DWBA) (Tobocman, 1961) for the theoretical calculation, the magnitude of the (d, p) reaction cross section is found to be proportional to the spectroscopic factor:

$$\left(\frac{d\sigma}{d\Omega}\right) = \frac{\mu_d\mu_p}{2\pi h^2}\frac{k_p}{k_d}\frac{2I_F+1}{2I_C+1}\sum_{M_C M_F m_p m_d lsj} S_{lsj}^{\rho}\ \frac{2va_s^2}{2s+1}\ |T_{lsj}|^2 , \tag{2.55}$$

where T_{lsj} is the amplitude for stripping a neutron into the orbit $(n)lsj$.

The factor $S_{lsj}^{(\rho)}$ in (2.55) is the spectroscopic factor for the final nucleus F = [A+1], which describes the probability of the nucleus F in its final state containing the core in its ground state and the particle n in the single particle state ϕ_{nlsj}. Another interpretation of the spectroscopic factor is

that it tells how much a particular stripping reaction is like inert core stripping. The spectroscopic factor can be obtained from the reduced width θ^2, which is determined by the overlap integral <[A+1]|[A]>; this overlap integral can be calculated with a proper nuclear structure model such as the shell model. The reduced width θ^2, similar to γ^2 in the R-matrix theory, is a property of the nucleus [A+1]; it should be independent of the experimental conditions. For a single particle reaction, the reduced width is determined by the square of the wave function ϕ_i, and is often referred to as the single particle reduced width θ_0^2. One has the relation

$$\theta^2 = S^\rho \theta_0^2 ,$$

where θ^2 is the observed reduced width for the state ρ. If the state ρ is an exact single particle state, then S^ρ is unity; if S^ρ is not unity, then several states ρ contain the wave function ϕ_i, in other words, the single particle state $|m>$ is fragmented into several states of the nucleus [A+1]. If the number of the states ρ is small, the requirement of the theoretical calculation (weak coupling) will be quite well satisfied.

An extremely useful relationship is the sum rule obtained from relation (2.54)

$$\sum_\rho S^\rho (\phi_i) = 1 .$$

This means that if there exists a single particle state, its whole strength can be traced back in the states ρ which are observed. For a nucleus whose spectroscopy is well understood, the sum rule may also be used to check the reaction theories. For cases in which the single particle state is distributed over only a few final states ρ, the energy of the single particle state ϕ_i plays a role as "center of gravity" of the energy E_ρ, where the states are weighted according to their strengths in the (d, p) reaction.

Chapter III

Experimental Procedure and Data Acquisition

A. KN Van de Graaff Accelerator and High Resolution System

This experiment was performed with the Triangle Universities Nuclear Laboratory (TUNL) KN Van de Graaff accelerator together with a high resolution feed back system. The laboratory arrangement is shown schematically in figure 3.1. The system provides an overall energy resolution of 300-400 eV for thin solid targets in the range of proton beam energies E_p = 1.00 - 4.00 MeV. The short term energy stability is about 10 eV at 0.992 MeV; the long term energy drift is presently ~ 60eV/hour at E_p = 2.045 MeV. The system has been improved and modified extensively since the original version (Parks 1958), and recently has been described in detail by Westerfeldt (1986). In this dissertation only a brief description of the system will be given.

The RF ion source in the terminal of the accelerator produces the hydrogen ion H^+ and the molecular ion HH^+. These ions are accelerated and pass into an analyzing magnet. The proton H^+ beam is bent 25° into the beam leg and passes through the steering and quadrupole magnet and collimators into the 43.2 cm diameter scattering chamber, while the HH^+ molecular beam is bent by the magnet 17° into an electrostatic analyzer. In front of the analyzer there are two slits which monitor the position of the HH^+ beam. The horizontal variation of the beam position reflects the beam energy fluctuation. The entrance slits provide a correction signal derived from the difference in the slit currents which is fed back to the corona control system. This system provides the correction for large, slow (~10Hz) terminal voltage fluctuations and reduces the magnitude of these fluctuations to ~2-3 keV.

The HH^+ beam then passes through the slits into an electrostatic analyzer. The analyzer consists of two metal plates (90° of arc) with a gap separation of 4.5 mm. An equal and opposite, well regulated high voltage is applied on the inner and outer plates by the programmable Bertan power supplies. Since the electrostatic fields in the analyzer are perpendicular to the HH^+ beam

Figure 3.1 Layout of the High Resolution Laboratory, showing the KN Van de Graaff accelerator and feedback system.

High Resolution Laboratory and Control System

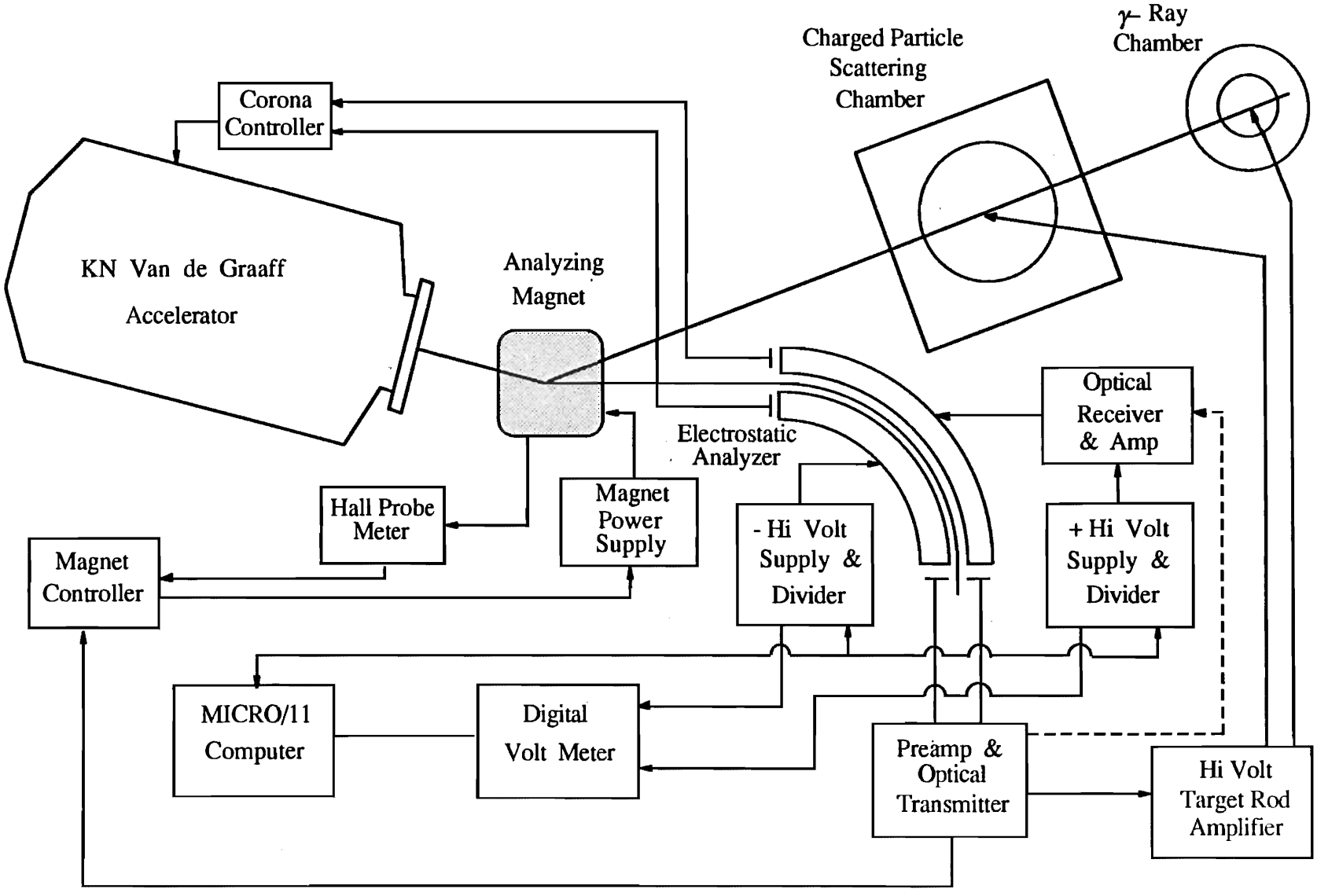

trajectory, the analyzer does not change the beam energy, and an image is formed at the exit of the analyzer where two slits are located. The HH^+ beam position fluctuation which remains after corona feed back leads to a current difference on the exit slits and provides another correction signal. The signal is appropriately amplified and applied to the outer plate of the analyzer to maintain the beam centered in the analyzer, and is also fed back to the magnet controller. The magnet controller changes the output current of the magnet power supply to correct for fluctuations up to a frequency of ~800Hz. The correction signals are also applied to the target rod which is biased to +3 kV DC, so that proton energy fluctuations on the target which have the same time dependence as the molecular beam are reduced. The analyzer geometry is such that 1 volt difference in the analyzer corresponds to a proton energy difference of 111 eV. A microprocessor (Micro PDP-11) is used as the main controller to monitor the high voltage difference on the plates. The microprocessor is linked to the VAX 11/750 so that the high voltage can be changed automatically during data acquisition. Drifts and fluctuations in the Bertan bias supplies are monitored and corrected by a high precision Fluke Digital Voltage Meter (DVM) which is controlled by the microprocessor. When the bias drifts more than 0.09V (corresponding to a proton energy drift of 10 eV), the DVM will produces an inhibit signal to turn off the data taking. The homogenizer and the microprocessor are described in detail by Warthen (1987).

B. Scattering Chamber and Detectors

A top view including detectors and collimators is shown in figure 3.2. The chamber vacuum is maintained at 10^{-6} torr by the diffusion pump, and during the experiment liquid nitrogen traps are filled. In front of the scattering chamber a series of collimators is used to reduce the beam spot size; after these collimators the proton beam spot on the target is typically 2 mm $\times$1 mm. The target rod (not shown) is in the center of the chamber and can hold up to 4 targets and a tuning ring with a 2 mm diameter hole in the center. The beam passes through the collimators and is dumped into a Faraday cup at the end of the chamber. In front of the Faraday cup there is a plate biased at -90 VDC to prevent secondary electron emission from the cup. A good tuning condition is about

Figure 3.2 Top view of the charged particle scattering chamber, beam collimators and detectors.

Charged Particle Scattering Chamber

(Top View)

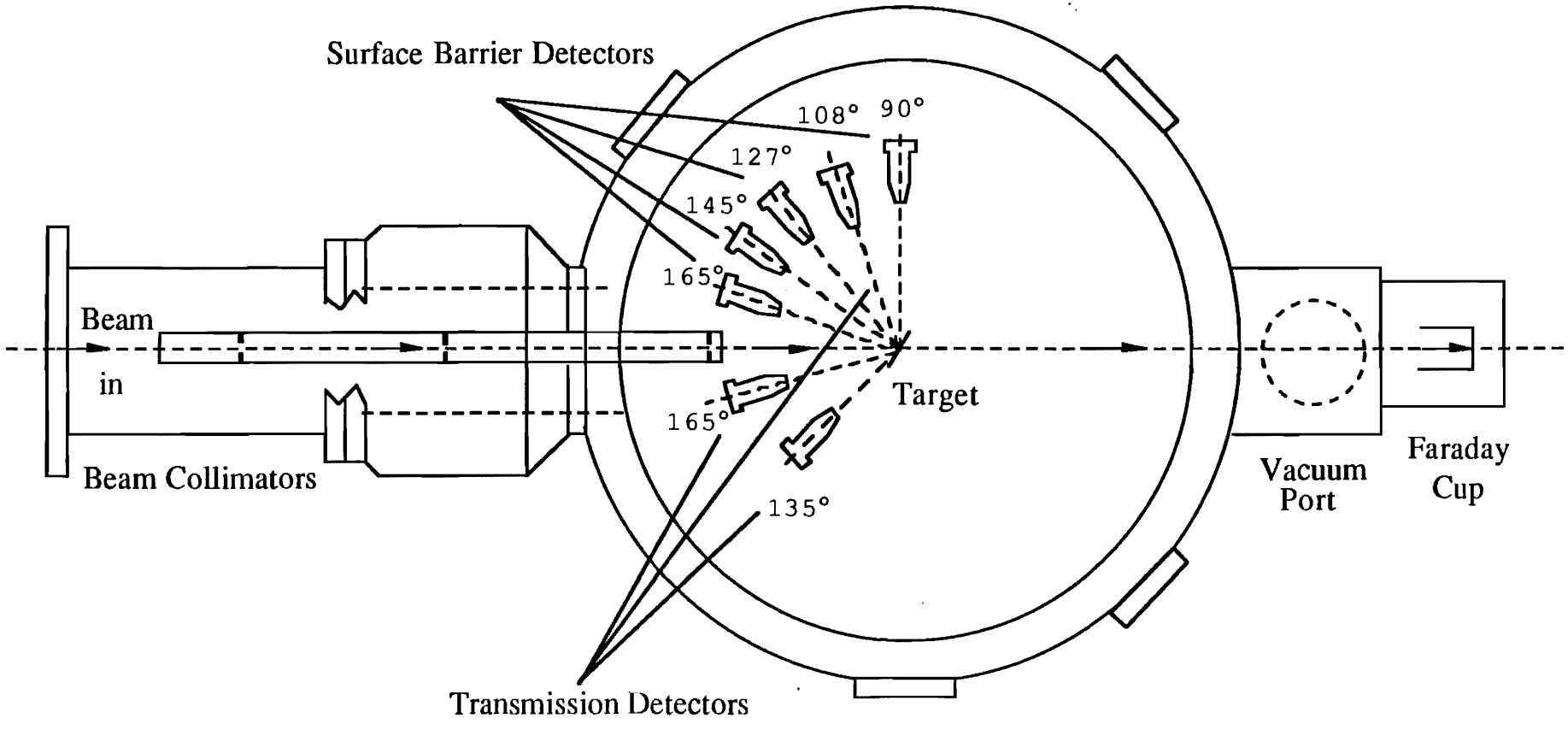

2-3 μA beam current passing through the tuning ring and less than 20 nA on the ring.

From E_p = 1.00 MeV to 3.00 MeV, five Ortec surface barrier detectors were mounted at the laboratory angles 90°, 108°, 127°, 145° and 165° relative to the beam to detect scattered protons. These detectors have active areas of 50 mm^2 and depletion depths of 100 μm or 300 μm, depending on the proton energy. The resolution of the detectors is about 15-20 keV. To measure the $^{31}P(p, \alpha_1)$ reaction, three Ortec transmission detectors (detector thickness about 50 μm) were employed at 108°, 135° and 165° (the surface detector at 108° was replaced by a transmission detector, see figure 3.2), because the α_1 particles generate the same pulse height in the surface barrier detector as protons elastically scattered from ^{16}O, which is an unavoidable contaminant. The transmission detectors cannot separate scattered protons and α_1 particles below E_p = 2.60 MeV. The solid angles for the surface barrier detectors were adjusted such that the counting rate for Rutherford scattering at each detector is about the same; this assures that the data acquisition system is not jammed by any one detector which has a high counting rate. The targets face the beam at 30°, such that the detectors can "see" an 1.2 mm diameter spot on the target. For the T = 2 resonance measurement (see Chapter IV), a NaI detector was mounted outside of the chamber at 45° to detect the γ decay of the resonance.

C. Data Acquisition System

The data acquisition system is composed of detectors, standard NIM modules and CAMAC modules, and is supported by the VAX 11/750 and a general data processing software XSYStem. Figures 3.3 and 3.4 show the block diagram of the electronics for data acquisition and CAMAC interface to the computer. Warthen (1987) made major contributions to the automation of online data analysis and beam energy control. In this dissertation the hardware (electronics, interface, etc.) and software (XSYS) will be discussed only briefly.

The charged particles or γ rays emitted from the target are detected by surface barrier detectors or NaI detectors and produce signals. The signals are amplified by Ortec Model 142A preamplifiers and sent to the main spectroscopy amplifiers (Ortec Model 572) to form well shaped

Figure 3.3 Block diagram of the data acquisition electronics.

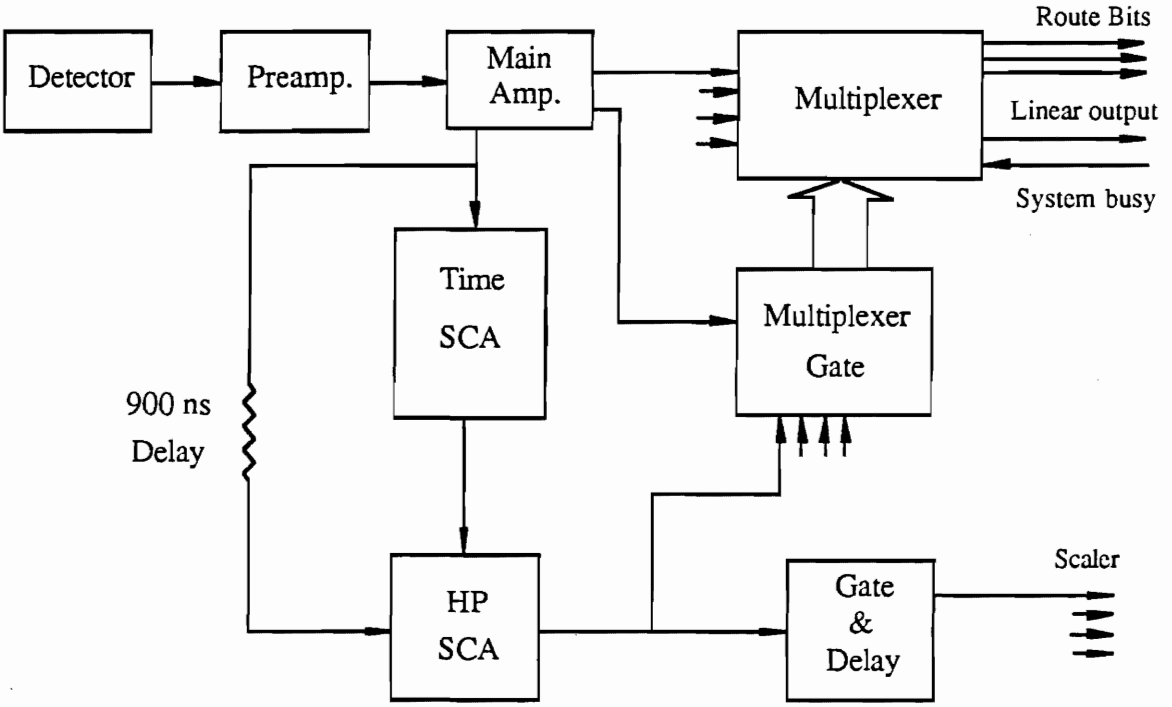
Detector
Preamp.
Main Amp.
Multiplexer
Route Bits
Linear output
System busy
Time SCA
Multiplexer Gate
900 ns Delay
HP SCA
Gate & Delay
Scaler

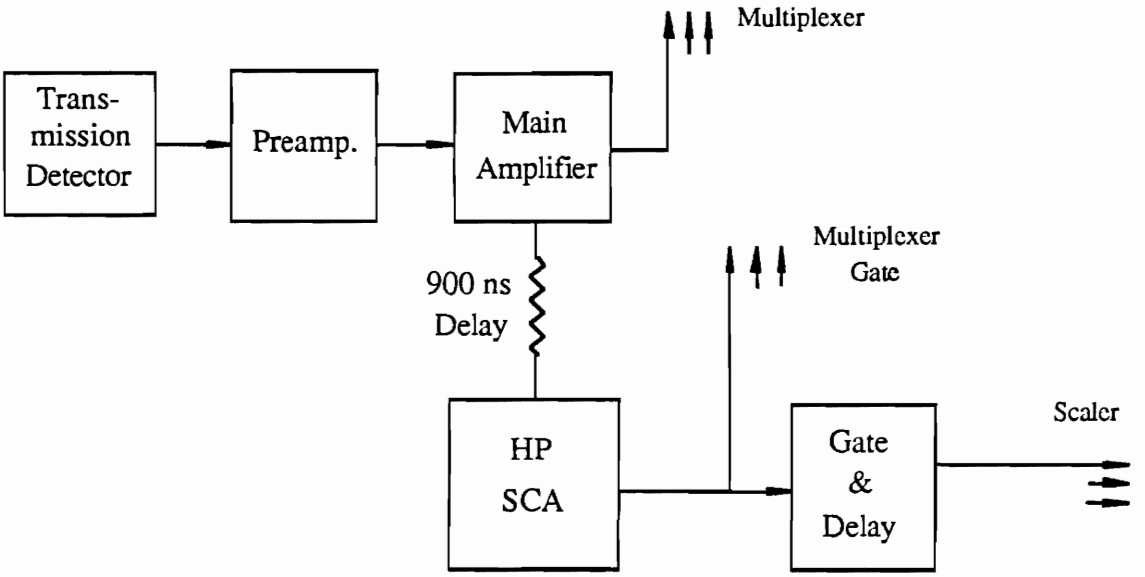
Multiplexer
Trans-mission Detector
Preamp.
Main Amplifier
Multiplexer Gate
900 ns Delay
HP SCA
Gate & Delay
Scaler

Figure 3.4 Block diagram of the data flow, CAMAC crate, computer interface and associated electronics.

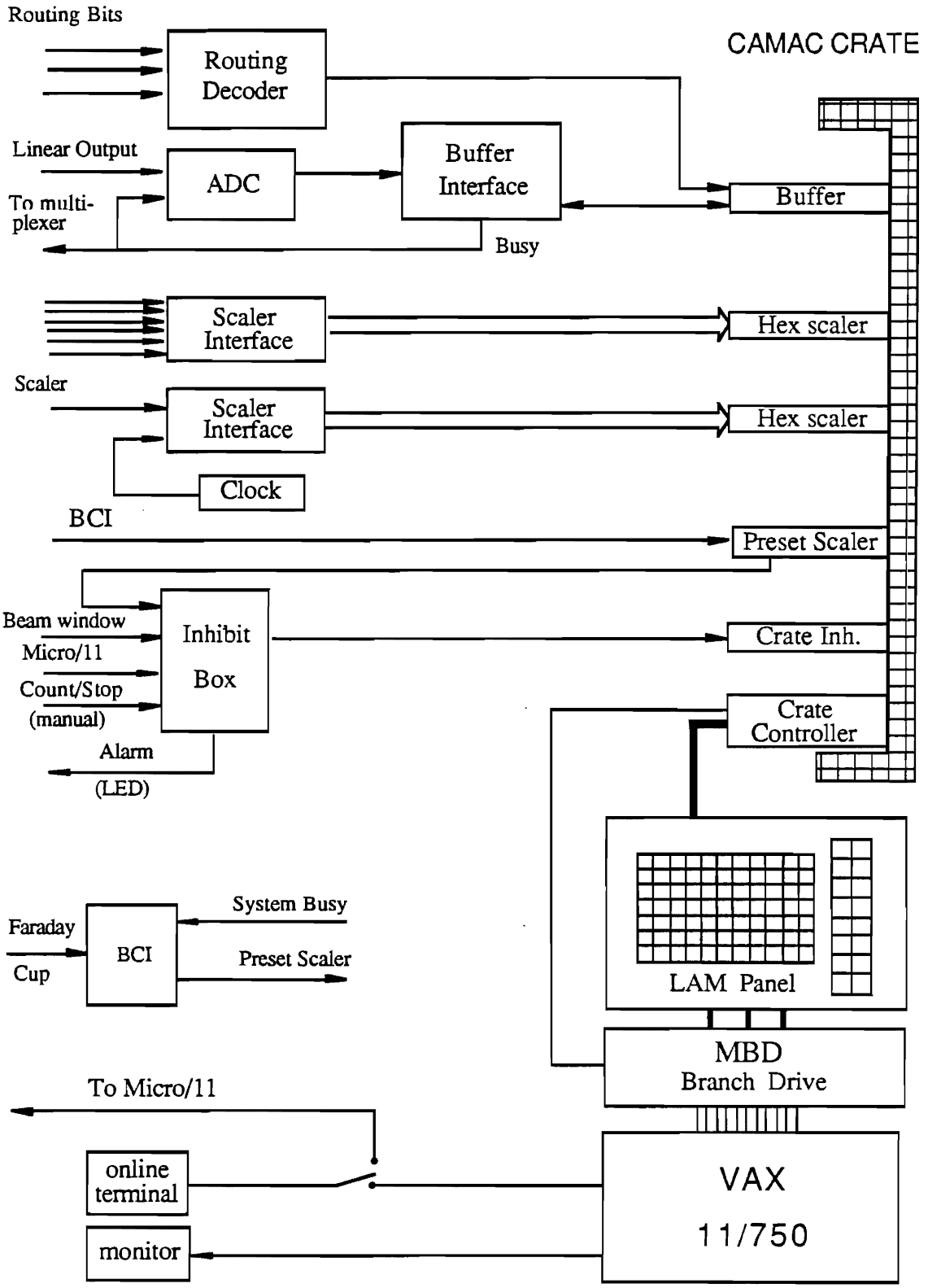
Routing Bits
Routing Decoder
CAMAC CRATE
Linear Output
ADC
Buffer Interface
To multi-plexer
Buffer
Busy
Scaler Interface
Hex scaler
Scaler
Scaler Interface
Hex scaler
Clock
BCI
Preset Scaler
Beam window
Micro/11
Count/Stop (manual)
Inhibit Box
Crate Inh.
Crate Controller
Alarm (LED)
LAM Panel
Faraday Cup
BCI
System Busy
Preset Scaler
MBD Branch Drive
To Micro/11
online terminal
monitor
VAX 11/750

signals. The amplitudes of the signals are proportional to the energies of the particles emitted or scattered from the target, and form peaks in the spectra. All the delayed unipole outputs of the amplifiers are sent into an Ortec multiplexer (Model 467-8). The output of the multiplexer is the scrambled linear signal accompanied with a 3-bit routing word that tells from which detector the signal originates. The counting rate of charged particles from each detector usually is very high due to protons elastically scattered from the carbon target backing; these carbon counts would keep the ADC "busy" and increase the dead time. In addition high counting rates produce pile-up. Therefore the carbon peak in the spectrum must be eliminated.

This is accomplished by using the carbon pulses to disable the multiplexer which sends the linear signals to the ADC. As shown in figure 3.3, the bipolar output of the spectroscopy amplifier is sent to the Timing Single Channel Analyzer (TSCA Ortec Model 551) operated in window mode and adjusted such that only carbon pulses can pass through. The bipolar output is also sent through a delay line to the input of another Single Channel Analyzer (HPSCA) operated in integral mode. The HPSCA is inhibited by the TSCA output, so that if the bipolar signal is a carbon pulse the HPSCA is inhibited and the multiplexer is not activated (disabled); if the bipolar signal is not a carbon pulse, the HPSCA will generate a short pulse. This short pulse is changed to a logic pulse by the Ortec Model 416A Gate and Delay Generator, and is sent through a scaler interface to a CAMAC scaler. The short pulse also is expanded to a wider logic pulse by a TUNL made gate generator to enable the multiplexer, and the multiplexer sends the unipolar signal to the ADC for digitizing. One can discriminate against electronic noise by adjusting the HPSCA threshold. Obviously, for each detector the number of counts in the scaler will be larger than or equal to the number of counts digitized by the ADC due to the ADC digitizing dead time. The dead time correction is performed in both online and offline data analysis.

The data processing is accomplished by CAMAC interfacing and Microprogrammed Branch Driver (MBD) and the data are stored in the computer, with the procedure supported by the XSYS software package. XSYS is a data acquisition and analysis system for VAX computers created at TUNL. Overviews of XSYS are given by Gould and Roberson (1983); the data flow and the linkage between CAMAC and computer are shown in figure 3.4.

The routing word is decoded and combined with the digitized signal from a Northern ADC (NS-612), and these numbers are encoded again by a CAMAC module Borer Buffer as a 16 bit word (bits 1-3 are detector numbers, bit 4 is for the coincident record, and bits 5-16 are the pulse height in digital numbers). The Borer Buffer has two 512-word buffers, so that when one of the buffers is full, the events will be recorded in another buffer, and at the same time the module provides a Look-At-Me (LAM) signal to the Crate Controller (CC) for data transfering. Upon being informed by the LAM, the CC will read one CNAF (Crate number, module Number, Address and Function) command from a defined channel of the MBD, execute the command, report the execution results to the MBD and read in the next CNAF. The CNAF command file is written for a specific function for the specific module. For example, the CC response to Borer Buffer LAM is to read instructions from the MBD, which tell the CC to read the Borer Buffer and to transfer the data to the MBD and then initialize the buffer. A special LAM control panel can set coincidence requirements between LAMs from different modules; in this way multi-parameter events can be hardware defined. In this experiment the LAM control panel is only set to tell the CC which channel in the MBD will perform the data transfer to the VAX 11/750 via unibus. The MBD is basically an interface between CAMAC crate Branch Highway and the Branch Highway to the VAX. There are 8 interrupts which cause the MBD to operate in one of the 8 channels. Channel 7 has the highest priority and channel 0 the lowest. Either a LAM, a coincidence LAM, or a request from the VAX can activate a channel. The MBD has read/write access to the VAX memory and can interrupt the VAX CPU.

A General Data Acquisition Program (GDAP) is down loaded to the MBD before the start of each experiment. This program contains all the instructions for the data transfer accompanied with the CNAF commands for the CAMAC modules. There are two big data buffers in the VAX 11/750. When the buffer is full, the subprocess XSORT6 which is hibernated in the computer will be activated and the data sorted according to the different data areas allocated by the experimenter. The CAMAC crate can also be inhibited by an "or" box. Any logical request on the box will also turn off data taking, and an LED signal will be sent to inform the experimenter. The preset scaler can be pre-written in a digital number, and will count down as the Beam Current Integration (BCI)

increases. When the preset scaler reaches zero, it will issue an inhibit signal and LAM signal. The MBD will read the Borer buffer and the scalers via the CC and transfer the contents to the VAX, where the data will be sorted and dumped onto magnetic tape. During the experiment the scalers are read by computer every 3 seconds, so one can conveniently monitor whether the data acquisition system is working properly.

D. Targets

One of the advantages of this experiment is that the natural abundance of ^{31}P is 100% and there is no isotopic contamination problem. The usual phosphorus target for nuclear experiments is prepared from red phosphorus with the method described by Hooton (1967). In the present experiment an alternate method for preparation of a thin phosphorus target was successfully employed. The compound Zn_3P_2 was chosen as the target material (melting point > 470 °C). Commercially obtainable (4-5 $\mu g/cm^2$) carbon foils were floated on the target ring as the target support. In the initial preparation of targets it was found that the Zn_3P_2 did not adhere well to the carbon foil. Therefore before evaporating Zn_3P_2 a thin layer (~0.5 $\mu g/cm^2$) of ultra-pure Ni was evaporated onto the carbon foil. Ni was chosen because it provides both good target stability and uniformity, and the Ni and Zn peaks in the spectra also provide normalization factors at low beam energies. Below 2 MeV, the two peaks cannot be distinguished from each other in the spectra, and it was assumed that there are no proton resonances for Ni and Zn below 2 MeV. A layer of 1-3 $\mu g/cm^2$ Zn_3P_2 was evaporated onto the foil, depending on the energy range of the experiment. The thickness of the target was measured by a vacuum deposition thickness monitor and later tested with a low energy proton beam. The evaporation was performed with high current evaporation from a W open boat for Ni, and a thin Ta open boat for Zn_3P_2. Before the evaporation, the Ni and Zn_3P_2 were baked for 20-30 minutes to reduce the moisture content. For Ni evaporation the temperature was adjusted just above the melting point; one can barely see the Ni on the target. One cannot actually see Zn_3P_2 powder melt before it evaporates, and the powder has a tendency to jump out of the boat when the boat temperature is high. Therefore the temperature

was very carefully controlled. Targets made in this way proved to be stable after 2-3μA beam conditioning for about 40 minutes and to have good uniformity. A typical spectrum is shown in figure 3.5.

E. Procedure

Before each experimental run, the accelerator was calibrated with secondary energy standards. The first step in the calibration procedure is to correct for the +3 kV DV target rod bias and the energy offset in the data at the lower energy calibration. Relativistic effects also must be considered. As the energy of the HH^+ ion increases from 1.00 to 4.00 MeV, the relativistic mass of HH^+ increases, which results in a non-linear relationship between the analyzer beam energy and the analyzer plate voltage required to bend the beam through the analyzer. Thus an increased electric field is needed to deflect the HH^+ ions due to the mass increase. Calculations (Adams 1983) indicate that up to 3 keV correction is needed for the beam energy range 1.00 to 4.00 MeV if the relativistic effect is set to zero at the calibration point.

The energy calibration is performed by locating a secondary standard, an *s*-wave resonance at 1.844 MeV in $^{44}Ca(p, p)$ (Wimpey 1974). This secondary standard was calibrated with a primary neutron threshold standard $^{7}Li(p, n)$ at $E_p = 1.8806$ MeV (Marion 1966). The calibration was performed by adjusting the potentiometers for the inner and outer analyzer plates (an equal amount) so that the Fluke DVM reads the correct energy at the ^{44}Ca calibration point. For higher energies, another calibration point was chosen with a second standard $^{56}Fe(p, p)$ at $E_p = 3.2387$ MeV; again this standard was calibrated with the primary standard $^{13}C(p, n)$ at $E_p = 3.3257$ MeV.

Most of the data in this experiment were measured twice. This ensured reproducibility and improved the data quality for the sections where accelerator tuning conditions changed in the previous run.

Before the data taking, all the electronics, Fluke DVM and the homogenizer and analyzer system were turned on for several hours to "warm up" the system. By employing XSYS programs, the data areas were allocated in the VAX 11/750 for the spectra and the yield curves,

Figure 3.5 Typical spectrum for proton-induced reactions on ^{31}P measured with a surface barrier detector at 165°. Sample yield curves for four reaction channels are shown.

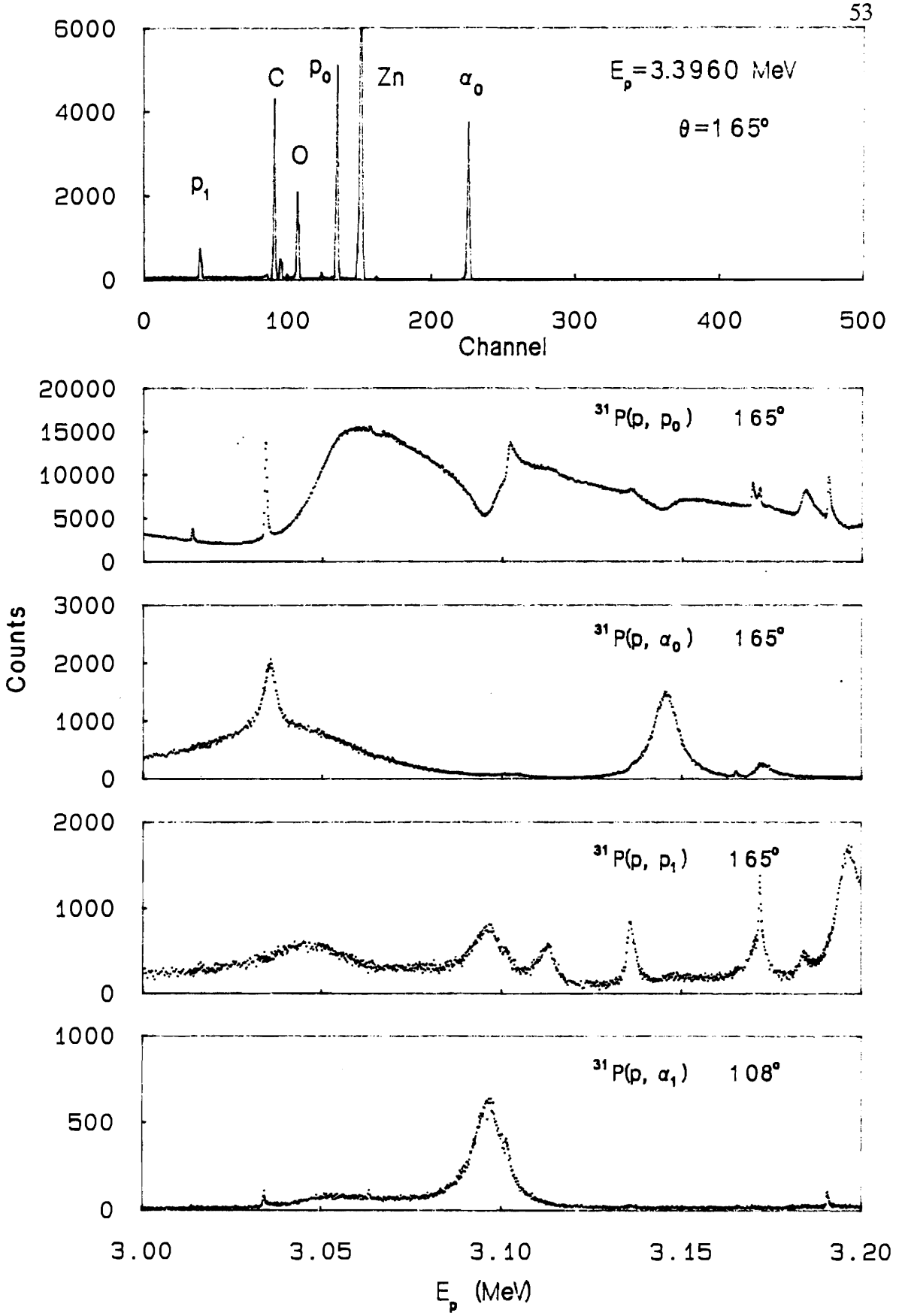
6000
4000
2000
0
C
p_0
Zn
α_0
O
p_1
E_p=3.3960 MeV
θ=165°
0
100
200
300
400
500
Channel
20000
15000
10000
5000
0
^{31}P(p, p_0) 165°
3000
2000
1000
0
^{31}P(p, α_0) 165°
2000
1000
0
^{31}P(p, p_1) 165°
1000
500
0
^{31}P(p, α_1) 108°
Counts
3.00
3.05
3.10
3.15
3.20
E_p (MeV)

and all the kinematic information and the detector arrangement were entered into the computer. The XSYS data acquisition software allows online monitoring of the spectra and the yield curves of the peaks in the spectrum for each angle. The spectrum lengths are 512 channels. Each spectrum can be energy calibrated so that the windows of interest, in which peaks will be summed for the yield curves, can be shifted automatically as the proton energy changes. The spectroscopy amplifier and HPSCA were adjusted so that the p_1 and α_1 pulses are properly digitized (by the ADC) and appear in the spectra. At lower energies, for 90° and 108° the ^{31}P and Zn peaks are close together. Since the inelastic p_1 group is not important below $E_p = 2.00$ MeV, a biased amplifier was added between the spectroscopy amplifier and the multiplexer for these angles to magnify the interesting section of the spectrum. Data were taken in energy steps of 400 eV or 100 eV, depending on the sharpness of the resonances in the yield curves. The BCI preset was set to 100 μC or 250 μC, depending on the thickness of the target, to achieve < 2% counting statistics. After the integrated beam current was accumulated for each data point, the energy, run number (which increments after each data point), spectra, and the number of counts in the scalers were stored on magnetic tape for detailed offline analysis.

A target usually lasted 24 hours before breaking. New targets were conditioned at a fixed energy for 30-40 minutes. Normally a small energy region was repeated to limit the ambiguities in the yield curve caused by the change of target. The accelerator operating parameters must be changed (tuned) for different energy ranges. Again, some data were repeated after each tuning.

Chapter IV

Data Reduction and Resonance Analysis

A. General

Yield curves for the four open channels were obtained from the corresponding peaks in the spectra stored on magnetic tape. The "stripping" program XSTRIP was written by Warthen (1987), and basically is a revised version of the XMASTER program which was utilized during data acquisition. Before executing XSTRIP all the kinematic information is entered, including detector angles, mass numbers and nuclear reaction Q-values (program XANGL, XCALIB, XMQ). A typical spectrum was read in by XREAD to calibrate the spectrum (XCALIB) and to set the windows (XWINDOW) in which the peaks will be summed by XSTRIP. The program XSTRIP reads in spectra and other information, sums the peaks of interest with a linear background subtraction, performs dead time correction, and tabulates the numbers for the yield curves at the experimental energies. The windows in the spectra are shifted automatically as the energy changes. A modification was made to XSTRIP to improve window shifting. In practice, after approximately 50 points the windows are checked to verify that the shifts are correct. The backgrounds were calculated by linear least square fitting points on each side of the peak. Finally, the yield curves were listed in a file which is suitable for the R-matrix program MULTI6.

Experimental excitation functions obtained from the previous data processing step are fit with the multi-level, multi-channel R-matrix program MULTI6. This program was originally written by Sellin (1968) and is based on the differential cross section expressions of R-matrix theory given by Lane and Thomas (1958).

The program has been updated as the studies were extended and the computer technology improved. Nelson (1983) expanded the program to be suitable for non-zero-spin targets and for up to 300 levels, 12 J^{π} values, 5 decay pairs, 10 channels for each J^{π}, 70 total channels for all the J^{π}, 1000 data points and 1000 fit points. Vanhoy (1985) fully documented the most recent version of

the program.

The code MULTI6 reads in all the parameters which are necessary for computation of the theoretical cross section, and for controlling the computation: particle masses and charges, reaction Q values, resonance energies, J^{π} values and allowed channel spin and orbital angular momenta for the J^{π} value, decay channels and laboratory partial widths. The theoretical calculations are compared with the experimental data. The fitting is performed by trial and error, with resonance energies and all parameters associated with the resonances adjusted to achieve the best visual fit. Each trial typically takes 2 to 15 minutes on the VAX 11/750 depending on the number of calculated points and the complexity of the region being fitted. In the fitting procedure the channel spin representation (LS coupling) was chosen for angular momentum coupling, mainly because the resonance shapes in the elastic channel are closely related to the l value, due to Coulomb and resonance/reaction interference effects. To perform the theoretical calculation, the value of the boundary conditions must be fixed. As discussed in chapter II, B_c is a real, arbitrary, energy independent boundary condition. In the calculation for each resonance B_c was chosen equal to the shift function S_c^{λ} at the resonance energy. This choice of boundary condition places the apparent resonance energy exactly at the R-matrix energy eigenvalue position. For a single isolated resonance at energy $E = E_{\lambda}$, the collision matrix is given by (2.28)

$$U_{cc'} = \exp[i\,(\omega_c+\omega_{c'}-\phi_c-\phi_{c'})][\,\delta_{cc'} + \frac{i\Gamma_c^{1/2}\Gamma_{c'}^{1/2}}{(E_{\lambda}-\Delta_{\lambda}(E)-E)-\frac{i}{2}\Gamma_{\lambda}}\,], \qquad (4.1)$$

where

$$\Delta_{\lambda}(E) = -\sum_{c'} (S_{c'}^{\lambda}-B_{c'})\,\gamma_{\lambda c'}^{2} \quad .$$

It is usually a good approximation to treat $\Delta_{\lambda}(E)$ as a linear function of E over a fairly wide range of energies. Thus it is convenient to write $\Delta_{\lambda}(E)$ as

$$\Delta_{\lambda}(E) = \Delta_{\lambda}(E_{\lambda}) + (E-E_{\lambda})\left(\frac{d\Delta_{\lambda}}{dE}\right)_{E=E_{\lambda}} + \ldots$$

B_c was chosen such that $\Delta_{\lambda}(E_{\lambda}) = 0$ for each resonance. Once B_c is fixed, one has

$$\left(\frac{d\Delta_{\lambda c}}{dE}\right) = -\gamma_{\lambda c}^2 \left(\frac{dS_c^{\lambda}}{dE}\right). \qquad (4.2)$$

Except for *s*-wave neutrons, the magnitude of dS_c^{λ}/dE is usually $\leq Ma^2/\hbar^2$ (Thomas, 1958), where M is the mass of the compound nucleus and a is the channel radius. For nuclei in the *s-d* shell, Ma^2/h^2 is on the order of 10^{-3}/keV to 10^{-2}/keV. In practice, B_c is always set equal to S_c^{λ} at each resonance for each channel, and $\Delta_{\lambda}(E)$ is assumed to be zero in the whole resonance region. From the equation (4.2) one can see that the error in this assumption is related to the slope of the shift function. Calculations (figure 4.1) indicate that the slopes are fairly small; for proton elastic and inelastic channels the value is about $0.2\text{-}0.4\times10^{-3}$/keV, and for the (p, α_0) channel the value is about $0.6\text{-}0.9\times10^{-3}$/keV. For an isolated resonance with γ_{λ}^2 not very large, this method of choosing boundary conditions will introduce the least error in extracting the physical information. Nelson (1983) tested different choices and reached essentially the same conclusion. However, for overlapping resonances, the non-zero value of $\Delta_{\lambda}(E)$ in the resonance energy range might affect the values of the widths and the energy positions which are obtained from the fitting. In the fitting procedure, another parameter that must be assumed is the nuclear radius. This is conventionally taken to be $a_c = r_0(m_3^{1/3} + m_4^{1/3})$, where m_3 and m_4 are the masses of the reaction products (m_1 and m_2 for entrance channel). The radius r_0 was chosen to be 1.25 fm for consistency with previous analyses performed in this laboratory. Given a set of resonance parameters, the code MULTI6 generates the theoretical differential cross section at the angles at which the experiment was performed, and the cross sections are convoluted with a Gaussian resolution function with a low energy Lorentzian tail to simulate beam straggling effects. The width of the Gaussian function was chosen to be 350 eV, which was determined by fitting narrow f-wave resonances in the elastic or α_0 channel. Experimental data points are normalized to the theoretical calculation by comparing the areas under the theoretical cross section curves and experimental yield curves in the same energy region.

Figure 4.1 The shift function for the $^{31}P(p, p)$ and (p, α_0) reactions. The slopes of the shift functions are small.

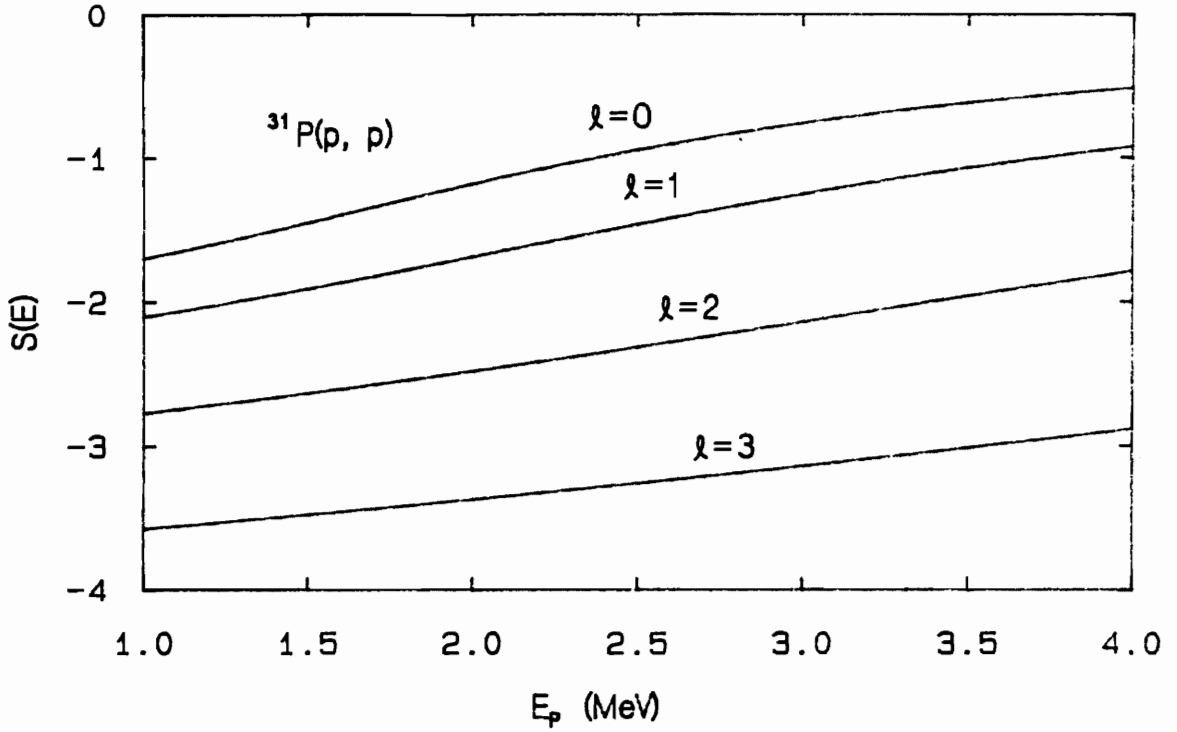
0
−1
−2
−3
−4
S(E)
^{31}P(p, p)
ℓ=0
ℓ=1
ℓ=2
ℓ=3
1.0
1.5
2.0
2.5
3.0
3.5
4.0
E_p (MeV)

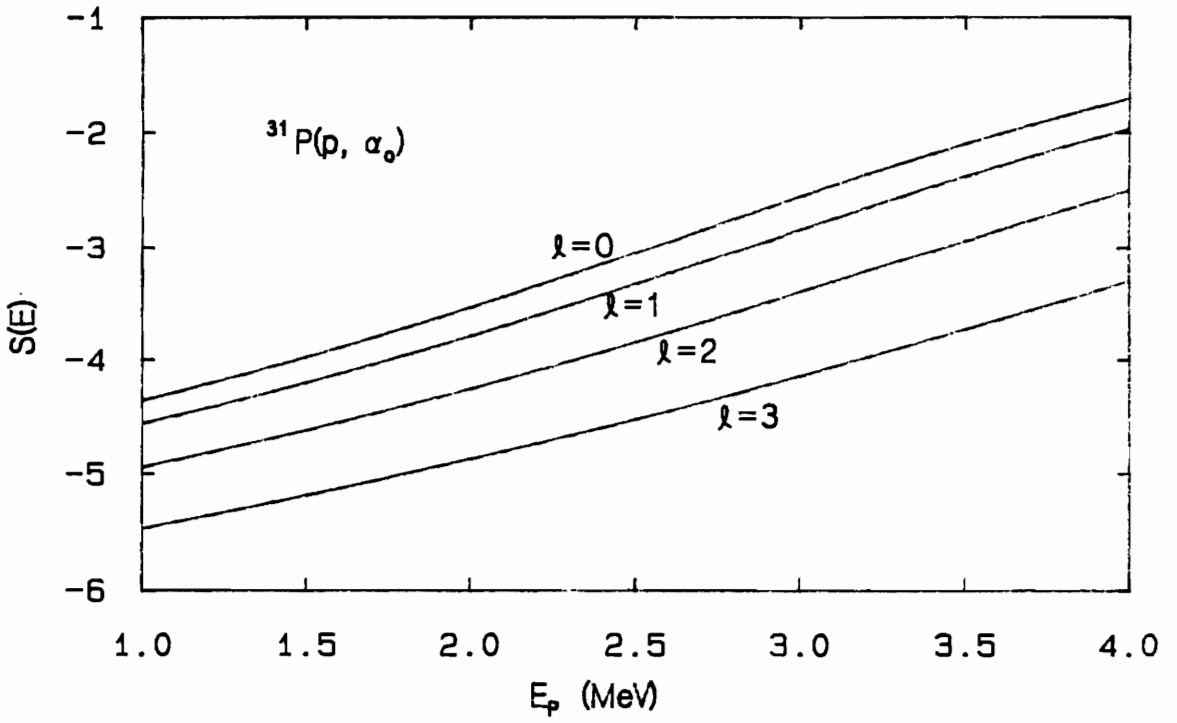
−1
−2
−3
−4
−5
−6
S(E)
^{31}P(p, α_o)
ℓ=0
ℓ=1
ℓ=2
ℓ=3
1.0
1.5
2.0
2.5
3.0
3.5
4.0
E_p (MeV)

B. Elastic Scattering

As was shown in figure 2.1, in the channel spin representation $J = S + L$. For a target of spin s_t and a projectile of spin s_p, the two spins are coupled to form a channel spin s; the channel spin is then combined with the relative orbital angular momentum l to form the spin J of the compound nuclear state. The channel parity is $(-1)^l \pi_t \pi_p$, where π_t and π_p are the parities of the target and the projectile, respectively. Obviously, the simplest case is when the target spin s_t equals zero. For a given J^π value there is only one choice of L (l) and S (s_p) coupling in the elastic entrance channel due to the conservation of parity and total angular momentum in the process. However, for targets with spin the coupling scheme will be complicated by the possibility that a resonance can be formed from various l, s combinations, and that the excited states may have several decay channels. The angular distributions will be determined by the relative strength of these channels. The combination of the spin 1/2 proton with the target ^{31}P (with ground state spin 1/2) gives channel spin values of 0 and 1. Figure 4.2 shows allowed entrance and exit channel l, s values for target spin equal to 0 and 1/2. For example, a 0^+ state can be formed and can decay only via $l = 0$, $s = 0$, but a 1^- state may decay by emitting an $l = 1$, $s = 0$ and/or $l = 1$, $s = 1$ particle pair. The combination of channels with the same l-value and different s is referred to as channel spin mixing. A 2^- state can be formed by combining $s = 1$ with $l = 1$ and/or $s = 1$ with $l = 3$. The combination of channels with the same s and different l-value is called angular momentum mixing or in short, l-mixing.

The channel spin mixing ratio for the elastic channel is defined as

$$\xi = \sum_l \Gamma_{p,s=1,l} / [\Gamma_{p,s=1,l} + \Gamma_{p,s=0,l}] \ , \qquad (4.3)$$

where $\Gamma_{p,s,l}$ is the laboratory width of the l^{th} partial wave of elastic scattering with channel spin s. The l-mixing ratio is defined as

$$\varepsilon = \pm [\Gamma_{p,s,l+2} / \Gamma_{p,s,l}]^{1/2}. \qquad (4.4)$$

For convenience, a mixing angle is also defined:

$$\psi = \text{arctg}(\varepsilon) .$$

Figure 4.2 Comparison of allowed channels for proton elastic scattering from $s_t = 0$ and $s_t = 1/2$ targets.

Elastic Scattering

(LS coupling)

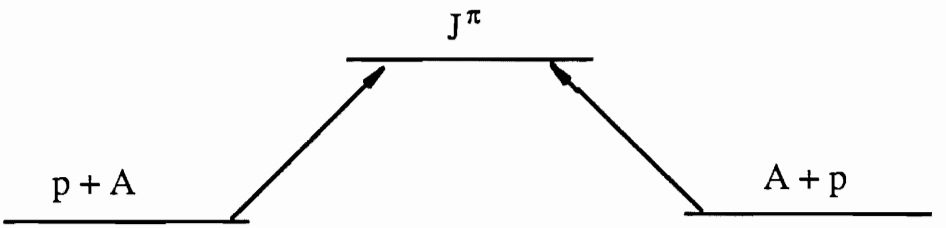

$^{31}P(p, p_0)$ $s_t = 1/2$

J^π	allowed channels	
0^-	s = 0	l = 1
0^+	s = 0	l = 0
1^-	s = 0	l = 1
	s = 1	l = 1
1^+	s = 1	l = 0
	s = 1	l = 2
2^-	s = 1	l = 1
	s = 1	l = 3
2^+	s = 0	l = 2
	s = 1	l = 2
3^-	s = 0	l = 3
	s = 1	l = 3

$^{32}S(p, p_0)$ $s_t = 0$

J^π	allowed channels	
$1/2^-$	s = 1/2	l = 1
$1/2^+$	s = 1/2	l = 0
$3/2^-$	s = 1/2	l = 1
$3/2^+$	s = 1/2	l = 2
$5/2^-$	s = 1/2	l = 3

Thus, ξ varies between zero for pure $s = 0$ and unity for pure $s = 1$, while ψ varies from –90° to 90°. For scattering of an unpolarized proton beam from an unpolarized target, channel spin mixing is incoherent while l -mixing is coherent. In the case of an $s_t = 1/2$ target with positive parity, in the elastic channel s-mixing is allowed only for resonances with natural parity ($\pi = (-1)^J$) and l-mixing can occur only for unnatural parity ($\pi = (-1)^{J+1}$) resonances. For proton inelastic exit channels both channel spin and l-mixing are allowed. This is also true for elastic scattering from nuclei with $s_t \geq 1$. The α_0 and α_1 exit channels will be discussed later.

There are two types of scattering amplitudes for the elastic channel in the R-matrix cross section formula (2.33): the Coulomb and the resonance/reaction amplitudes. The cross section is the square of the sum of the amplitudes, which gives three terms: Coulomb, resonance and interference. The interference term causes different shapes for different l-values. These general resonance shapes for elastic scattering from ^{31}P are shown in figure 4.3.

The main task of the fitting procedure is the determination of resonance J^π values. The parity is the easiest to determine, since as shown in figure 4.3 positive parity resonances have a dip in the 90^0 elastic excitation function while negative parity resonances either have a bump or are flat. Thus, simply by inspecting the 90° elastic yield curve, one can almost always determine the parity of a resonance. For positive parity, the l-value can only be $l = 0, 2,...$ (s-, d-,... wave), while for negative parity the l-value can only be $l = 1, 3,...$ (p-, f-,... wave). Since $\Gamma_l = 2P_l \gamma^2$, and the penetrabilities P_l decrease rapidly with l (as shown in figure 4.4), the laboratory widths Γ_l with high l-value will be much smaller for the same reduced width γ^2, especially at the lower energies. Further, the sum of reduced widths for a partial wave is limited to the single particle width (see chapter V). Therefore l-mixing usually will be small unless the compound nucleus has a configuration which strongly prefers l +2 partial waves. In practice, only l <4 waves need to be considered. From the shapes at back angles (165°) and at other angles, one can determine the l-value of a resonance with little ambiguity. The differences in shapes for the two channel spins are noticeable for p-wave and f-wave resonances. A p-wave with channel spin 1 gives a bump at 90° and a spike at 165°, while channel spin zero has a rather flat pattern at 90° and 165°. The lower energy side of an $s = 0$, $l = 1$ resonance has a deeper dip. The difference for d-wave resonances

Figure 4.3 Calculated excitation functions for $^{31}P(p, p_0)$ at four angles. Shapes for ℓ = 0, 1, 2, and 3 resonances are shown for each channel spin with the resonance strength $(2J+1)\Gamma_p$ = 1.0 keV.

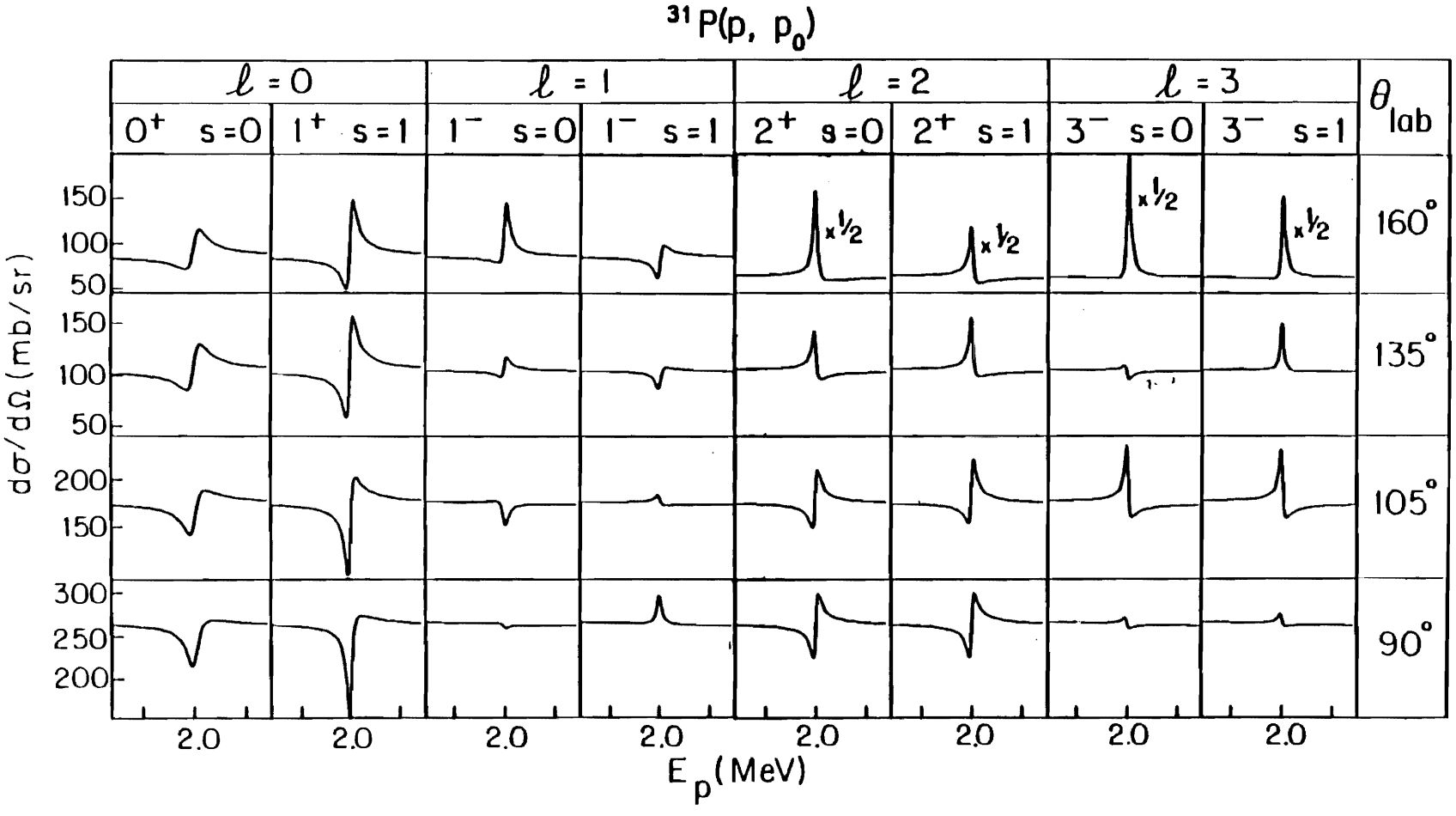
$^{31}P(p, p_0)$
$\ell = 0$
$\ell = 1$
$\ell = 2$
$\ell = 3$
θ_{lab}
0^+ s=0
1^+ s=1
1^- s=0
1^- s=1
2^+ s=0
2^+ s=1
3^- s=0
3^- s=1
160°
135°
105°
90°
×½
$d\sigma/d\Omega$ (mb/sr)
150
100
50
200
150
300
250
200
2.0
E_p (MeV)

Figure 4.4 Coulomb penetrabilities for the $^{31}P(p, p_0)$ and (p, α_0) reactions as a function of incident proton laboratory energy and ℓ value.

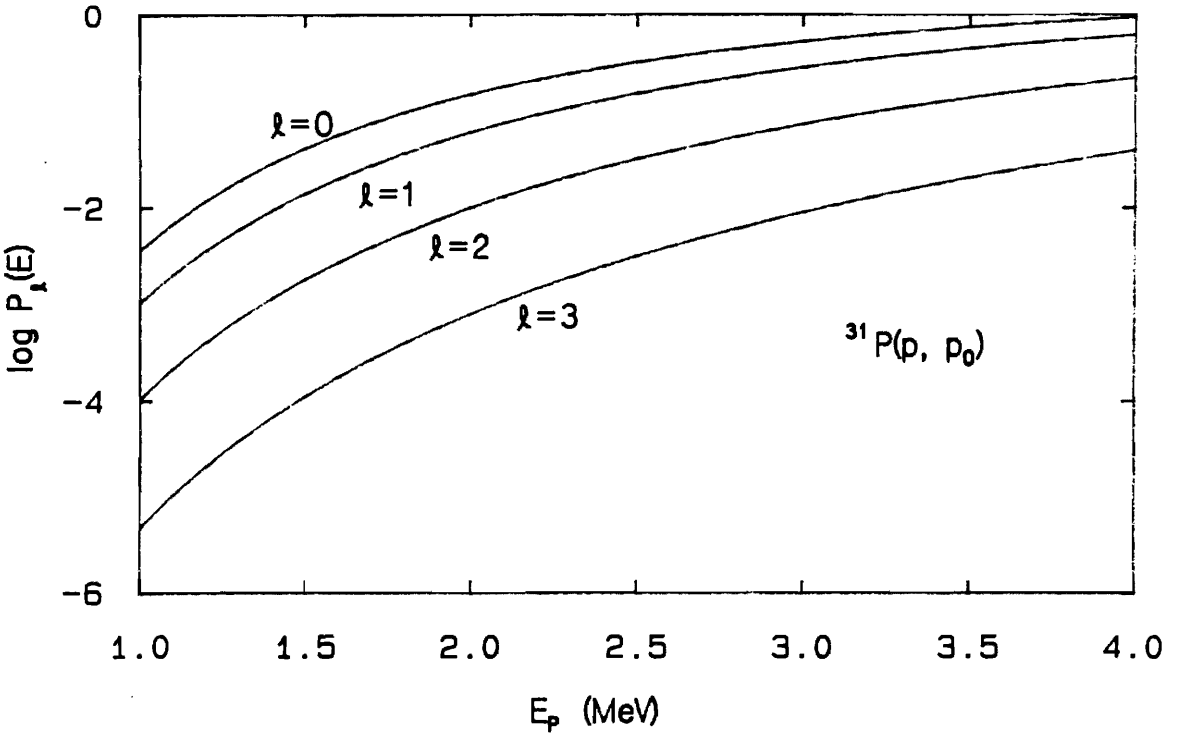
0
−2
−4
−6
log $P_\ell(E)$
ℓ=0
ℓ=1
ℓ=2
ℓ=3
$^{31}P(p, p_0)$
1.0
1.5
2.0
2.5
3.0
3.5
4.0
E_p (MeV)

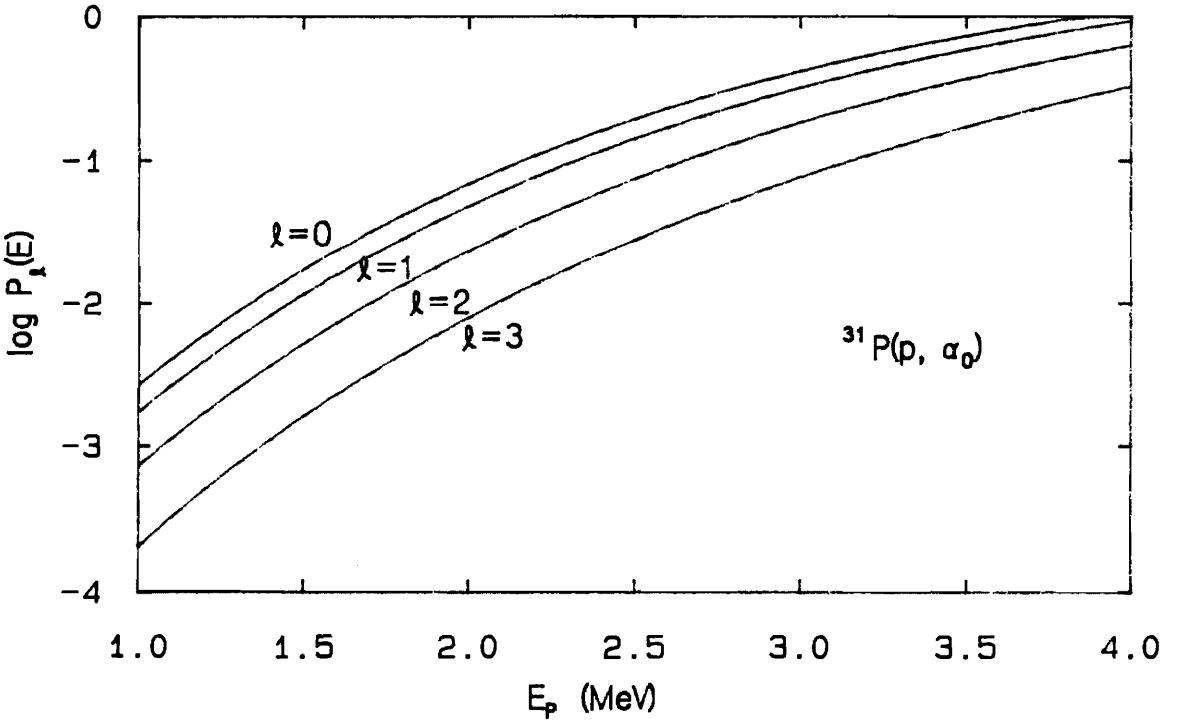
0
−1
−2
−3
−4
log $P_\ell(E)$
ℓ=0
ℓ=1
ℓ=2
ℓ=3
$^{31}P(p, \alpha_0)$
1.0
1.5
2.0
2.5
3.0
3.5
4.0
E_p (MeV)

with different channel spins is not as striking as for p-wave and f-wave resonances. This leads to more ambiguities in the determination of the J-value and the strength functions for different channel spins.

The J-value determination is more difficult. For fixed s- and l-values, higher J-values affect the excursion of the general shape because the resonance terms in the elastic cross section expression (2.33) have a (2J+1) dependence. Examples are given in figure 4.5 and figure 4.6 for $s = 1$, p-wave and $s = 1$, d-wave resonances. The $J = 0$, s-wave resonances are usually easy to identify, but for higher J the channel spin mixing and l-mixing add more uncertainty to the J-value assignment. Figure 4.7 shows the variation of the shapes of 1^- p-wave resonances as the mixing ratio ξ varies from 0 to 1. The change of the shape with l-mixing is striking because the partial wave amplitude is coherently added in the cross section. Figure 4.8 shows 1^+ s- and d-wave mixing for 1^+ resonance shapes and figure 4.9 shows 2^- p- and f-wave mixing. At higher energies where the penetrabilities are larger for l +2 partial waves, the l-mixing is larger. It should be noted that for isolated resonances, the relative sign of the partial width amplitude has only slight effects which are usually very difficult to distinguish. However, the sign is very important for overlapping resonances or level-level interference (see section 4.2).

Figure 4.10 shows the variation in shape for 2^+ d-wave resonances, which are relatively insensitive to the change of the spin mixing ratio ξ. The shape of a 3^+ d-wave resonance is similar to that of a 2^+ d-wave resonance (figure 4.6). Without other decay channels such as the α_0 channel, and with no interference with neighboring resonances, the J-value assignment may be indefinite. Even if the J-value is fixed, for example $J = 2$, it is difficult to determine the channel spin mixing ratio without ambiguity.

It should be pointed out that all the discussion above assumes that resonance widths are larger than the energy resolution Δ of the system. For a resonance width Γ less than Δ, both J and the mixing ratio usually cannot be uniquely determined. This also happens for higher J-value resonances at lower energies with small laboratory width. Thus good experimental resolution is very important not only for separation of overlapping resonances, but also for determination of the resonance parameters.

Figure 4.5 Calculated excitation functions for $l = 1$, $s = 1$ resonances at 165° and 90°. The 0^-, 1^-, and 2^- resonances are shown for a fixed laboratory width $\Gamma_p = 1.5$ keV.

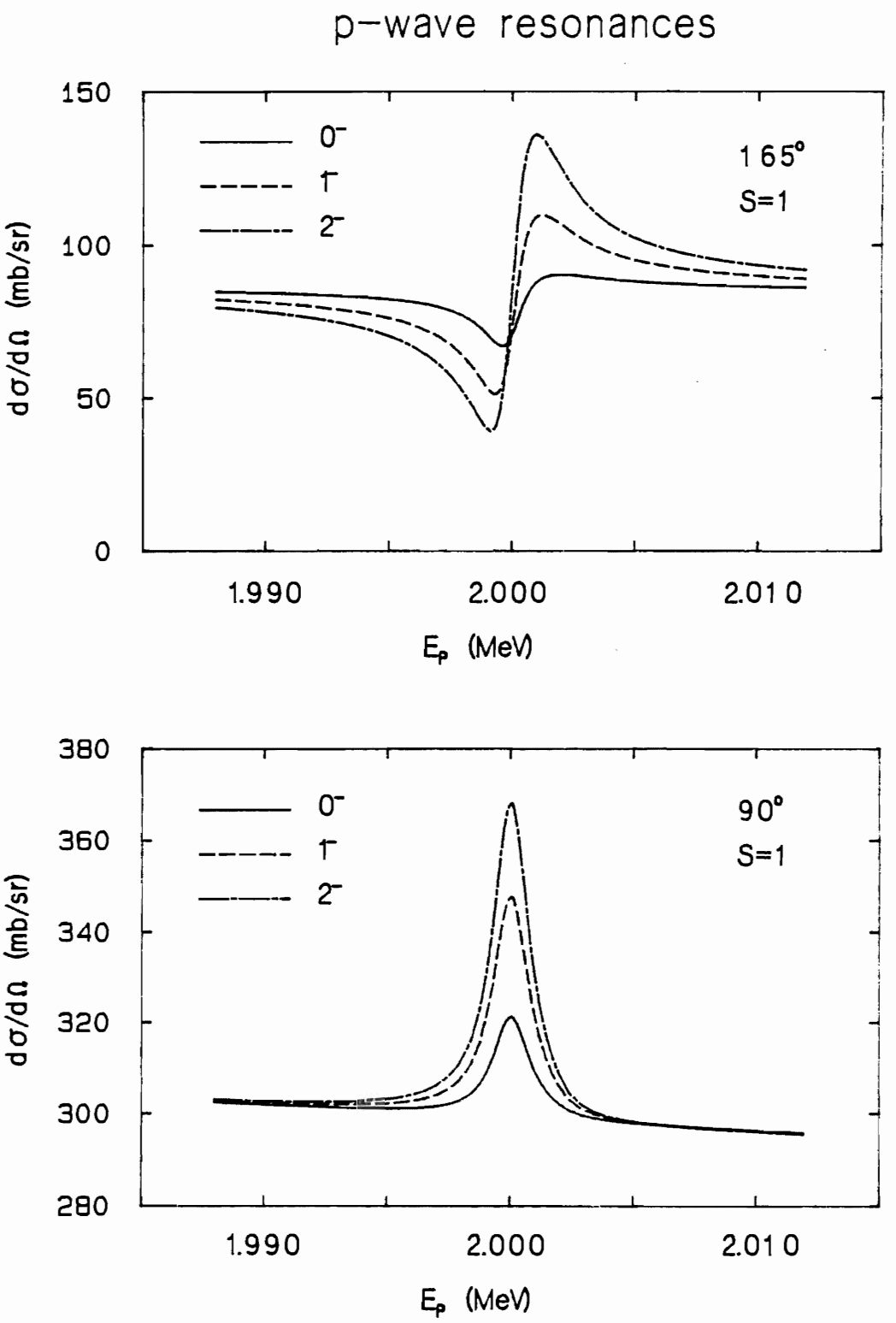
p–wave resonances
150
100
50
0
dσ/dΩ (mb/sr)
0⁻
1⁻
2⁻
165°
S=1
1.990
2.000
2.010
Ep (MeV)
380
360
340
320
300
280
dσ/dΩ (mb/sr)
0⁻
1⁻
2⁻
90°
S=1
1.990
2.000
2.010
Ep (MeV)

Figure 4.6 Calculated excitation functions for $l = 2$, $s = 1$ resonances at 165° and 90°. The 1^+, 2^+, and 3^+ resonances are shown for a fixed laboratory width $\Gamma_p = 1.50$ keV.

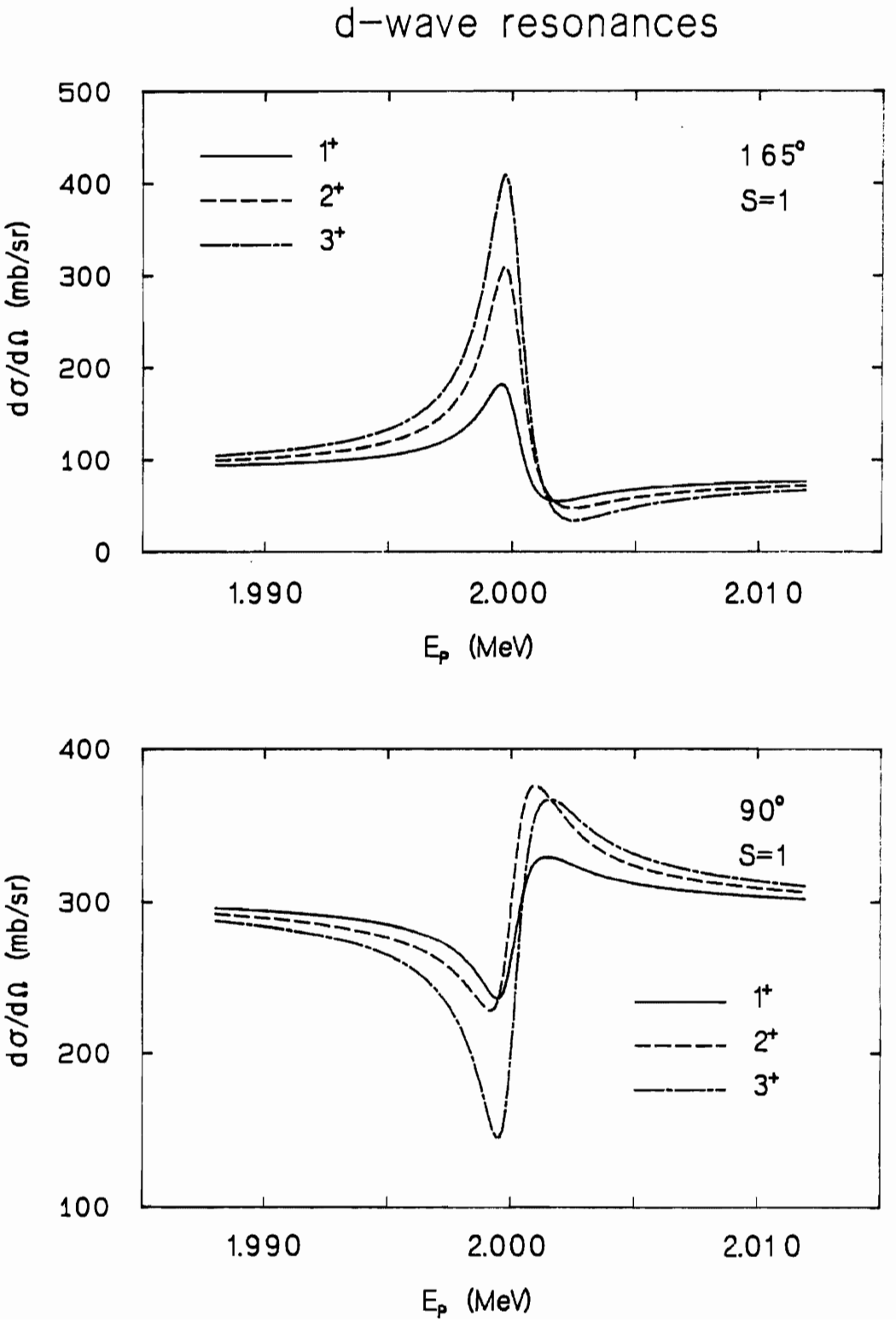
d–wave resonances
500
400
300
200
100
0
dσ/dΩ (mb/sr)
1+
2+
3+
165°
S=1
1.990
2.000
2.010
Ep (MeV)
400
300
200
100
dσ/dΩ (mb/sr)
90°
S=1
1+
2+
3+
1.990
2.000
2.010
Ep (MeV)

Figure 4.7 Variation in shape for 1^- ($l = 1$) resonances with channel spin mixing. Note there is a large change in shape from $\xi = 0$ (all $s = 0$) to $\xi = 1$ (all $s = 1$).

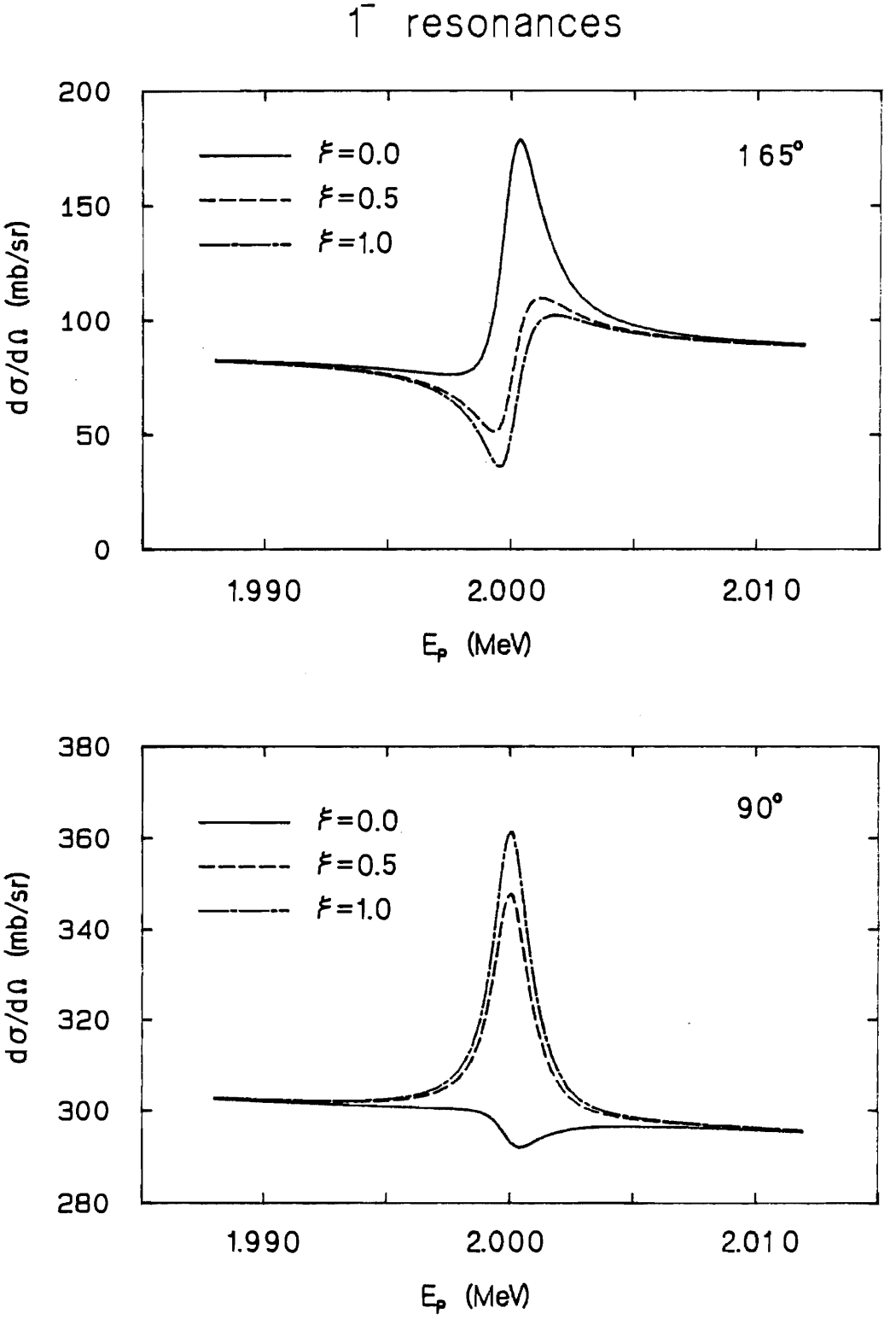
1⁻ resonances
200
150
100
50
0
dσ/dΩ (mb/sr)
f=0.0
f=0.5
f=1.0
165°
1.990
2.000
2.010
Ep (MeV)
380
360
340
320
300
280
dσ/dΩ (mb/sr)
f=0.0
f=0.5
f=1.0
90°
1.990
2.000
2.010
Ep (MeV)

Figure 4.8 Variation in shape for 1^+ resonances with l mixing at 90° and 165°. The changes in shape are striking at both angles.

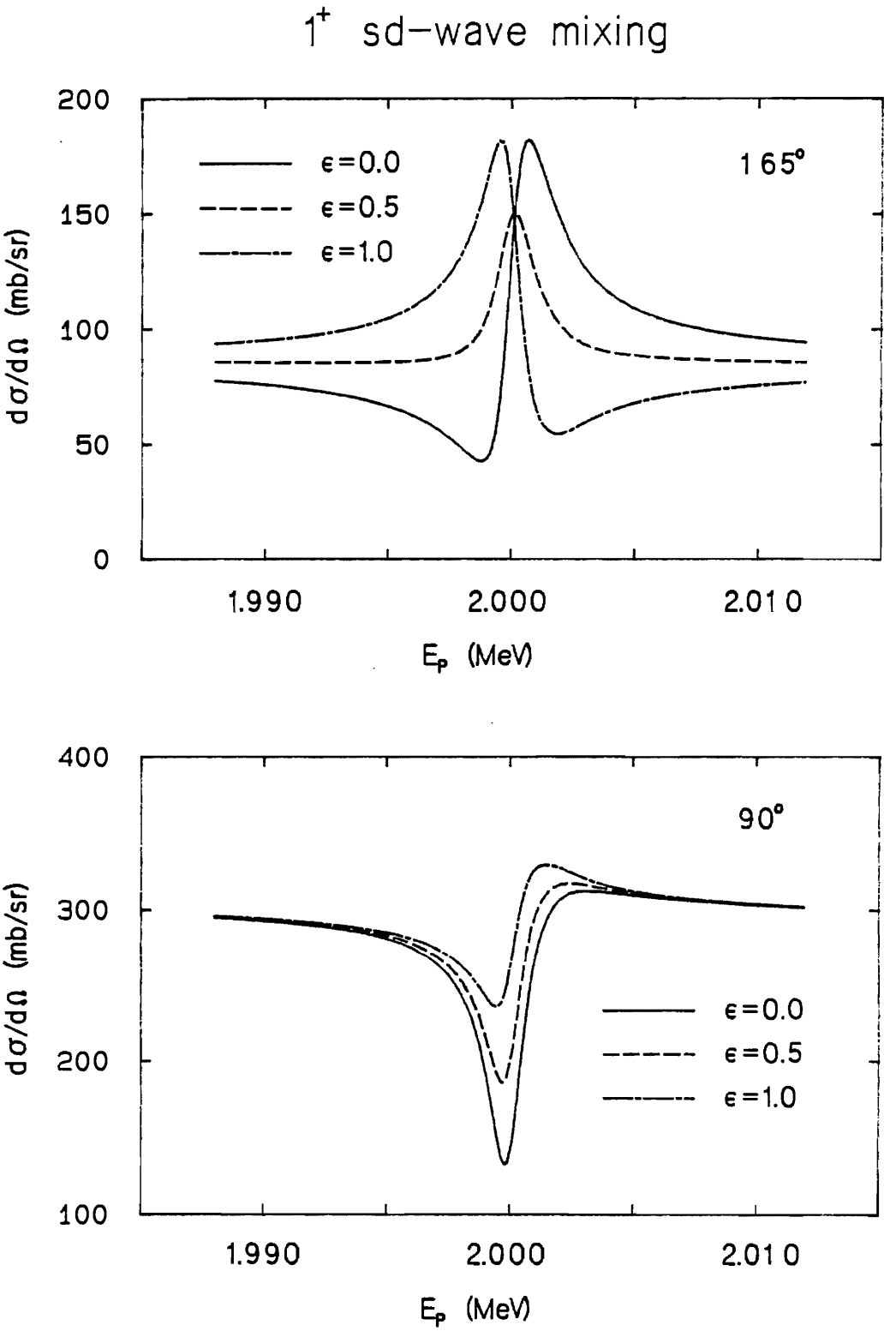
1+ sd-wave mixing
200
150
100
50
0
dσ/dΩ (mb/sr)
ε=0.0
ε=0.5
ε=1.0
165°
1.990
2.000
2.010
Ep (MeV)
400
300
200
100
dσ/dΩ (mb/sr)
90°
ε=0.0
ε=0.5
ε=1.0
1.990
2.000
2.010
Ep (MeV)

Figure 4.9 Variation in shape for 2^- resonances with l mixing at 90° and 165°. The change in shape is striking at 165°, while at 90° the shapes are almost the same.

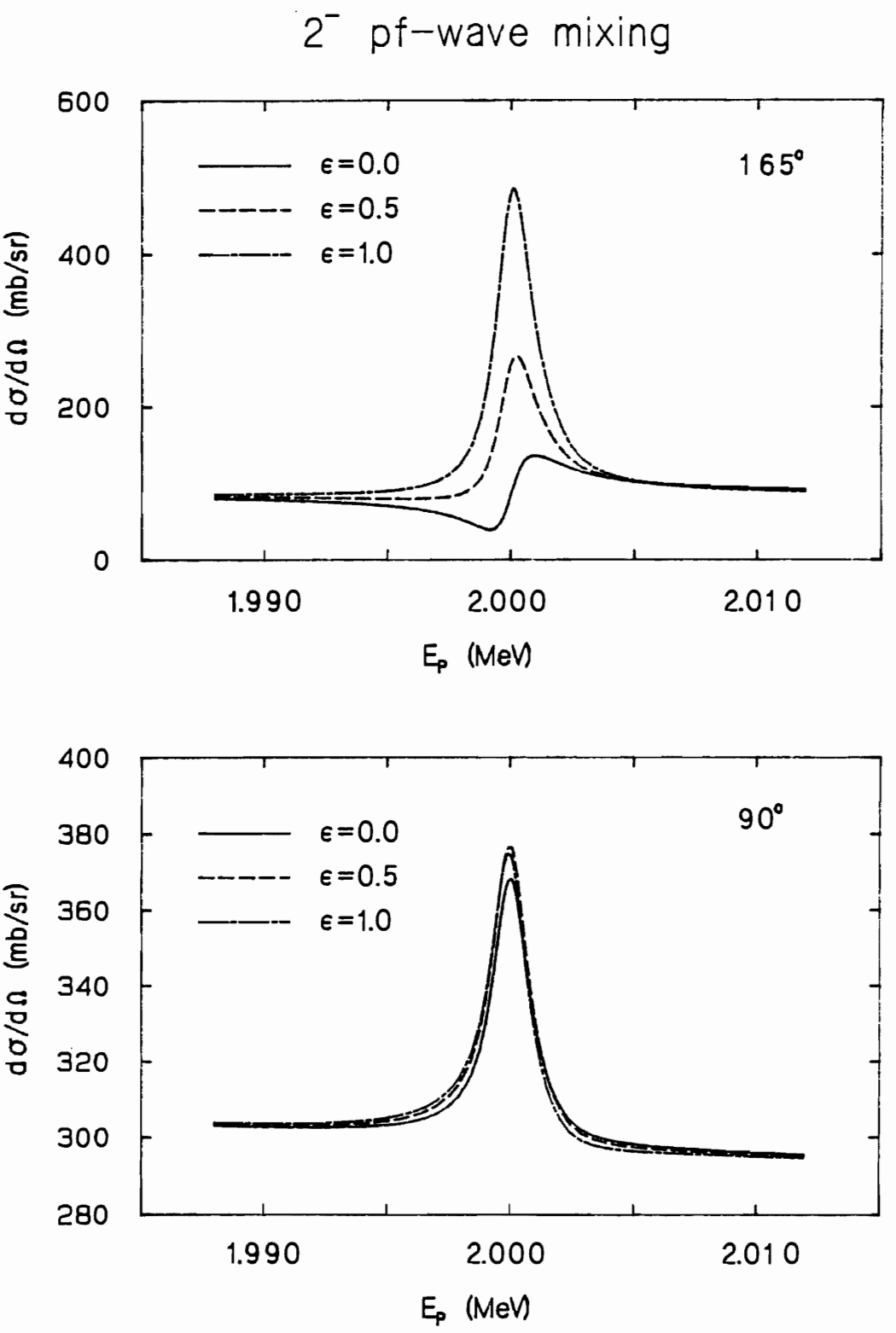
2⁻ pf-wave mixing
600
400
200
0
dσ/dΩ (mb/sr)
ε=0.0
ε=0.5
ε=1.0
165°
1.990
2.000
2.010
Ep (MeV)
400
380
360
340
320
300
280
dσ/dΩ (mb/sr)
ε=0.0
ε=0.5
ε=1.0
90°
1.990
2.000
2.010
Ep (MeV)

Figure 4.10 Variation in shape for 2^+ resonances with channel spin mixing. The change in shape is insensitive to the channel spin mixing near $\xi = 1$. At 90° the shapes for $\xi = 0$ and $\xi = 1$ are identical.

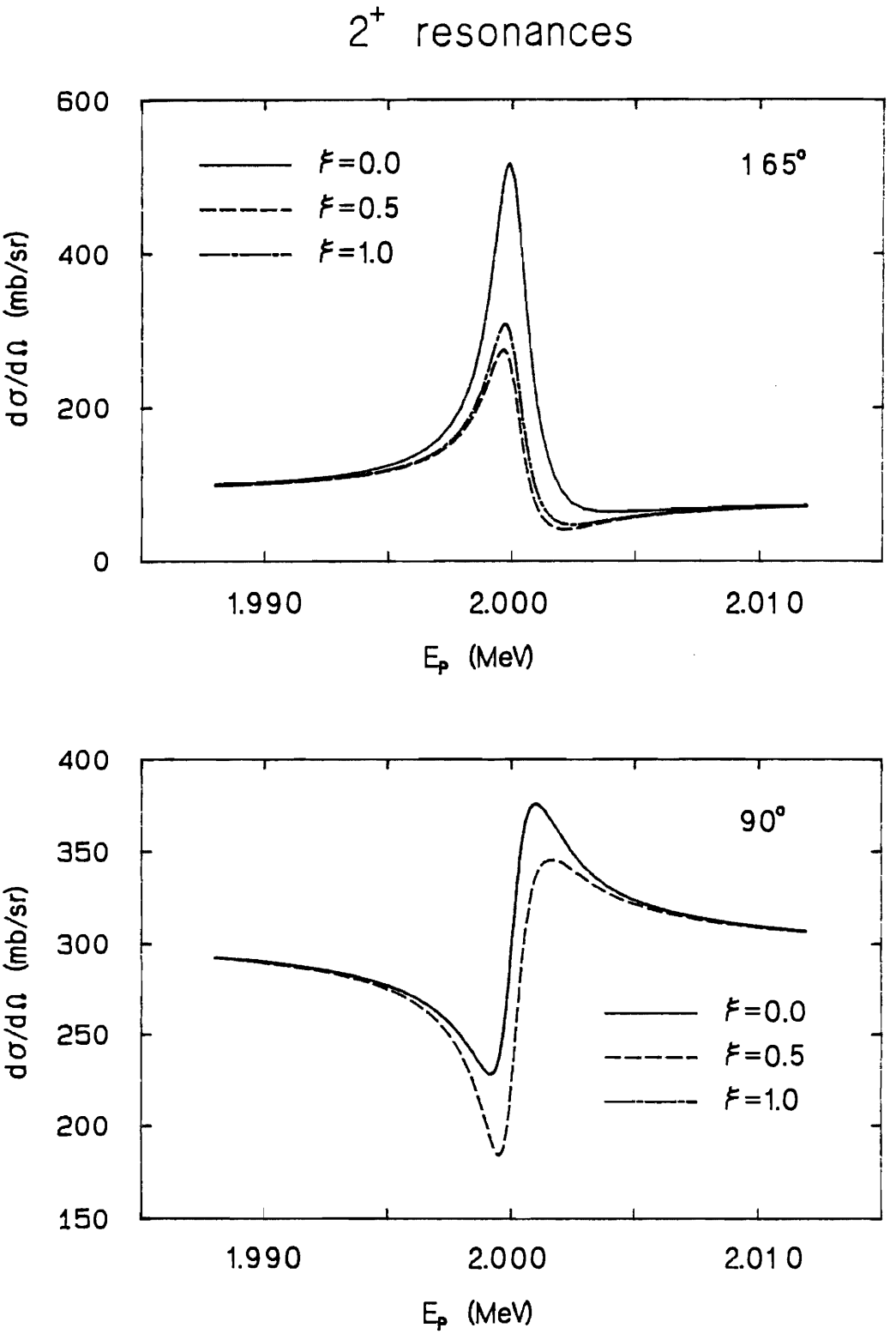
2+ resonances
600
400
200
0
dσ/dΩ (mb/sr)
f=0.0
f=0.5
f=1.0
165°
1.990
2.000
2.010
Ep (MeV)
400
350
300
250
200
150
dσ/dΩ (mb/sr)
90°
f=0.0
f=0.5
f=1.0
1.990
2.000
2.010
Ep (MeV)

C. Nonelastic Channels and Level-Level Interference

In addition to the elastic channel, excited states of ^{32}S can decay to the first excited state of ^{31}P by emitting a proton and subsequently γ decaying to the ground state. For α-cluster nuclei (^{12}C, ^{16}O, ^{20}Ne, ^{24}Mg, ^{28}Si, ^{32}S,...), the excited states also have strong α decay channels. The penetrabilities for both decay channels are shown in figure 4.11. There is a higher Coulomb barrier for α decay, but (p, α_0) reactions usually have a positive reaction Q-value. For $^{31}P(p, \alpha_0)$, the Q-value is 1.916 MeV. In the present experimental data, α_0 peaks can be observed at low energies (~ 1 MeV), while inelastic scattering resonances did not appear until $E_p = 2.40$ MeV.

The α_0 decay is very helpful in the data analysis. First, the presence of α_0 decay to the ^{28}Si ground state requires natural parity ($\pi = (-1)^J$). The other advantage is that there is no exit channel spin mixing in the (p, α_0) reaction and therefore the α_0 angular distribution can help to unambiguously determine the entrance s- or l-mixing ratios. Figure 4.12 shows the $^{31}P(p, \alpha_0)$ angular distributions as a function of s-mixing for all the natural parity states up to $J = 3$. These patterns were generated with the expressions derived from the angular correlation approach discussed in Chapter II.

Proton inelastic scattering (p, p') and the (p, α_1) reaction are not as helpful as the (p, α_0) reaction, mainly because these reactions can have both entrance and exit s- and l-mixing. The (p,p') and (p, α_1) cross sections are usually small, and the quality of the data is not as good as for elastic scattering. Only approximate solutions usually can be obtained, unless the resonances have both inelastic and α_0 decay channels. This is especially true for those resonances with very small elastic partial widths and large inelastic partial widths. One needs to study other reactions in order to remove these ambiguities.

Another interesting phenomenon is level-level interference, which was briefly discussed in Chapter II. For simplicity, we discuss the two level, many channel case. There are two kinds of interference, involving levels with different J^π and levels with the same J^π. Although the R-matrix is block diagonal in J, in the formula (2.33) the differential cross section is summed over all J. Thus for overlapping resonances with different J values, there is a two level interference term. By

Figure 4.11 Coulomb penetrabilities versus energy for $^{31}P(p, p_1)$ and (p, α_1) reactions. The penetrabilities below $E_p = 2.00$ MeV are not shown.

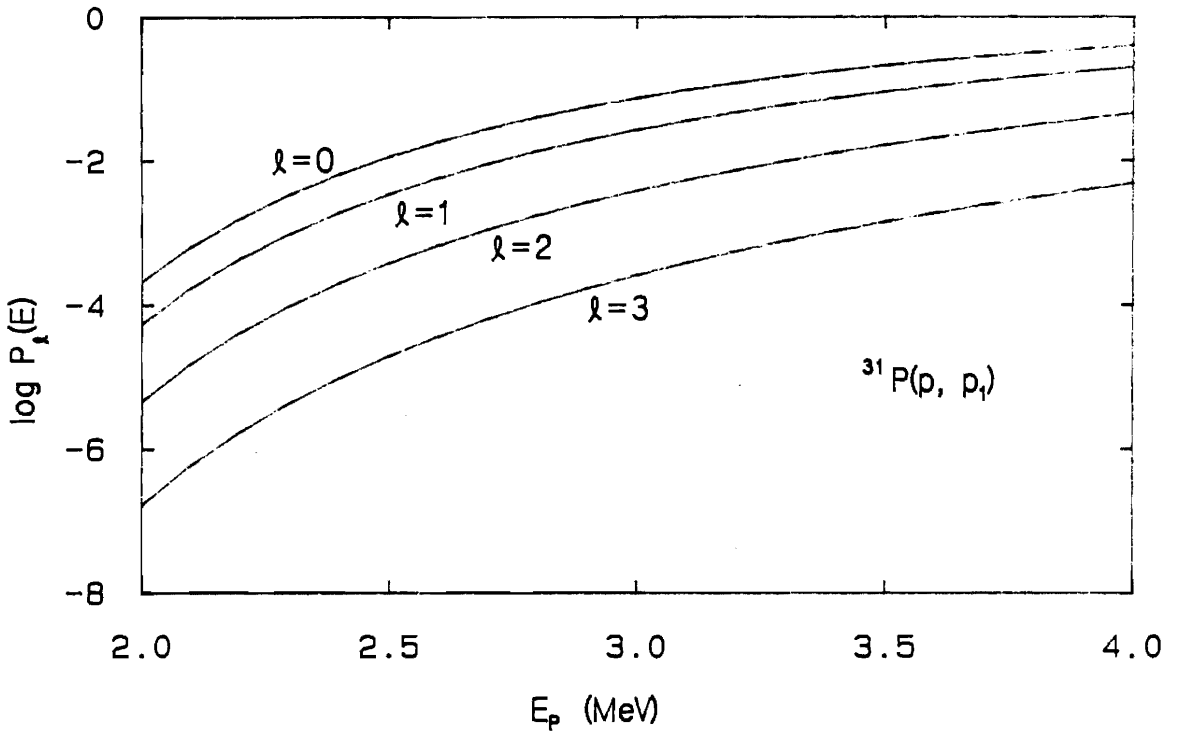
0
-2
-4
-6
-8
log $P_\ell(E)$
ℓ=0
ℓ=1
ℓ=2
ℓ=3
$^{31}P(p, p_1)$
2.0
2.5
3.0
3.5
4.0
E_p (MeV)

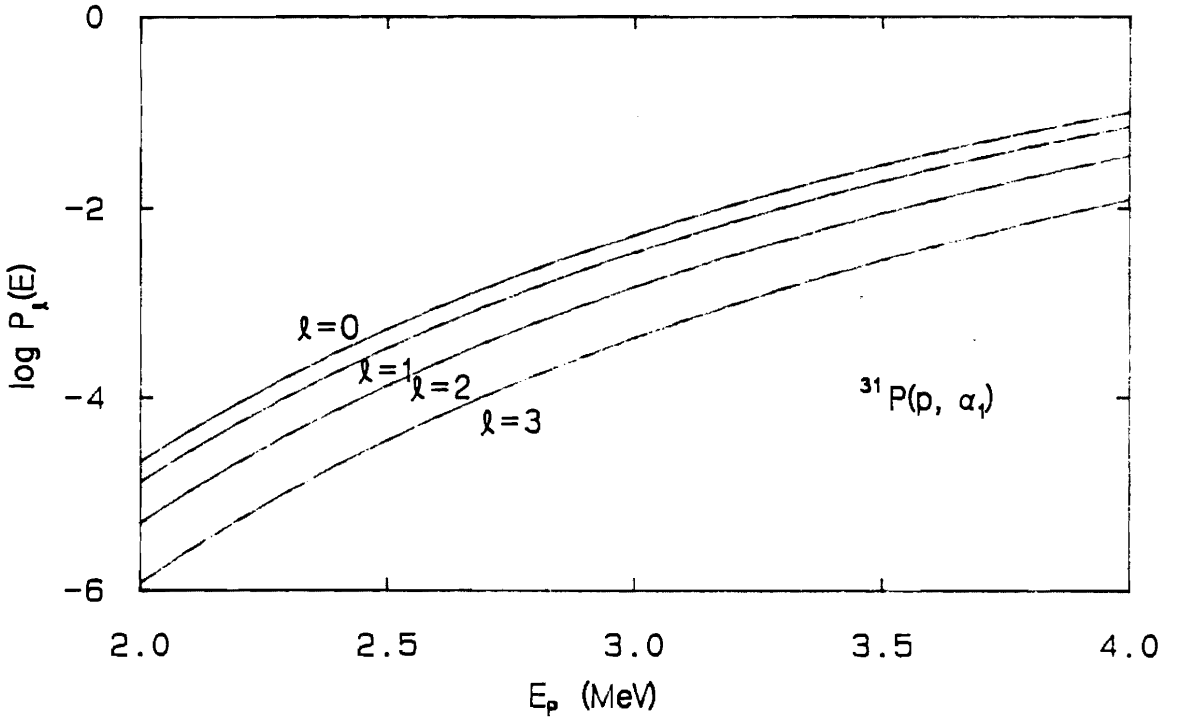
0
-2
-4
-6
log $P_\ell(E)$
ℓ=0
ℓ=1
ℓ=2
ℓ=3
$^{31}P(p, \alpha_1)$
2.0
2.5
3.0
3.5
4.0
E_p (MeV)

Figure 4.12 Catalog for $^{31}P(p, \alpha_0)$ angular distributions. Distributions for various J^π values and channel spin mixing ratios are shown. The angular range for each plot is 90° to 180°.

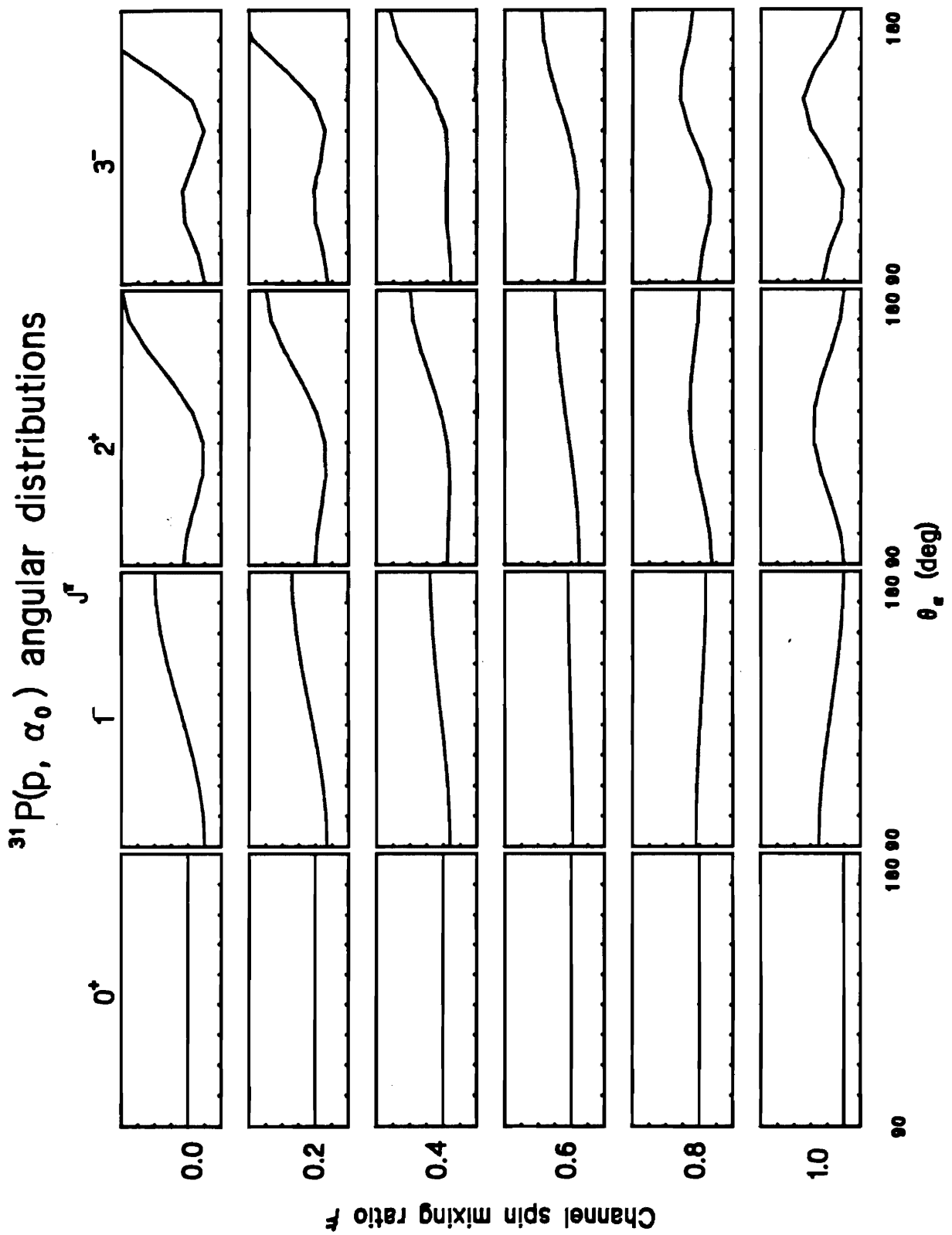
$^{31}P(p, \alpha_0)$ angular distributions
J^π
0⁺
1⁻
2⁺
3⁻
Channel spin mixing ratio r_s
0.0
0.2
0.4
0.6
0.8
1.0
90
180 90
$\theta_{c.m.}$ (deg)

using expression (2.33) and resonance parameters $J_1^{\pi 1}$, $J_2^{\pi 2}$, l_1, l_1', l_2, l_2' associated with each resonance, the interference term of the cross section can be written as

$$\left(\frac{d\sigma_{\eta,\eta'}}{d\Omega_{\eta'}}\right) = \frac{1}{2k'^2_a(2s+1)} \sum_{\substack{ss'l_1l_1' \\ l_2l_2'L}} \frac{(-1)^{s-s'}\Gamma_{1c}^{1/2}\Gamma_{1c'}^{1/2}\Gamma_{2c}^{1/2}\Gamma_{2c'}^{1/2}\cos(\delta+\delta_2-\delta_1)}{[(E_1-E)^2+\frac{1}{4}\Gamma_1^2]^{1/2}[(E_2-E)^2+\frac{1}{4}\Gamma_2^2]^{1/2}}$$

$$\bar{Z}(I_1J_1l_2J_2,sL)\bar{Z}(l'_1J_1l'_2J_2,s'L)P_L(\cos\theta_{\eta'}), \qquad (4.5)$$

where $\delta=\omega_{l_1}+\omega_{l'_1}-\omega_{l_2}-\omega_{l'_2}+\phi_{l_2}+\phi_{l'_2}-\phi_{l_1}-\phi_{l'_1}$ and $\delta_\lambda=\tan^{-1}(\Gamma_\lambda/2(E_\lambda-E))$ are the nuclear phase shifts, and $c=\{\alpha sl\}$. From the symmetry properties of the Z coefficients, one can easily obtain the selection rules for the interference effects:

$$l_1+l_2-L=\text{even} \qquad \text{and/or} \qquad l'_1+l'_2-L=\text{even}.$$

For states with opposite parities the interference term only involves Legendre polynomials with odd L values, while for states with the same parity (but different J) only even L values are involved. The former case introduces asymmetry about $\theta=90°$, which was observed in (p, γ) reaction studies (Devons *et al.* 1952). From the expression (4.5), the interference effects are dominated by the largest terms in the product of partial width amplitudes $\Gamma_{1c}^{1/2}\Gamma_{1c'}^{1/2}\Gamma_{2c}^{1/2}\Gamma_{2c'}^{1/2}$ with specific $\{s, s', l_1, l'_1, l_2, l'_2\}$ values. The overall sign of the product is important, since one can maximize or minimize the interference effects by changing relative signs of these partial width amplitudes with specific $\{s, s', l_1, l'_1, l_2, l'_2\}$ values.

As an example, Table 4.1 lists partial widths, and the product term for two levels with different J^π. Resonance 1 is a broad 1^- state at $E_p = 2.0220$ MeV, which has a large α_0 width, while resonance 2 is a narrow 2^+ state at $E_p = 2.0233$ MeV. In the α_0 decay channel there is only one value for s' and l' for each resonance. Thus only two terms in the partial width amplitude products are left in the summation of (4.5) for the (p, α_0) reaction with target spin $s_t = 1/2$. Due to the phase factor $(-1)^{s-s'}$, one can change signs to make the two terms both positive, both negative, or have opposite signs (together with the phase factor $(-1)^{s-s'}$) as shown in column 9. Figures 4.12(a), 4.12(b), 4.13(a) and 4.13(b) show these effects at 127° and 165°. For two different J^π levels, the interference term (4.5) is zero at 90°. From equation (4.5), one can also see that the

Table 4.1 Level Interference Effects

Resonance 1 ($J^\pi = 1^-$)				Resonance 2 ($J^\pi = 2^+$)				$(-)^{s-s'}\Pi$ [a]	Figure
s	Γ_p [b]	s'	Γ_α	s	Γ_p	s'	Γ_α	(keV)^2	
0	8.50	0	3.00	0	0.15	0	0.14	0.73	4.12(a)
1	−10.50 [c]			1	0.03			0.36	
0	− 8.50 [c]	0	3.00	0	0.15	0	0.14	− 0.73	4.12(b)
1	10.50			1	0.03			− 0.36	
0	8.50	0	3.00	0	0.15	0	0.14	0.73	4.13(a)
1	10.50			1	0.03			− 0.36	
0	8.50	0	−3.00 [c]	0	0.15	0	0.14	− 0.73	4.13(b)
1	10.50			1	0.03			0.36	

a) $\Pi = \Gamma_{1c}^{1/2}\Gamma_{1c'}^{1/2}\Gamma_{2c}^{1/2}\Gamma_{2c'}^{1/2}$

b) Resonance widths are in units of keV. For resonance 1, $l = l' = 1$ and for resonance 2, $l = l' = 2$.

c) Signs are associated with resonance width amplitude $\Gamma_c^{1/2}$.

Figure 4.13 (a) Two level interference effects at 127° and 165°. The dots are the experimental data and the solid curve is the fit with a negative proton partial width (s = 1) amplitude for resonance 1. The pattern will be the same if the negative sign is assigned to the proton width (s = 1) of resonance 2. (b) All the fitting parameters are the same as (a) except the negative sign is assigned to one of the (two resonance) s = 0 proton partial width amplitudes.

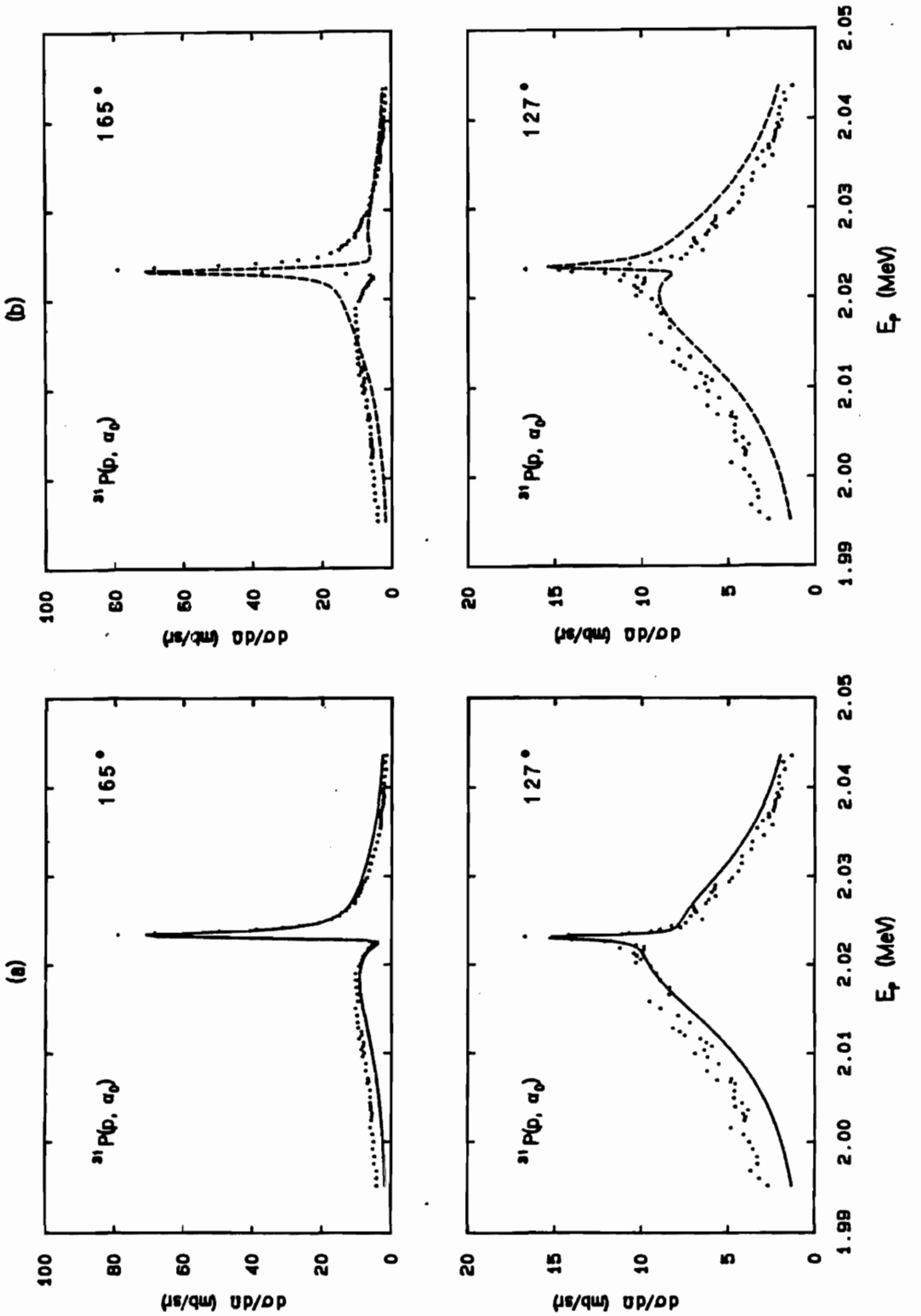
(a)
(b)
^{31}P(p, α_0)
165°
127°
dσ/dΩ (mb/sr)
E_p (MeV)
1.99
2.00
2.01
2.02
2.03
2.04
2.05
0
5
10
15
20
20
40
60
80
100

Figure 4.14 (a) The fitting parameters are the same as in figure 4.13(a) except that all the partial width amplitudes are positive. (b) The fitting parameters are the same as in figure 4.13(a) except the negative sign is assigned to the one of the α width amplitudes.

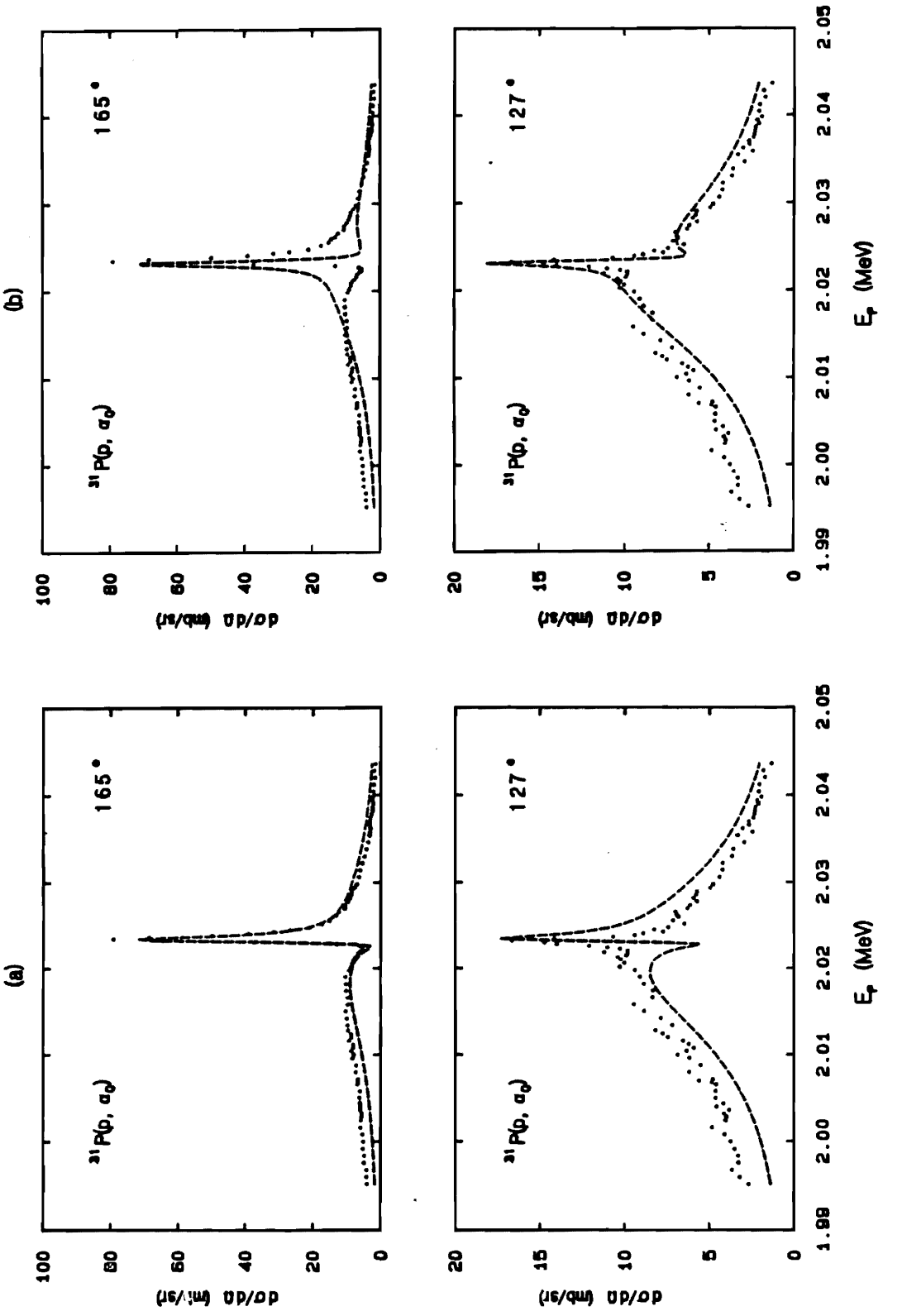
(a)
(b)
^{31}P(p, α_0)
165°
127°
dσ/dΩ (mb/sr)
dσ/dΩ (mb/sr)
E$_p$ (MeV)
E$_p$ (MeV)

shape of interference will be the same if the sign of the resonance partial width amplitude is assigned to the other resonance. In Table 4.1, those signs are associated with resonance 1. For the elastic channel with spin flip exit channel, for the inelastic channel or for target spin 3/2, 5/2,..., the sign effects are too complicated to predict due to the increasing numbers of combinations of partial width amplitudes.

A different level-level interference effect arises for two levels with the same J^{π}. Using the level expansion discussed in chapter II, one obtains the level matrix elements $A_{\lambda\lambda'}$ for two levels:

$$A_{11} = (E_2 - E + i\Gamma_2/2)/D \qquad A_{22} = (E_1 - E + i\Gamma_1/2)/D$$

$$A_{12} = A_{21} = (i\Gamma/2)/D$$

where $D = [(E_1-E) + i\Gamma_1/2][(E_2-E) + i\Gamma_2/2] + \Gamma_{12}^2/4$, and $\Gamma_{12} = \sum_c \Gamma_{1c}^{1/2}\Gamma_{2c}^{1/2}$. The reaction term of the differential cross section is proportional to TT^*. Using expression (2.38) for two levels with the same J^{π} in reaction channels, TT^* is found to be:

$$\begin{aligned}
&(T_{\alpha's'l'_1,\alpha sl_1})(T_{\alpha's'l'_2,\alpha sl_2})^* \\
&= [P_{c1}^{1/2}P_{c'1}^{1/2}[\sum_{\lambda\mu}(\gamma_\lambda\times\gamma_\mu)A_{\lambda\mu}]_{c1c'1}][P_{c2}^{1/2}P_{c'2}^{1/2}[\sum_{\eta\sigma}(\gamma_\eta\times\gamma_\sigma)A_{\eta\sigma}]^*_{c2c'2}] \\
&= A_{11}A_{11}^*(\Gamma_{1c1}^{1/2}\Gamma_{1c'1}^{1/2}\Gamma_{1c2}^{1/2}\Gamma_{1c'2}^{1/2}) + A_{22}A_{22}^*(\Gamma_{2c1}^{1/2}\Gamma_{2c'1}^{1/2}\Gamma_{2c2}^{1/2}\Gamma_{2c'2}^{1/2}) \\
&+ A_{12}A_{12}^*(\Gamma_{1c1}^{1/2}\Gamma_{2c'1}^{1/2} + \Gamma_{2c1}^{1/2}\Gamma_{1c'1}^{1/2})(\Gamma_{1c2}^{1/2}\Gamma_{2c'2}^{1/2} + \Gamma_{2c2}^{1/2}\Gamma_{1c'2}^{1/2}) \\
&+ A_{11}A_{22}^*(\Gamma_{1c1}^{1/2}\Gamma_{1c'1}^{1/2}\Gamma_{2c2}^{1/2}\Gamma_{2c'2}^{1/2}) + A_{22}A_{11}^*(\Gamma_{2c1}^{1/2}\Gamma_{2c'1}^{1/2}\Gamma_{1c2}^{1/2}\Gamma_{1c'2}^{1/2}) \qquad (4.6) \\
&+ A_{11}A_{12}^*(\Gamma_{1c2}^{1/2}\Gamma_{2c'2}^{1/2} + \Gamma_{2c2}^{1/2}\Gamma_{1c'2}^{1/2})\Gamma_{1c1}^{1/2}\Gamma_{1c'1}^{1/2} + A_{12}A_{11}^*(\Gamma_{1c1}^{1/2}\Gamma_{2c'1}^{1/2} + \Gamma_{2c1}^{1/2}\Gamma_{1c'1}^{1/2})\Gamma_{1c2}^{1/2}\Gamma_{1c'2}^{1/2} \\
&+ A_{22}A_{12}^*(\Gamma_{1c2}^{1/2}\Gamma_{2c'2}^{1/2} + \Gamma_{2c2}^{1/2}\Gamma_{1c'2}^{1/2})\Gamma_{2c1}^{1/2}\Gamma_{2c'1}^{1/2} + A_{12}A_{22}^*(\Gamma_{1c1}^{1/2}\Gamma_{2c'1}^{1/2} + \Gamma_{2c1}^{1/2}\Gamma_{1c'1}^{1/2})\Gamma_{2c2}^{1/2}\Gamma_{2c'2}^{1/2}
\end{aligned}$$

The subscripts for the partial width amplitudes are level numbers, the particle pair and channel spin and the angular momentum for the channels. For example, Γ_{1c1} is the width for level number 1, incident channel c, with angular momentum l_1 which will be summed over in the differential cross section expressions; $\Gamma_{2c'2}$ is the width for level number 2, exit channel c' with value l'_2. The first two terms of equation (4.6) are single resonance expressions for each level; the rest of the terms will contribute to the interference. It is impractical to obtain the explicit expression for the differen-

tial cross section in the general case. However, one can discuss the general behavior by integrating the differential cross section (2.38) over the solid angle $\Omega_{\alpha'}$. In this integration only the B_0 contribution is non-vanishing. Using the relation

$$\bar{Z}\ (l_1 J_1 l_2 J_2, s\ 0) = \delta_{l_1 J_1, l_2 J_2}\,(-1)^{J_2 - s}(2J+1)\ ,$$

one obtains the result

$$\sigma_{\alpha s,\alpha' s'} = \frac{\pi}{k_a^{\,2}(2s+1)} \sum_{Jll'} (2J+1)\,|\,T^{J}_{\alpha' s' l',\alpha s l}\,|^2 . \qquad (4.7)$$

In other words, the total cross section for a specific channel only involves diagonal elements of the T matrix. Using equation (4.6), one obtains the expression for the total cross section for the interference of two levels with the same J^{π}:

$$\sigma_{\alpha s,\alpha' s'} = \frac{\pi g_J}{k_\alpha^{\,2}(2s+1)} \sum_{ll'} \frac{[(E_2-E)\Gamma_{1c}^{1/2}\Gamma_{1c'}^{1/2}+(E_1-E)\Gamma_{2c}^{1/2}\Gamma_{2c'}^{1/2}]^2+\frac{1}{4}[\sum_{c''}\Pi_{c''c}\Pi_{c''c'}]^2}{[(E_1-E)(E_2-E)+\frac{1}{4}(\Gamma_{12}^2-\Gamma_1\Gamma_2)]^2+\frac{1}{4}[\Gamma_1(E_2-E)+\Gamma_2(E_1-E)]^2}\ , \qquad (4.8)$$

where $\Pi_{c''c} = \Gamma_{1c''}^{1/2}\Gamma_{2c}^{1/2} - \Gamma_{2c''}^{1/2}\Gamma_{1c}^{1/2}$ and $\Gamma_{12} = \Sigma_{c''} 2P_{c''}\gamma_{1c''}\gamma_{2c''}$, and $P_{c''}$ is the penetrability for channel c''. From this formula, one can see that the reaction cross section vanishes only if the products $\Gamma_{1c}^{1/2}\Gamma_{1c'}^{1/2}$ and $\Gamma_{2c}^{1/2}\Gamma_{2c'}^{1/2}$ have the same sign.

The differential cross section expression can be derived for more limited cases. Consider the (p,α_0) reaction from spin 1/2 targets. As discussed before, all the resonances must have natural parity and only one l value for both the entrance and exit channel. Thus equation (4.6) can be simplified. Following almost the same procedure as deriving (4.8), one has

$$\left(\frac{d\sigma_{p\alpha}}{d\Omega_\alpha}\right) = \frac{1}{4k_\alpha^{\,2}(2s+1)} \sum_{JL} \frac{(-1)^s\,[(E_2-E)\Gamma_{1p}^{1/2}\Gamma_{1\alpha}^{1/2} + (E_1-E)\Gamma_{2p}^{1/2}\Gamma_{2\alpha}^{1/2}]^2 + \frac{1}{4}[\sum_{c''}\Pi_{c''p}\Pi_{c''\alpha}]^2}{[(E_1-E)(E_2-E) + \frac{1}{4}(\Gamma_{12}^2-\Gamma_1\Gamma_2)]^2 + \frac{1}{4}[\Gamma_1(E_2-E) + \Gamma_2(E_1-E)]^2}$$

$$\times \bar{Z}\ (lJlJ, sL)\bar{Z}\ (lJlJ, 0L)P_L(\cos\theta_\alpha)\ , \qquad (4.9)$$

where s is the incident channel spin, and $l = l'$, $s' = 0$ are used; the definitions for Γ_{12} and $\Pi_{c''c}$ are the same as in (4.8). In general, for elastic scattering with s- and l- mixing, and for the (p, α_0) reaction from higher spin targets (3/2, 5/2,...), the effects of the relative phase associated with the

reduced width amplitudes of the two resonances are even more complicated.

Vogt (1958) proposed another method for handling the resonance interference. Consider a system having N levels with a large number of open exit channels. The channel number is not exactly known due to some of the channels having very small laboratory widths. The level matrix **A** has $N(N-N)/2$ independent non-diagonal elements. Vogt's suggestion was to parametrize these elements and redefine them. The definition of the width vector is:

$$g_\lambda = \sum_c^m e_c \Gamma_{\lambda c}^{1/2},$$

where e_c is the unit vector for each channel c, m is the total number of the channels (assumed orthogonal), and $|g_\lambda| = |g_\lambda \cdot g_\lambda| = (\Sigma\Gamma_{\lambda c})^{1/2} = \Gamma_\lambda^{1/2}$. From the expression for the level matrix **A** (2.37), one has

$$A_{\lambda\lambda'}^{-1} = \frac{-i}{2}\sum_c \Gamma_{\lambda c}^{1/2}\Gamma_{\lambda' c}^{1/2} = \frac{-i}{2} g_\lambda \cdot g_{\lambda'} \qquad (4.10)$$

Thus the system can be described as an N vector $\{g_\lambda\}$ system in the vector space which has a dimension m. One can choose a unit vector $g_\lambda / |g_\lambda|$ from one of the low-lying levels as the base vector and parametrize the relationship between the levels as the angles $\theta_{\lambda\lambda'}$ between the vectors. Thus all the non-diagonal elements of **A** can be expressed as $N(N-N)/2$ parameters $\theta_{\lambda\lambda'}$, or

$$A_{\lambda\lambda'}^{-1} = \frac{-i}{2}(\Gamma_\lambda \Gamma_{\lambda'})^{1/2}\cos\theta_{\lambda\lambda'},$$

where the definition of $\theta_{\lambda\lambda'}$ is

$$\cos\theta_{\lambda\lambda'} = \frac{\sum_c \Gamma_{\lambda c}^{1/2}\Gamma_{\lambda' c}^{1/2}}{[(\sum_c \Gamma_{\lambda c})(\sum_c \Gamma_{\lambda' c})]}. \qquad (4.11)$$

Obviously, if there is only one open channel, the vectors will be either parallel or anti-parallel, which results in $\cos\theta_{\lambda\lambda'} = \pm 1$, and the interference effects will be simple and clear. If the number of open channels m is very large and the signs of the width amplitudes are random, one can expect the inner products of the vectors to be zero; in other words, the width vectors are orthogonal to each other: in this case, $\cos\theta_{\lambda\lambda'} = 0$. From the definition of $\theta_{\lambda\lambda'}$ and the two extreme cases, one

can see that the detailed sign distribution among the components of the width vector is averaged and represented as the correlation angles $\theta_{\lambda\lambda'}$. The value of the correlation angles $\theta_{\lambda\lambda'}$ depends on the number of open channels, the partial width amplitudes and their signs. If the signs are randomly distributed and the norm of the partial width amplitudes $|\Gamma_{\lambda c}^{1/2}|$ is a Gaussian distribution, and each channel has the same probability, then the average value of $cos\theta_{\lambda\lambda'}$ along the spherical surface of m dimensions is found to be

$$<|cos\theta_{\lambda\lambda'}|> = \frac{(m-1)}{2^{m-1}[\frac{1}{2}(m-1)!]^2} \qquad m = \text{odd}$$

$$= \frac{2(m-1)!}{\pi} \frac{1}{[(m-1)!!]^2} . \qquad m = \text{even}$$

Thus, the correlation angle $\theta_{\lambda\lambda'}$ can provide not only the description of level-level interference, but also a method for determination of the number of open channels.

Vogt's theory is very useful for nuclear fission, which usually has a large number of fission channels and strong level-level interference. Unfortunately, in the present experiment the channel number is not large enough to test Vogt's theory. However, one can discuss some features of the level-level interference effects in terms of the correlation angles $\theta_{\lambda\lambda'}$. Note that the inversion of the level matrix **A** can be written as a sum of the diagonal matrix **D** and non-diagonal matrix **N**:

$$\mathbf{A}^{-1} = \mathbf{D} + \mathbf{N} ,$$

where $$D_{\lambda\lambda'} = (E_\lambda - E - i\Gamma_\lambda/2)\delta_{\lambda\lambda'}$$

$$N_{\lambda\lambda'} = \frac{-i}{2}(1 - \delta_{\lambda\lambda'})g_\lambda \cdot g_{\lambda'} .$$

The matrix **A** can be approximated as

$$\mathbf{A} = (\mathbf{D} + \mathbf{N})^{-1} = \mathbf{D}^{-1}(\mathbf{1} - \mathbf{N}\mathbf{D}^{-1} + \mathbf{N}\mathbf{D}^{-1}\mathbf{N}\mathbf{D}^{-1} + \dots) . \qquad (4.12)$$

Taking the first order of (4.12), one has

$$\mathbf{A} = \mathbf{D}^{-1} - \mathbf{D}^{-1}\mathbf{N}\mathbf{D}^{-1}$$

or $$A_{\lambda\lambda'} = \frac{\delta_{\lambda\lambda'}}{Z_\lambda} + \frac{i}{2}(1-\delta_{\lambda\lambda'})\frac{G_{\lambda\lambda'}}{Z_\lambda Z_{\lambda'}} , \qquad (4.13)$$

where $G_{\lambda\lambda'} = g_\lambda \cdot g_{\lambda'}$, and $Z_\lambda = (E_\lambda - E) - i\Gamma_\lambda/2$. The derivation of the differential cross section is very complicated. To simplify the problem, one substitutes (4.13) into the expression (2.38) and writes the total cross section as the sum of two single resonances and the interference term. Assuming $ka<<1$, one obtains the interference term:

$$\sigma_t^{(\lambda\lambda')} = \frac{\pi}{k^2} 2g_J \frac{(E_\lambda - E)(E_{\lambda'} - E)(\Gamma_{\lambda 0}\Gamma_{\lambda' 0}\Gamma_\lambda\Gamma_{\lambda'})^{1/2}}{[(E_\lambda - E)^2 + \frac{1}{4}\Gamma_\lambda^2][(E_{\lambda'} - E)^2 + \frac{1}{4}\Gamma_{\lambda'}^2]} \cos\theta_{\lambda\lambda'} , \quad (4.14)$$

where $\Gamma_{\lambda 0}$ and $\Gamma_{\lambda' 0}$ are the entrance widths for levels λ and λ', respectively. From equation (4.14) one can see that when the distance between the two levels is larger than the widths Γ_λ or $\Gamma_{\lambda'}$, the contribution will be small. The interference maxima occur somewhere within the resonance width $\pm\Gamma_\lambda / 2$ (or $\pm\Gamma_{\lambda'} / 2$), and the value of the interference term will change sign when the energy E passes E_λ or $E_{\lambda'}$. In practice, one adjusts the correlation angle $\theta_{\lambda\lambda'}$ to fit the experimental data. The formula (4.14) is not necessarily very accurate compared with (4.9), but it will be a good approximation for a pair of levels belonging to a set of well-separated resonances, and it can be used more explicitly to give quantitative estimates of the interference effects. Note that in equation (4.11) one can choose the partial width amplitudes and their signs (the total widths for each resonance stay the same) to change the value of $\cos\theta_{\lambda\lambda'}$. An example of the change of the interference pattern is shown in figure 4.15. From figure 4.15 (a) one can see that the interference of two resonances has a striking change as the correlation angle $\theta_{\lambda\lambda'}$ varies, and the contribution to the cross section can be constructive as well as destructive. Because of their change in signs at the resonance energies, the interference terms can cause an asymmetry in the resonance shapes or an energy shift in the resonance position from E_λ as shown in figure 4.15 (b).

The analysis of high resolution elastic scattering and (p,α_0) reaction data provides an excellent survey of compound nuclear states. The energies, parities, widths and most of the spins and the *s*-, *l*- mixing ratios can be determined. Combined with information from other nuclear reactions, one can obtain an almost complete set of resonance parameters, including relative phases, mixing ratios and resonance amplitude correlations (Mitchell *et al.* 1985).

Figure 4.15 (a) Level-level interference term (4.14) for two different correlation angles $\theta_{\lambda\lambda'}$. The resonance widths are 1.5 keV and 4.5 keV. The contribution to the total cross section can be either constructive or destructive when the energy passes the resonance energy. (b) The total cross section of two resonances are shown in arbitrary units. Note the asymmetry caused by the interference effects.

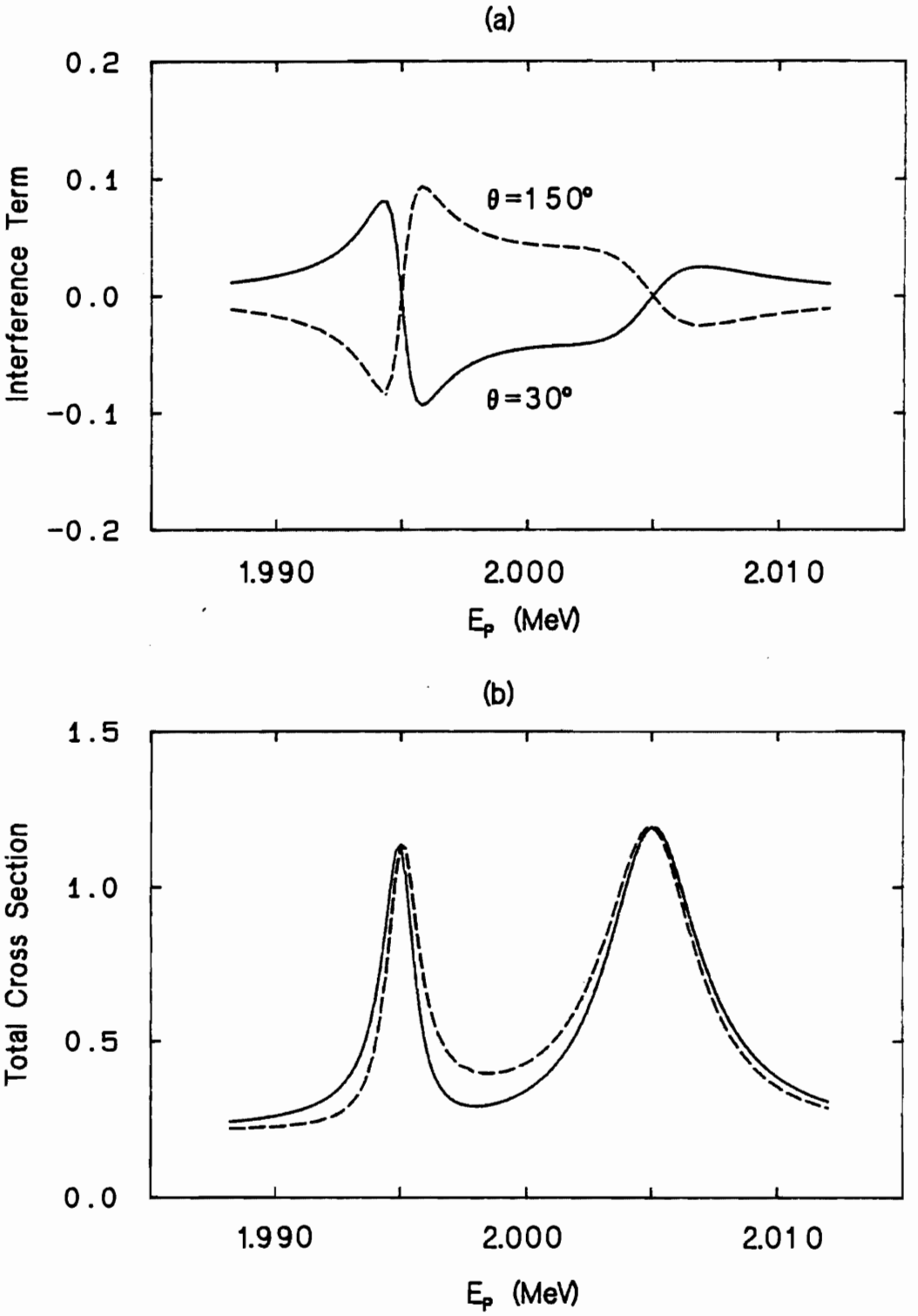
(a)
0.2
0.1
0.0
−0.1
−0.2
Interference Term
θ=150°
θ=30°
1.990
2.000
2.010
Ep (MeV)
(b)
1.5
1.0
0.5
0.0
Total Cross Section
1.990
2.000
2.010
Ep (MeV)

D. Data Presentation

In the present experiment excitation functions were measured in the range E_p = 1.00 to 4.01 MeV, and a total of 143 resonances were observed. Resonances above E_p = 2.05 MeV had not been fit previously except for a 4^-, $T = 1$ state and a 0^+, $T = 2$ state near E_p = 3.285 MeV.

The excitation functions for proton elastic scattering from ^{31}P and for (p, α_0) in the energy range 1.00 to 2.00 MeV are shown in figures 4.16; the exitation functions for (p, p_0), (p, α_0) and (p, p_1) in the range E_p = 2.00 to 3.00 MeV are shown in figure 4.17; the differential cross section for ^{31}P(p, p_0), (p, α_0), (p, p_1) and (p, α_1) channels in the range E_p = 3.00 to 4.00 MeV are shown in figure 4.18. Figure 4.19 shows the differential cross sections for ^{31}P(p, p_0) at 5 angles in the energy range E_p = 2.00 to 3.00 MeV. Overall, the fitting is satisfactory. Typical uncertainties in the resonance parameters are about 10% for small resonances. For large resonances ($\Gamma \geq 15$ keV) the laboratory widths have quite large uncertainties (~20%), especially for resonances whose inelastic widths are larger than their elastic widths.

There is good agreement with the previous experimental data compiled by Endt and Van der Leun (1978) below E_p = 2.050 MeV. In one key experiment, Kalifa *et al.* (1978) performed an extensive study of the nucleus ^{32}S through the ^{31}P$(^3$He,$d)^{32}$S proton transfer reaction, and 111 levels were observed from the ground state to an excitation $E_x(^{32}S)$ = 10.977 MeV (corresponding to E_p = 2.182 MeV). Few measurements have been performed since this compilation. Several resonances below E_p = 2.00 MeV which are observed in the (p, γ) experiments are barely seen in the present experiment due to a small elastic width. For these resonances the laboratory widths have quite large uncertainties; the J^π value for these resonances are taken from Endt's compilation. The major disagreements are: 1) Resonance at E_p = 1.643 MeV whose J^π value was assigned as 1^- is assigned 0^+ from the present experimental data. 2) Resonance at E_p = 1.796 MeV was assigned previously as a 2^+ state with α decay. In this experiment the elastic shape is totally different from the shape for 2^+, and no α decay was observed. This resonance is assigned $J^\pi = 1^-$. 3) Resonances at E_p = 1.280, 1.724 and 1.740 MeV, which were observed in the (p, γ) reaction, are

Figure 4.16 Differential cross sections for $^{31}P(p,p_0)$ at 165° and 90° and $^{31}P(p,\alpha_0)$ at 165° in the energy range E_p = 1.00 to 2.00 MeV. The solid curve is the R-matrix fit.

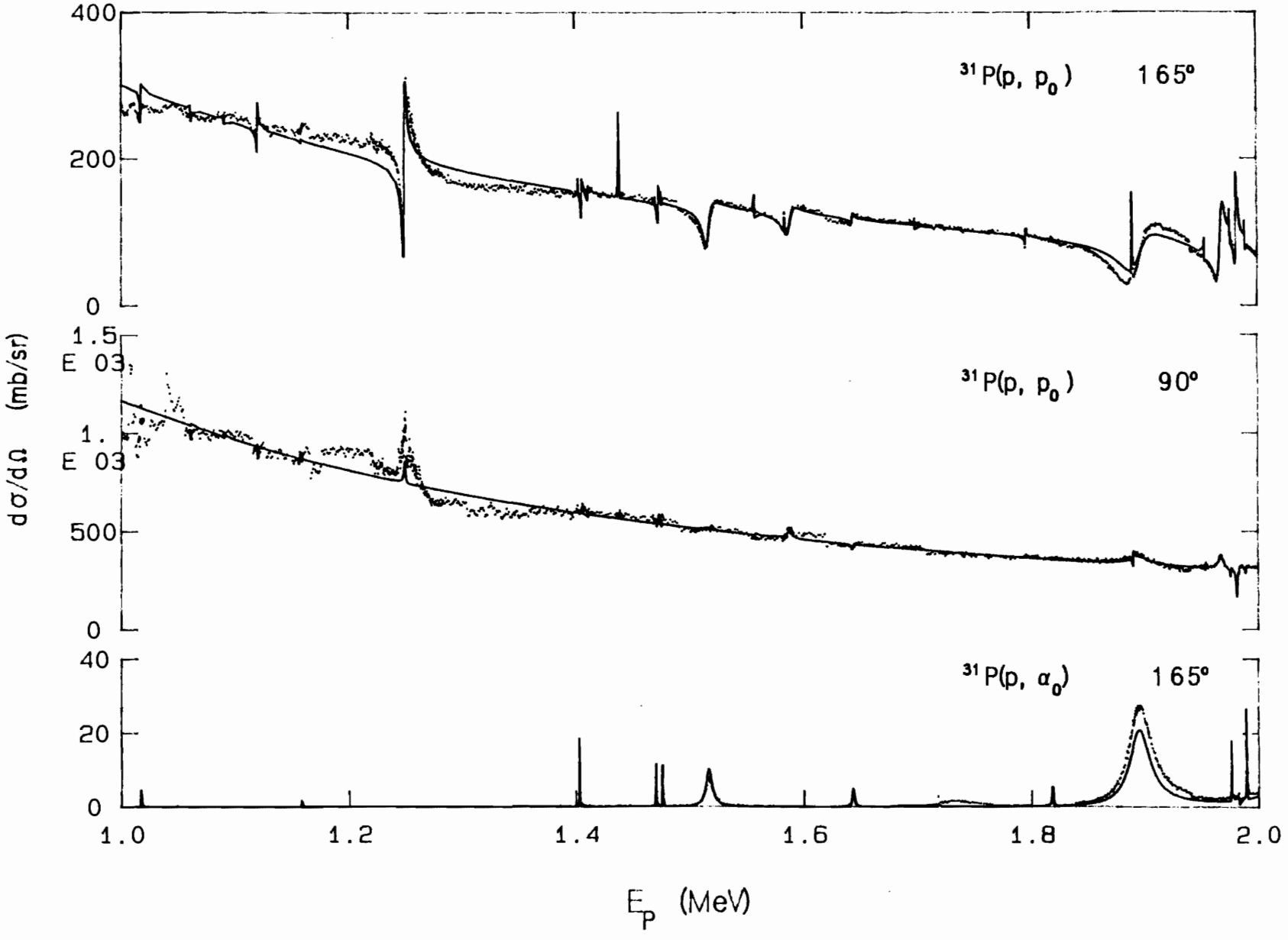
400
200
0
^{31}P(p, p$_0$) 165°
1.5
E 03
1.
E 03
500
0
^{31}P(p, p$_0$) 90°
40
20
0
^{31}P(p, α$_0$) 165°
1.0
1.2
1.4
1.6
1.8
2.0
dσ/dΩ (mb/sr)
E$_P$ (MeV)

Figure 4.17 Differential cross sections for $^{31}P(p, p_0)$, $^{31}P(p, \alpha_0)$ and $^{31}P(p, p_1)$ at 165° in the energy range E_p = 2.00 to 3.00 MeV.

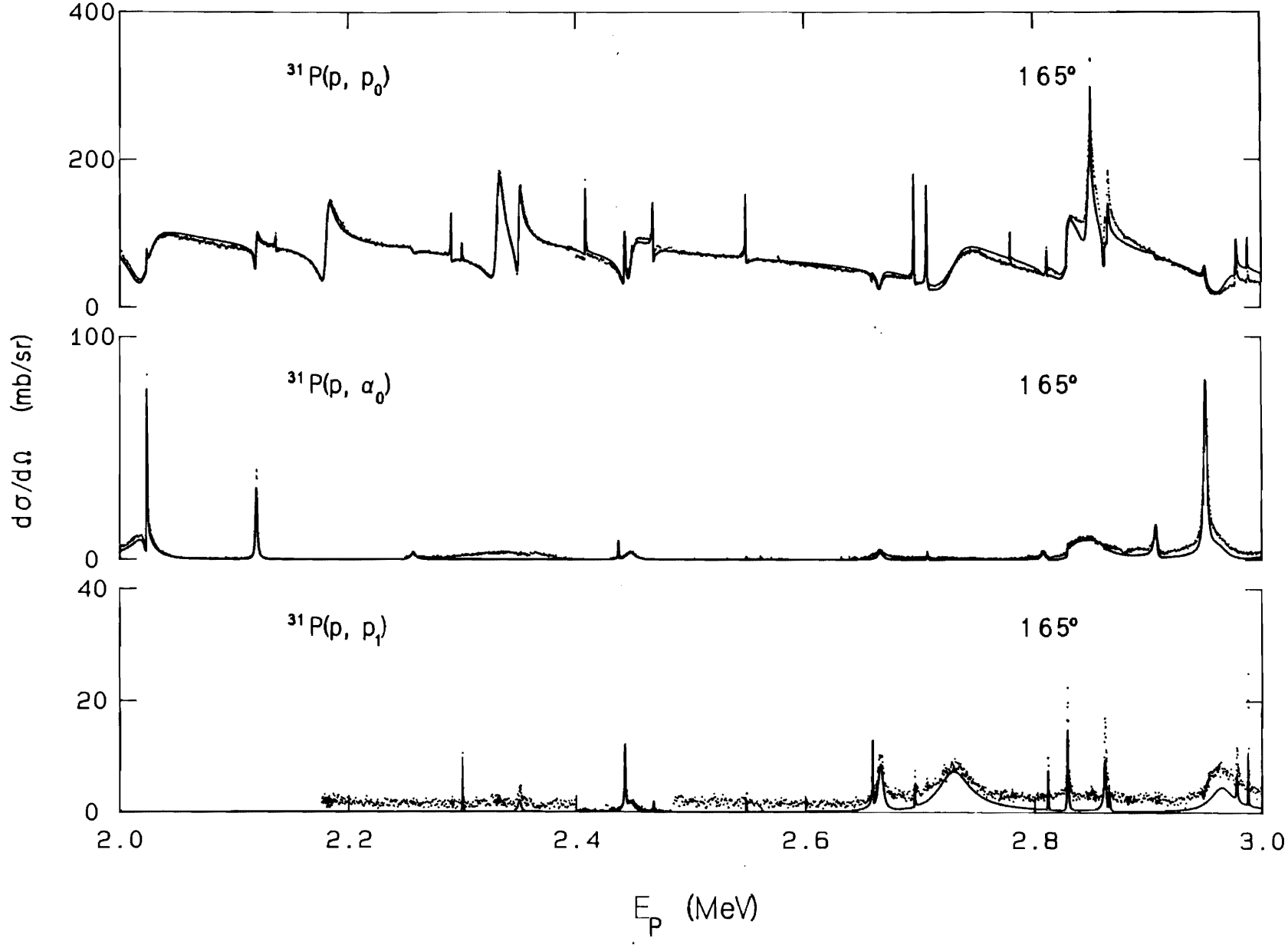
400
200
0
^{31}P(p, p$_0$)
165°
100
0
^{31}P(p, α$_0$)
165°
40
20
0
^{31}P(p, p$_1$)
165°
dσ/dΩ (mb/sr)
2.0
2.2
2.4
2.6
2.8
3.0
E$_P$ (MeV)

Figure 4.18 Differential cross sections for $^{31}P(p, p_0)$, $^{31}P(p, \alpha_0)$ and $^{31}P(p, p_1)$ at 165° and $^{31}P(p, \alpha_1)$ at 108° in the energy range E_p = 3.00 to 4.00 MeV.

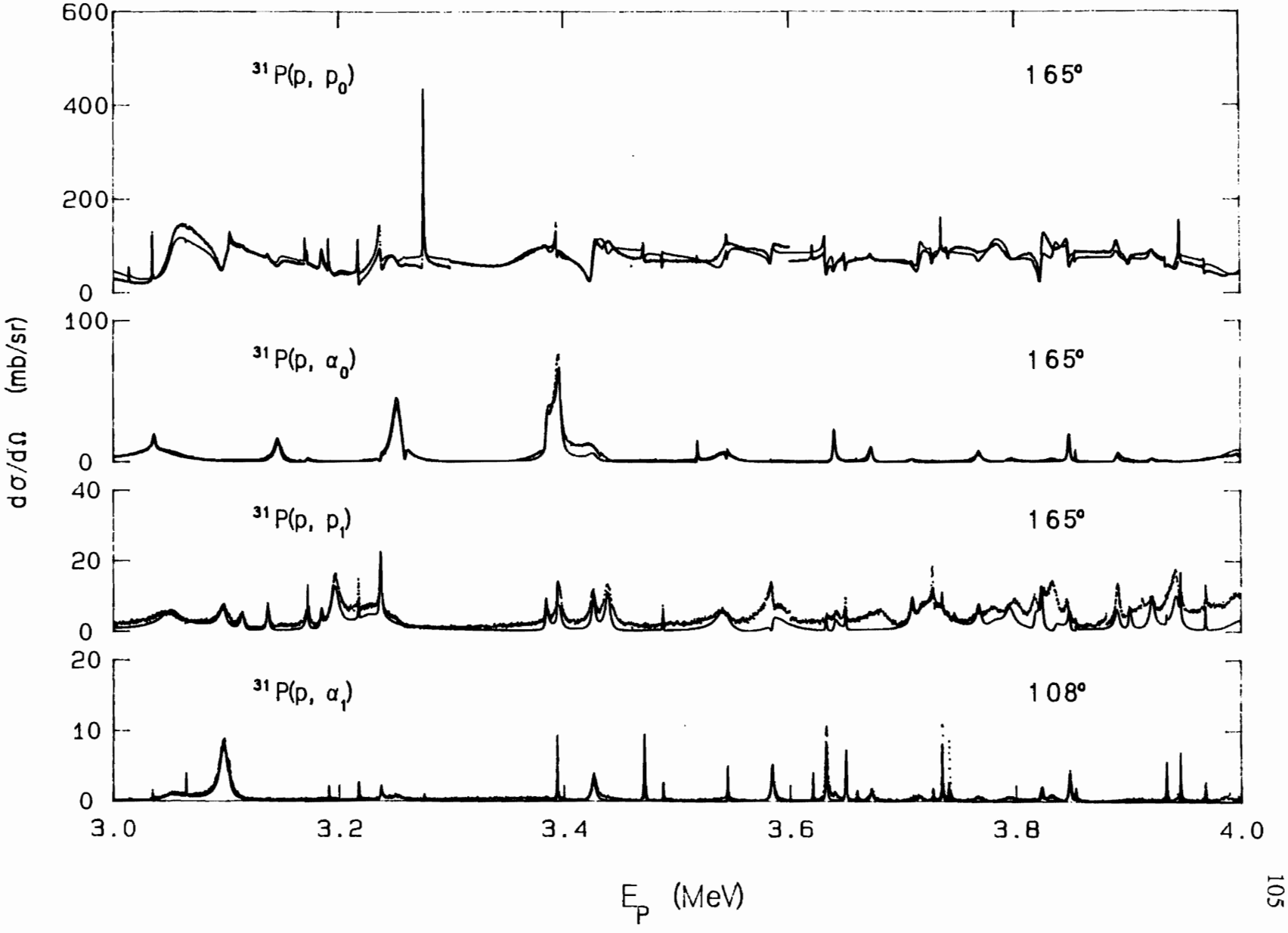
600
400
200
0
^{31}P(p, p$_0$)
165°
100
0
^{31}P(p, α$_0$)
165°
40
20
0
^{31}P(p, p$_1$)
165°
20
10
0
^{31}P(p, α$_1$)
108°
3.0
3.2
3.4
3.6
3.8
4.0
dσ/dΩ (mb/sr)
E$_P$ (MeV)

Figure 4.19 Differential cross sections for $^{31}P(p, p_0)$ at five angles in the energy range E_p = 2.00 to 3.00 MeV.

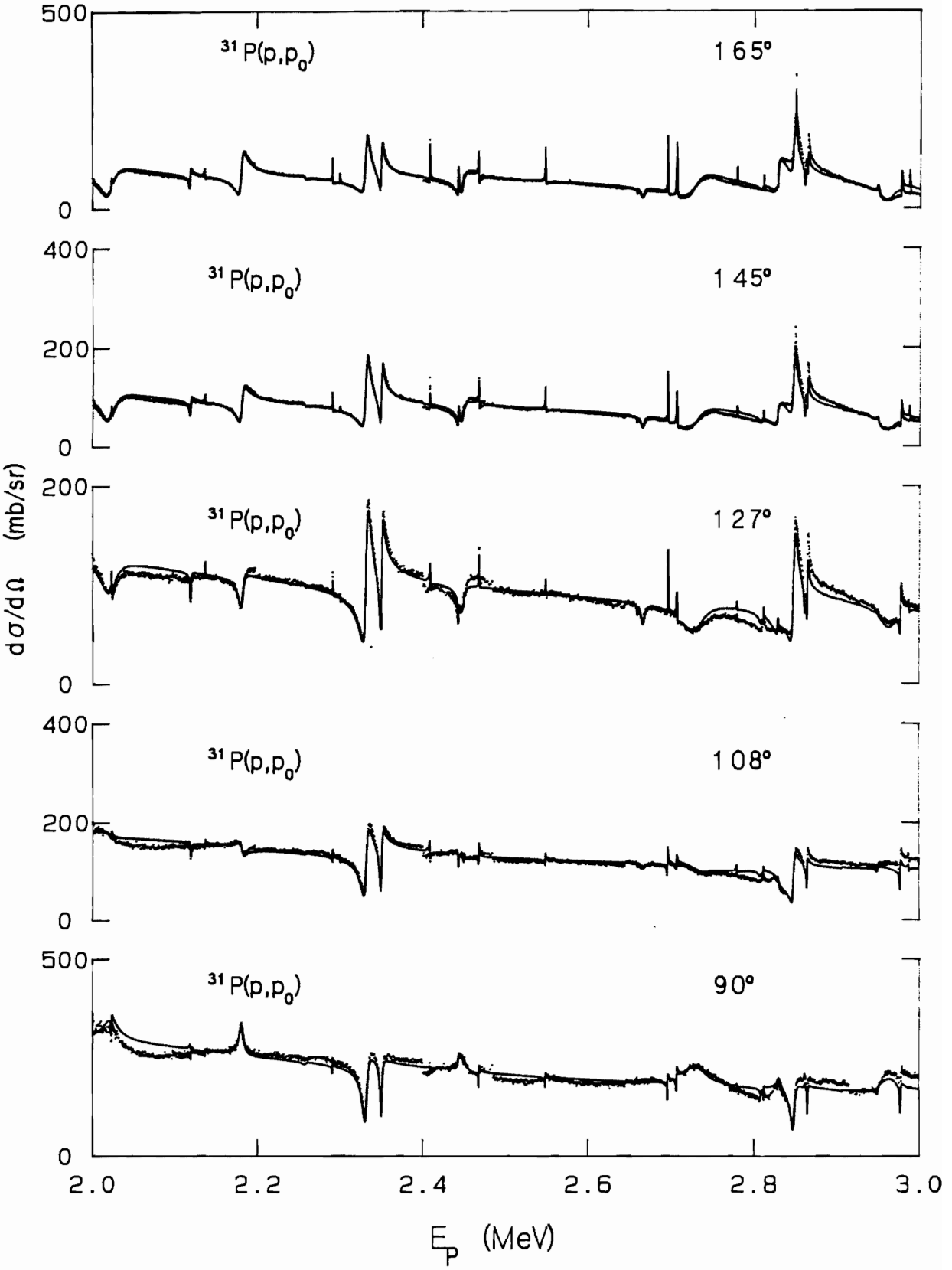
500
^{31}P(p,p$_0$)
165°
0
400
^{31}P(p,p$_0$)
145°
200
0
200
^{31}P(p,p$_0$)
127°
0
400
^{31}P(p,p$_0$)
108°
200
0
500
^{31}P(p,p$_0$)
90°
0
dσ/dΩ (mb/sr)
2.0
2.2
2.4
2.6
2.8
3.0
E$_P$ (MeV)

not seen.

Five resonances are newly observed and fit in the region E_p = 1.900 to 2.050 MeV. There had been some uncertainty in the J^π value for the resonance at E_p = 1.989 MeV in the previous data; the present experiment gives strong evidence for a 1^- assignment.

No previous resonance parameters are available above E_p = 2.050 MeV for comparison. There are always some ambiguities in the width determination and sometimes in the J^π value assignment when the level density is so high that resonances overlap. The complexity of the excitation curve is higher around E_p = 2.850 MeV than in any other energy region. The resonances near E_p = 3.033 MeV have very unusual interference effects in the α decay channel, and even after many attempts the fits are still not good. At higher energies the fits for the inelastic channel in general is poor. This may be because the level density is high and four channels are open, there is also complicated interference between levels, as discussed in the last section. In the fitting procedure, in order to avoid introducing spurious resonances, a level is assigned in the overlapping region only if there is a clear evidence for its existence. The extracted resonance parameters are listed in Table 4.2.

Table 4.3 lists relative signs of the resonance amplitudes for those resonances which have strong interference effects. Most of the two level interference cases are fit fairly well. For interference which involves three or more levels, the relative signs of the amplitudes are approximately correct, but many uncertainties remain.

There has been great interest in searching for lowlying T = 2 states. Previous experiments observed the lowest T = 2, $J^\pi = 0^+$ state in ^{32}S at $E_x(^{32}S)$ = 12.050 MeV (E_p = 3.289 MeV) with total width ≤ 170 eV by the (p,t) reaction (Freedman *et al.*, 1979) and by a detailed (p, γ) measurement (Vernotte *et al.*, 1973). This T = 2 state, whose excitation energy is expected to be only about 5 keV higher than a sharp, prominent 4^- resonance at E_p = 3.276 MeV, was not observed in proton elastic scattering in the present experiment. A NaI γ- ray detector was then used to observe the γ decay of this state. Unfortunately, the T = 2 resonance γ decay is very weak (the selection rule requires ΔT = 1, and the level density of T = 1 states is not high) and the resolution of the NaI crystal is poor. Essentially all of the γ-rays detected are from the (p, $p'\gamma$) channel; this

FANG PhD 1987

$R_0 = 1.25$ fm

Table 4.2

Resonance Parameters of ^{31}P(p, x)

		(p, p_0)				(p, p_1)				(p, α_0)				(p, α_1)			
E_p (MeV)	J^π	l	s	Γ (keV)	γ^2 (keV)	l	s	Γ (keV)	γ^2 (keV)	l	s	Γ (keV)	γ^2 (keV)	l	s	Γ (keV)	γ^2 (keV)
1.0170	1^-	1	0	0.015	6.84					1	0	0.025	6.72				
		1	1	0.06	25.64												
1.0600 [a]	2^+	2	0	0.01	30.73												
1.0896 [a]	2^+	2	1	0.01	25.00												
1.1192	1^-	1	0	0.13	28.57												
		1	1	0.02	4.40												
1.1576	0^+	0	0	0.025	1.32					0	0	0.075	7.30				
1.2500	2^-	1	1	1.5	160.05												
1.4002 [a]	3^+	2	1	0.01	4.30												
1.4030 [b]	3^-	3	0	0.008	58.50					3	0	0.04	16.94				
		3	1	0.008	58.50												
1.4060	1^-	1	0	0.12	6.25												
	1^-	1	1	0.06	3.13												
1.4114	1^+	0	1	0.025	0.42												

Table 4.2 continued

E_p (MeV)	J^π	(p, p_0) l	s	Γ (keV)	γ^2 (keV)	(p, p_1) l	s	Γ (keV)	γ^2 (keV)	(p, α_0) l	s	Γ (keV)	γ^2 (keV)	(p, α_1) l	s	Γ (keV)	γ^2 (keV)
1.4387	4^-	3	1	0.035	212.68												
1.4698	3^-	3	1	0.005	25.99					3	0	0.15	52.14				
1.4729	2^-	1	1	0.12	4.79												
		3	1	0.005	25.59												
1.4754 [b]	2^+	2	0	0.008	2.45					2	0	0.06	6.28				
		2	1	0.005	1.53												
1.5163	1^-	1	0	0.3	10.14					2	0	3.80	155.88				
		1	1	2.0	67.62												
1.5574	2^+	2	1	0.025	5.43												
1.5839	4^-	3	1	0.012	36.49												
1.5875	0^-	1	1	7.0	183.92												
1.6433	0^+	0	0	0.50	3.90					0	0	1.20	22.36				
1.6988 [a]	$(1^+, 2^+)$	2	1	0.01	1.27												
1.7173	1^- (2^+)	1	0	0.025	0.43					1	0	0.04	0.89				
		1	1	0.01	0.17												
1.7646 [a]	1^-	1	0	0.015	0.23												

Table 4.2 continued

E_p (MeV)	J^π	(p, p_0) l	s	Γ (keV)	γ^2 (keV)	(p, p_1) l	s	Γ (keV)	γ^2 (keV)	(p, α_0) l	s	Γ (keV)	γ^2 (keV)	(p, α_1) l	s	Γ (keV)	γ^2 (keV)
1.7959 [c]	1^-	1	0	0.11	1.53												
		1	1	0.04	0.56												
1.8184	3^-	3	0	0.003	3.53					3	0	0.650	70.02				
		3	1	0.01	11.75												
1.8892	2^+	2	0	0.11	7.54												
		2	1	0.07	4.80												
1.8938 [b]	1^-	1	0	11.5	123.27					1	0	3.50	47.62				
		1	0	6.0	64.32												
1.9528 [b]	2^+	2	0	0.03	1.71												
		2	1	0.02	1.14												
1.9669	2^-	1	1	5.05	45.31												
1.9756	2^+	2	0	0.055	2.94					2	0	0.52	1.19				
		2	1	0.04	2.14												
1.9810	1^+	0	1	0.70	2.44												
		2	1	0.05	2.63												
1.9826	0^+	0	0	0.55	1.91					0	0	0.05	0.38				
1.9890	2^+	2	0	0.025	1.29					2	0	0.085	1.87				
		2	1	0.055	2.83												

Table 4.2 continued

E_p (MeV)	J^π	(p, p_0) l	s	Γ (keV)	γ^2 (keV)	(p, p_1) l	s	Γ (keV)	γ^2 (keV)	(p, α_0) l	s	Γ (keV)	γ^2 (keV)	(p, α_1) l	s	Γ (keV)	γ^2 (keV)
2.0220	1^-	1	0	8.50	67.26					1	0	2.50	24.58				
		1	1	10.5	83.09												
2.0233	2^+	2	0	0.15	7.02					2	0	0.15	3.02				
		2	1	0.015	0.70												
2.1183	1^-	1	0	0.85	5.47					1	0	0.55	4.30				
		1	1	0.20	1.29												
2.1362 [b]	2^+	2	0	0.028	0.98												
		2	1	0.020	0.70												
2.1808	2^-	1	1	6.60	37.52												
		3	1	0.10	36.25												
2.2575	2^+	2	0	0.020	0.52					2	0	4.00	45.34				
		2	1	0.150	3.93												
2.2913 [b]	2^+	2	0	0.07	1.70												
		2	1	0.015	0.36												
2.3004 [b]	3^-	3	0	0.01	2.61	1	2	0.04	20.28								
		3	1	0.02	5.21												
2.3316	1^+	0	1	6.40	12.43												

Table 4.2 continued

E_p (MeV)	J^π	(p, p_0) l	s	Γ (keV)	γ^2 (keV)	(p, p_1) l	s	Γ (keV)	γ^2 (keV)	(p, α_0) l	s	Γ (keV)	γ^2 (keV)	(p, α_1) l	s	Γ (keV)	γ^2 (keV)
2.3504	1^+	0	1	2.38	4.50	0	1	0.10	10.37								
		2	1	0.13	2.77												
2.4084	3^-	3	1	0.08	15.79												
2.4370	1^-	1	0	0.03	0.11					1	0	0.15	0.60				
		1	1	0.006	0.02												
2.4428	2^-	1	1	0.65	2.34	1	1	0.06	11.96								
		3	1	0.06	10.88												
2.4474	1^-	1	0	1.5	5.36	1	1	0.20	38.81	2	0	0.80	3.12				
		1	1	5.4	19.29												
2.4498 [b]	2^+	2	0	0.03	0.52												
		2	1	0.02	0.35												
2.4678	2^+	2	0	0.04	0.67	0	2	0.01	0.52								
		2	1	0.16	2.86												
2.5486 [b]	2^+	2	0	0.12	1.72	0	2	0.01	0.35								
		2	1	0.02	0.29												
2.6590	2^-	1	1	0.05	0.13	1	1	0.30	19.76								

Table 4.2 continued

E_p (MeV)	J^π	(p, p_0) l	s	Γ (keV)	γ^2 (keV)	(p, p_1) l	s	Γ (keV)	γ^2 (keV)	(p, α_0) l	s	Γ (keV)	γ^2 (keV)	(p, α_1) l	s	Γ (keV)	γ^2 (keV)
2.6658	1^-	1	0	1.50	3.91	1	1	2.0	127.78	1	0	0.40	1.05				
		1	1	0.90	2.34	1	2	0.5	31.94								
2.6957	3^+	2	1	0.21	2.32	2	2	0.02	9.10								
2.7067	2^+	2	1	0.45	4.87					2	0	0.045	0.20				
2.7290	2^- (1^-)	1	1	30.0	72.22	1	1	2.0	97.66								
						1	2	0.5	31.95								
2.7795 [b]	3^-	3	0	0.005	0.43												
		3	1	0.04	3.42												
2.8080	0^+	0	0	0.90	1.01					0	0	2.20	3.45				
2.8110	1^-	1	1	0.12	0.26					1	0	1.50	3.11				
2.8117	2^+	2	1	0.10	0.91	0	2	0.06	0.72								
2.8289	2^+	2	0	0.08	0.71	0	2	0.50	5.67	2	0	0.03	0.11				
		2	1	0.20	1.77												
2.8297	$(1^-, 2^-)$	1	0	1.0	2.13												
		1	1	6.0	12.76												
2.8317	0^+	0	0	0.01	0.01					0	0	0.30	0.46				

Table 4.2 continued

E_p (MeV)	J^π	(p, p_0) l	s	Γ (keV)	γ^2 (keV)	(p, p_1) l	s	Γ (keV)	γ^2 (keV)	(p, α_0) l	s	Γ (keV)	γ^2 (keV)	(p, α_1) l	s	Γ (keV)	γ^2 (keV)
2.8340 [d]	1^-	1	0	14.0	29.63					1	0	1.3	2.60				
		1	1	3.50	7.41												
2.8484	1^+	0	1	5.30	5.75												
		2	1	0.20	1.72												
2.8504 [b]	3^-	3	0	0.045	3.34												
		3	1	0.01	0.74												
2.8545 [d]	1^-	1	0	1.50	3.10					1	0	25.0	48.44				
		1	1	0.30	0.62												
2.8618	1^-	1	0	0.50	1.02	1	1	0.80	23.57								
		1	1	0.60	1.23												
2.8651	1^+	0	1	0.55	0.59	0	1	0.10	1.26								
		2	1	0.15	1.25												
2.9064	2^+	2	0	0.07	0.55					2	0	2.50	7.92				
		2	1	0.05	0.39												
2.9497	2^+	2	0	0.55	4.05					2	0	2.20	6.50				
2.9640	1^-	1	0	8.00	14.65	1	2	2.50	52.32	1	0	1.50	2.47				
		1	1	12.0	21.98												

Table 4.2 continued

E_p (MeV)	J^π	(p, p_0) l	s	Γ (keV)	γ^2 (keV)	(p, p_1) l	s	Γ (keV)	γ^2 (keV)	(p, α_0) l	s	Γ (keV)	γ^2 (keV)	(p, α_1) l	s	Γ (keV)	γ^2 (keV)
2.9776	1^+	0	1	0.65	0.63	0	1	0.10	0.72								
		2	1	0.15	1.06												
2.9877 [b]	3^-	3	0	0.04	1.72	1	2	0.07	1.36								
		3	1	0.03	4.00												
3.0135	3^-	3	1	0.03	1.64												
3.0341	3^+	2	1	0.12	0.78									2	2	0.002	0.54
3.0356 [d]	3^-	3	0	0.005	0.26					3	1	2.00	12.23				
		3	1	0.015	0.79												
3.0380 [d]	1^-	1	0	24.0	40.65	1	2	2.00	33.39	1	0	4.00	5.94				
		1	1	7.0	11.86												
3.0500 [d]	2^-	1	1	18.0	30.12	1	1	0.40	6.45					1	2	0.18	19.94
						1	2	0.80	12.90								
3.0636	2^+	1	0	0.02	0.12									1	2	0.12	8.97
3.0975	2^-	1	1	5.80	9.26	1	1	0.20	2.82					1	2	0.80	80.35
		1	3	0.60	14.10	1	2	0.80	11.27								
3.1015	0^+	0	0	0.90	0.79	2	2	0.05	4.61					2	2	0.10	22.71

Table 4.2 continued

E_p (MeV)	J^π	(p, p_0)				(p, p_1)				(p, α_0)				(p, α_1)			
		l	s	Γ (keV)	γ^2 (keV)	l	s	Γ (keV)	γ^2 (keV)	l	s	Γ (keV)	γ^2 (keV)	l	s	Γ (keV)	γ^2 (keV)
3.1132 [b,d]	3^-	3	0	0.05	2.29												
		3	1	0.05	2.29	1	2	3.50	47.22								
3.1357 [d]	3^-	3	1	0.10	4.40	1	2	2.00	25.40	3	0	0.25	1.29				
3.1452	1^-	1	0	1.10	1.68					1	0	5.00	6.44				
		1	1	0.20	0.30												
3.1651	0^+	0	0	0.04	0.03					0	0	0.06	0.06				
3.1694	3^- (2^-)	3	1	0.015	0.63												
3.1713	3^-	3	0	0.045	1.86					3	0	0.80	3.88				
		3	1	0.10	4.14	1	2	0.50	5.78								
3.1717	$2^+(1^+)$	2	1	0.07	0.39	0	2	0.04	0.18								
3.1839	1^+	0	1	1.45	1.20	0	1	0.15	0.65								
		2	1	0.90	4.80												
3.1906	3^-	3	0	0.01	0.40									1	2	0.01	0.66
		3	1	0.06	2.41												
3.1963 [d]	2^-	1	1	1.30	1.89	1	1	4.00	43.40								
		3	1	0.30	11.91	1	2	3.00	32.55								

Table 4.2 continued

E_p (MeV)	J^π	(p, p_0) l	s	Γ (keV)	γ^2 (keV)	(p, p_1) l	s	Γ (keV)	γ^2 (keV)	(p, α_0) l	s	Γ (keV)	γ^2 (keV)	(p, α_1) l	s	Γ (keV)	γ^2 (keV)
3.2174	$3^+(2^+)$	2	0	0.35	1.53	2	2	0.04	2.58					0	2	0.02	2.94
3.2280 [d]	1^-	1	0	13.0	18.36	1	1	3.00	30.08								
		1	1	15.0	21.19	1	2	1.00	10.03								
3.2376	2^+	2	0	1.10	5.48	0	2	0.65	2.51	2	0	0.02	0.038	0	2	0.10	3.27
		2	1	0.10	0.50												
3.2515	2^+	2	0	1.65	8.07					2	0	6.80	12.77	0	2	0.50	17.77
		2	1	0.05	0.24												
3.2597	2^+	2	0	0.02	0.10					2	0	2.50	4.64				
		2	1	0.08	0.39												
3.2762	4^-	3	1	0.37	12.89									3	2	0.025	8.87
3.3650 [d]	1^-	1	0	40.0	50.22												
		1	1	10.0	12.56												
3.3845	3^-	3	0	0.10	2.94	1	2	1.80	12.63	3	0	1.20	4.14				
		3	1	0.05	1.47												
3.3890 [d,e]	2^+	2	0	0.80	3.32					2	0	12.0	18.74				
		2	1	0.20	0.83												
3.3911	3^+	2	1	0.20	0.82	0	3	0.05	0.14					2	2	0.08	5.84

Table 4.2 continued

E_p (MeV)	J^π	(p, p_0) l	s	Γ (keV)	γ^2 (keV)	(p, p_1) l	s	Γ (keV)	γ^2 (keV)	(p, α_0) l	s	Γ (keV)	γ^2 (keV)	(p, α_1) l	s	Γ (keV)	γ^2 (keV)
3.3963	3^-	3	0	0.42	12.13	1	2	1.50	10.27	3	0	2.30	7.81				
		3	1	0.08	2.31												
3.4260	1^+	0	1	1.80	1.28	0	1	1.00	2.70					2	2	0.50	35.71
		2	1	0.20	0.80												
3.4280	1^-	1	0	6.00	7.16					1	0	1.50	1.38				
		1	1	3.00	3.58												
3.4390 [d,e]	1^-	1	0	1.00	1.18	1	2	2.00	25.13	1	0	1.00	0.91				
		1	1	1.50	1.78												
3.4710	3^+	2	1	0.12	0.45									2	2	0.08	4.56
3.4875	1^-	1	1	0.18	0.20	1	2	0.10	0.57					1	2	0.06	1.50
3.5182 [d]	3^-	3	0	0.022	0.53					3	0	0.28	0.80				
		3	1	0.003	0.07												
3.5430	1^-	1	0	10.0	10.93	1	2	2.00	10.24	1	0	1.00	0.81				
		1	1	2.00	2.19												
3.5445	2^+	2	1	0.10	0.35					2	0	0.10	0.13	0	2	0.12	1.73
3.5841	1^-	1	0	1.50	1.59	1	2	0.80	3.80	2	0	0.10	0.13	1	2	0.40	7.56

Table 4.2 continued

E_p (MeV)	J^π	(p, p_0) l	s	Γ (keV)	γ^2 (keV)	(p, p_1) l	s	Γ (keV)	γ^2 (keV)	(p, α_0) l	s	Γ (keV)	γ^2 (keV)	(p, α_1) l	s	Γ (keV)	γ^2 (keV)
3.5880 [d]	$1^-(2^-)$	1	1	2.50	2.64	1	2	20.0	94.38								
3.6202 [b]	3^-	3	0	0.01	0.21									1	2	0.15	2.56
		3	1	0.02	0.42												
3.6319 [b]	2^+	2	0	0.10	0.80	0	2	0.10	0.20					0	2	0.25	2.84
		2	1	0.60	2.23												
3.6392 [b,d]	2^+	2	0	0.15	0.38					2	0	1.40	1.62				
		2	1	0.25	1.01												
3.6404	1^-	1	0	0.35	0.47	1	2	3.50	15.07	1	0	0.20	0.15	1	2	0.15	2.42
3.6494	$2^+(0^+)$	0	0	0.10	0.06					0	0	0.20	0.12	2	2	0.05	1.61
3.6720 [b]	3^-	3	0	0.12	2.33					3	0	1.80	4.14	1	2	0.80	11.84
		3	1	0.06	1.16												
3.6720	3^-	3	1	0.06	1.16												
3.6795	?	$\Gamma \approx 15.0$ keV															
3.7085 [b,d]	3^-	1	0	0.05	0.25	1	2	2.50	9.61	3	0	0.50	0.83				
		1	1	0.15	0.29												
3.7160	1^-	1	0	4.50	4.35	1	2	0.20	0.76					1	2	0.10	1.32

Table 4.2 continued

E_p (MeV)	J^π	(p, p_0) l	s	Γ (keV)	γ^2 (keV)	(p, p_1) l	s	Γ (keV)	γ^2 (keV)	(p, α_0) l	s	Γ (keV)	γ^2 (keV)	(p, α_1) l	s	Γ (keV)	γ^2 (keV)
3.7250 [d]	1^+	0	1	5.00	3.01	0	1	20.0	34.59								
		2	1	0.50	1.45												
3.7263	2^+	2	1	0.16	0.46	0	2	1.00	1.73	2	0	0.10	0.10	0	2	0.14	1.24
3.7348 [b]	3^-	3	0	0.085	1.52	1	2	0.05	0.18					1	2	0.15	1.88
		3	1	0.06	1.07												
3.7408 [e]	$1^-(2^+)$	1	0	0.10	0.10	1	1	0.10	0.36					1	2	0.20	2.65
3.7670	2^+	2	0	0.60	1.67	0	2	3.00	4.92	2	0	1.00	1.00				
3.7800 [d]	0^+	0	0	13.00	7.62	2	2	2.0	33.21								
3.7945	2^+	2	0	0.10	0.27	0	2	4.00	6.34	2	0	3.50	3.41				
		2	1	1.50	4.06												
3.8000	?	$\Gamma \approx 1.0$ keV															
3.8170 [b,d]	2^+	2	0	0.10	0.26	0	2	3.00	4.63								
		2	1	0.10	0.26												
3.8230	$2^-(1^-)$	1	1	2.20	1.98	1	1	0.30	0.96					1	2	0.10	1.00
						1	2	0.30	0.96								
3.8328	?	$\Gamma \approx 8.0$ keV															

Table 4.2 continued

E_p (MeV)	J^π	(p, p_0) l	s	Γ (keV)	γ^2 (keV)	(p, p_1) l	s	Γ (keV)	γ^2 (keV)	(p, α_0) l	s	Γ (keV)	γ^2 (keV)	(p, α_1) l	s	Γ (keV)	γ^2 (keV)
3.8350 [d]	0^+	0	0	4.00	2.28	2	2	0.50	7.46								
3.8473	2^+	2	0	0.50	0.52	0	2	0.40	0.59	2	0	0.60	3.00	0	2	0.30	1.99
		2	1	0.20	0.31												
3.8529	2^+	2	0	0.02	0.05	0	2	0.10	0.15	2	0	0.15	0.14	0	2	0.08	0.52
		2	1	0.05	0.13												
3.8895 [d]	3^-	3	0	0.12	1.76	1	2	3.00	8.70	3	0	1.30	2.27				
		3	1	0.30	4.39												
3.9006 [d]	1^-	1	0	0.08	0.07	1	2	2.20	6.33	1	0	0.05	0.03				
		1	1	0.42	0.36												
3.9204 [d]	3^-	3	0	0.15	0.56	1	2	4.00	11.20	3	0	1.00	1.68				
		3	1	0.45	2.11												
3.9329 [b]	2^+	2	0	0.05	0.12	0	2	0.05	0.07					0	2	0.12	0.65
		2	1	0.05	0.12												
3.9420 [d]	1^-	1	0	4.00	3.36	1	2	3.50	9.52								
3.9454	3^-	3	0	0.10	1.37	1	2	0.05	0.14					1	2	0.10	0.75
		3	1	0.05	0.68												

Table 4.2 continued

E_p (MeV)	J^π	(p, p_0) l	s	Γ (keV)	γ^2 (keV)	(p, p_1) l	s	Γ (keV)	γ^2 (keV)	(p, α_0) l	s	Γ (keV)	γ^2 (keV)	(p, α_1) l	s	Γ (keV)	γ^2 (keV)
3.9678 [b]	2^+	2	0	0.05	0.12	0	2	0.30	0.39					0	2	0.10	0.54
		2	1	0.05	0.12												
4.0000 [f]	1^-	1	0	10.0	8.12	1	1	6.0	15.11	1	0	6.00	3.22				
		1	1	8.00	6.49												

a) J^π values are adopted from (p, γ) measurement

b) Channel spin mixing ratios have large errors

c) J^π values are different from previous assignment (Endt and Van der Leun, 1978)

d) Values for the resonance widths (especially $\Gamma_{p'}$) have large uncertainties

e) J^π cannot be uniquely determined

f) Estimated resonance width and position

Table 4.3 Relative Signs of the Resonance Amplitudes [a]

E_p (MeV)	J^π	(p, p_0) l	s	Γ (keV)	(p, p_1) l	s	Γ (keV)	(p, α_0) l	s	Γ (keV)	(p, α_1) l	s	Γ (keV)
1.8938	1^-	1	0	−11.5				1	0	3.50			
		1	1	6.00									
2.0220	1^-	1	0	8.50				1	0	2.50			
		1	1	−10.5									
2.0233	2^+	2	0	0.15				2	0	0.15			
		2	1	0.015									
*													
2.4370	1^-	1	0	0.03				1	0	0.15			
		1	1	−0.006									
2.4428	2^-	1	1	0.65	1	1	0.06						
		3	1	−0.06									
2.4474	1^-	1	0	1.50	1	1	0.20	1	0	0.80			
		1	1	5.40									
*													
2.8080	0^+	0	0	0.90				0	0	2.20			
2.8110	1^-	1	0	−0.12				1	0	1.50			
*													
2.8289	2^+	2	0	0.08	0	2	0.50	2	0	0.03			
		2	1	−0.20									
2.8317	0^+	0	0	0.01				0	0	0.30			
2.8340	1^-	1	0	14.0				1	0	1.30			
		1	1	−3.50									
2.8545	1^-	1	0	1.50				1	0	−25.0			
		1	1	0.30									
*													
2.8618	1^-	1	0	0.50	1	0	0.80						
		1	1	−0.60									

Table 4.3 Continued

E_p (MeV)	J^π	(p, p_0)			(p, p_1)			(p, α_0)			(p, α_1)		
		l	s	Γ (keV)	l	s	Γ (keV)	l	s	Γ (keV)	l	s	Γ (keV)
2.8651	1^+	0	1	0.55	0	1	0.10						
		2	1	0.15									
*													
2.964	1^-	1	0	8.00	1	2	2.50	1	0	1.50			
		1	1	12.0									
3.0356	3^-	3	0	0.005				3	0	2.00			
		3	1	−0.015									
3.0380	1^-	1	0	−24.0	1	1	2.00	1	0	4.00			
		1	1	7.00									
*													
3.0975	2^-	1	1	5.80	1	1	−0.20				1	2	−0.80
		3	1	0.60									
3.1015	0^+	0	0	0.90	2	2	0.05				2	2	0.10
*													
3.1357	3^-	3	1	0.10	1	2	2.00	3	0	−0.25			
3.1452	1^-	1	0	1.10				1	0	5.00			
		1	1	0.20									
3.1713	3^-	3	0	0.045	1	2	2.50	3	0	−0.80			
		3	1	0.10									
*													
3.1963	2^-	1	1	1.30	1	1	−4.00						
		3	1	0.30	1	2	3.00						
3.2174	3^+	2	1	−0.35	2	2	0.04				2	1	0.02
3.2280	1^-	1	0	13.0	1	1	3.00						
		1	1	15.0	1	2	−1.00						
3.2376	2^+	2	0	−1.10	0	2	0.65	2	0	0.02	0	2	0.10
*													

Table 4.3 Continued

E_p (MeV)	J^π	(p, p_0) l	s	Γ (keV)	(p, p_1) l	s	Γ (keV)	(p, α_0) l	s	Γ (keV)	(p, α_1) l	s	Γ (keV)
3.3890	2^+	2	0	0.80				2	0	12.0			
		2	1	0.20									
3.3963	3^-	3	0	− 0.42	1	2	1.50	3	0	2.30			
		3	1	0.08									
3.4280	1^-	1	0	− 6.00				1	0	1.50			
		1	1	3.00									
*													
3.7085	3^-	3	0	− 0.05	1	2	2.50	3	0	0.50			
3.7160	1^-	1	1	4.50	1	2	0.20				1	2	0.10
3.7250	1^+	0	1	5.00	0	1	20.0						
3.7263	2^+	2	1	− 0.16	0	2	1.00	2	0	0.10	0	2	0.14
3.7348	3^-	3	0	0.085	1	2	− 0.05				1	2	0.15
		3	1	0.06									
*													
3.8170	2^+	2	0	0.10	0	2	3.00						
		2	1	0.10									
3.8230	2^-	1	1	2.20	1	1	− 0.30				1	2	0.10
					1	2	0.30						

a) The negative signs are associated with $|\Gamma|^{1/2}$. Above $E_p = 3.30$ MeV the sign assignments are approximately correct. The relative signs are important for the groups (2 – 5 resonances) separated by an asterisk.

causes a high background which may mask the presence of the $T = 2$ state. Evidence for the existence of this $T = 2$ state was not obtained in the present experiment.

Chapter V

Analysis and Results

A. Analog States

If the nuclear force is charge independent, then the neutron and proton may be considered as two states of the same particle – the nucleon. States with the same value of the isospin quantum number T, but with different projections T_3 = (N-Z)/2 should have similar properties. Since the $2T$+1 members of the isospin multiplet occur in different nuclei, considerable attention has focused on the properties of these multiplets. Clearly the electromagnetic force violates charge independence and isospin is no longer a good quantum number, only an approximate one. Thus the identification of isospin multiplets in nuclei provides evidence about the charge independence of the nuclear force.

For mass A > 18, the ground state of a nucleus is always the last member of a T-multiplet with T = T_3 (McCarthy, 1968). The T_3 = T−1 member of this multiplet is always a rather highly excited state of a nucleus with one less neutron. This is because the Coulomb force causes the proton-rich nuclei to have higher energies than the neutron-rich nuclei. Members of the multiplet states with the highest T_3 value are referred to as "parent" states, and the others are called "daughter" states. Figure 5.1 shows the energy relationship of these multiplets in the isobar (the same mass number); that is,

$$E_x(A) = E_x(P) + \Delta E_C - \delta = E_x(P) + \Delta E_C - B_n + B_p \ ,$$

where B_n is the binding energy of the last neutron in the parent nucleus, B_p is the binding energy of the last proton in the daughter nucleus, and $E_x(A)$ and $E_x(P)$ are the excitation energies of the daughter and parent state, respectively. From figure 5.1, one can see a example of a basic symmetry property: maximum symmetry configurations have lower energies than those with less symmetry (the T = 0 state has the highest symmetry in isospin space). Even for the lowlying isobaric states in the parent nucleus ${}_Z A_{N+1}$, the excitation energies of the corresponding states in the

Figure 5.1 Schematic level diagram showing energy relations between the parent state and the analog resonance.

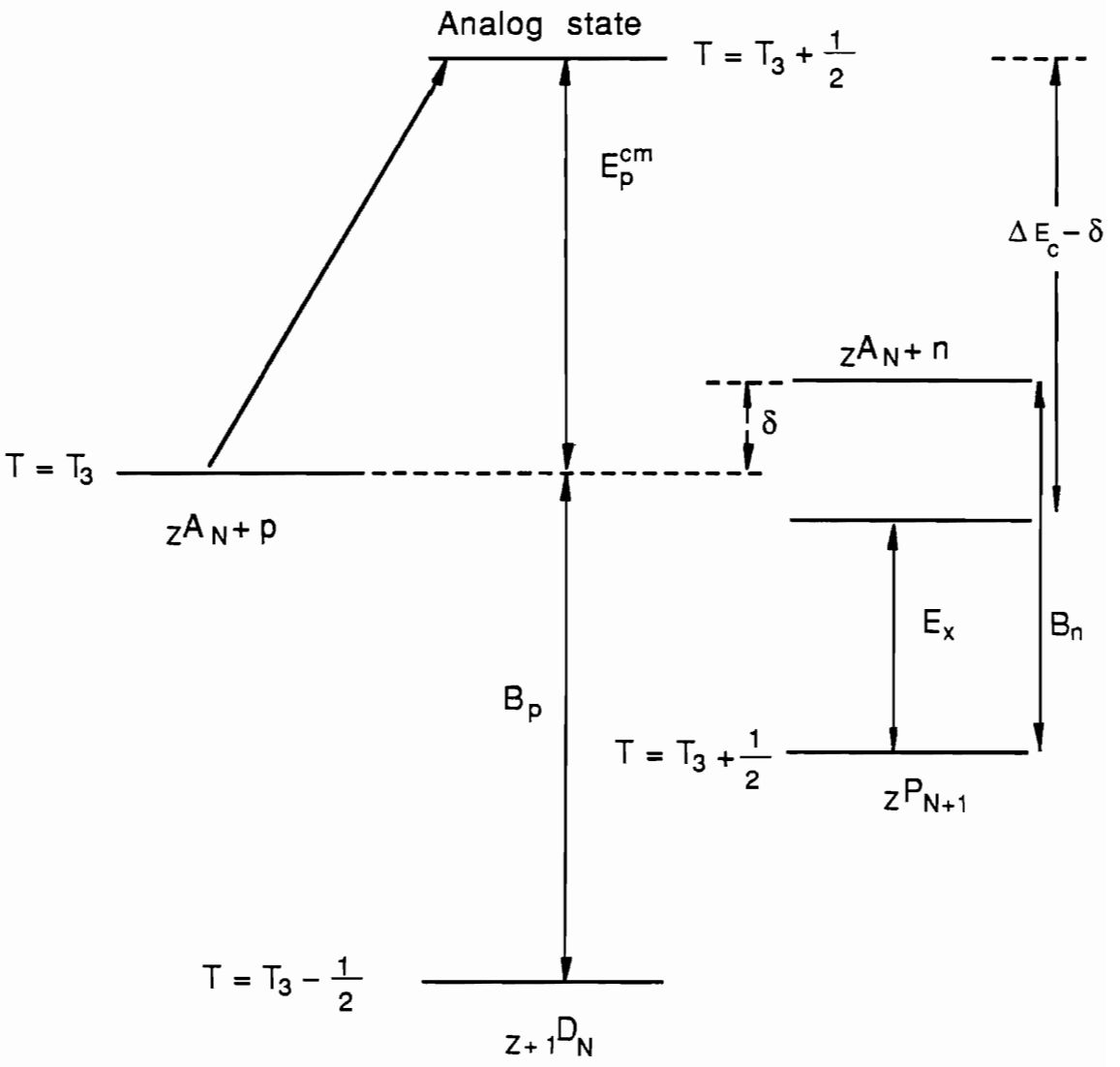
Analog state
$T = T_3 + \frac{1}{2}$
E_p^{cm}
$\Delta E_c - \delta$
$_ZA_N + n$
δ
$T = T_3$
$_ZA_N + p$
E_x
B_n
B_p
$T = T_3 + \frac{1}{2}$
$_ZP_{N+1}$
$T = T_3 - \frac{1}{2}$
$_{Z+1}D_N$

daughter nucleus $_{Z+1}A_N$ are usually so high that they occur at positive energies (the energy scale is defined such that the energy is equal to zero at the separation energy of the last proton), and these states are called analog states. These analog states can be reached by proton scattering from a $_ZA_N$ target. Proton scattering from a target nucleus with isospin T_t can form a compound nucleus with isospin $T = T_t+1/2$ or $T = T_t-1/2$; the analog resonances are the $T = T_t+1/2$ states. For nuclei with $(\Delta E_C - \delta - B_P) \sim 0$, low energy proton scattering provides an excellent method to study the lowlying (in the parent nucleus) isobaric states. Nuclei in the $2s$-$1d$ and $1f$-$2p$ shells have this property, and many of them have been investigated extensively with the TUNL high resolution accelerator facilities (Bilpuch *et al.* 1976).

The states of an isospin multiplet have the same spin and parity. To identify the analog state, one needs information about the parent state, such as the J^π value, excitation energy E_x and strength of the state. This information for lowlying states can be obtained by neutron transfer experiments, usually (d, p) reactions. The Coulomb energy shift ΔE_C can be estimated theoretically. The strengths of the isospin T states in parent and daughter nuclei are assumed to be the same:

$$s_{dp} = s_n \approx s_p = (2T+1)\frac{\Gamma_p}{\Gamma_{sp}} , \qquad (5.1)$$

where s_p is the proton spectroscopic factor, which can be used to characterize the strength of the analog state, Γ_p is the measured laboratory width of the analog state, $s_{dp} \equiv s_n$ is the neutron spectroscopic factor, and Γ_{sp} is the single particle width of the proton resonance.

The proton single particle widths for the analog resonances were calculated with the program HANS. This program provides three different methods of calculation; here the ZDH (Zaidi, Darmodjo, and Harney 1967, 1968) method is chosen for consistency with other analyses. This method was discussed in detail by Harney and Weidenmüller (1969) and by Moses (1969). In this method the neutron eigenstate in the parent nucleus is calculated first with a Woods-Saxon potential. To calculate the proton width, one assumes that the proton sees the same potential shape as the neutron, except that the depth of the potential well differs from the neutron by a symmetry term:

$$U_p = U_n - V_1(2T_0 + 1)/(2A),$$

where A is the target mass number, V_1 is fixed at 125 MeV, and the proton resonance energy position is determined by equation (5.1). The calculated proton single particle widths are sensitive to the choice of nuclear radius r_0. Bilpuch *et al.* (1976) discussed these effects in detail. In practice standard values for the optical model parameters are chosen.

For the parent nucleus ^{32}P, the lowest T = 1 state is its ground state with $J^\pi = 1^+$. With the Coulomb energy shift estimate (Janecke 1969) and the binding energy $B_p = 8.864$ MeV of the last proton for ^{32}S, the analog resonance is expected at $E_x(^{32}S) \sim 7.200$ MeV. This resonance was observed at $E_x(^{32}S) = 7.003$ MeV, and was studied in detail in several experiments (Kalifa *et al.*, 1978). Based on the well-studied T = 1 analog resonances in ^{32}S below the proton separation energy, the excitation energies of parent and daughter resonances have the relation

$$E_x(^{32}S) = E_x(^{32}P) + 7.000 \text{ MeV} . \qquad (5.2)$$

Using this relation as a guide and remembering that the parent and analog states have the same J^π, one can locate the analog resonance candidates by comparing the (*d, p*) experimental data with proton scattering data.

Previous experiments (Kalifa *et al.* 1978, Endt and Van der Leun, 1978) identified the T = 1 analog resonances below $E_x(^{32}S) = 10.977$ MeV and a 4^- resonance at 12.044 MeV, which correspond to proton scattering energies up to 2.181 MeV and 3.282 MeV, respectively. In this experiment both resonance positions and strengths agree very well with previous measurements. For resonances above $E_x(^{32}S) = 11.00$ MeV, only a few resonances are identified as analog states mainly because of the lack of (*d, p*) data corresponding to this energy region. The results are listed in Table 5.1.

The strength analysis suggests that the analog of the $E_x(^{32}P) = 3.320$ MeV, 3^- state is a resonance at $E_x(^{32}S) = 10.223$ MeV. Previous measurements suggest that this resonance may be mixed with a 3^-, T = 0 resonance at $E_x(^{32}S) = 10.286$ MeV.

The analog of the $E_x(^{32}P) = 3.880$ MeV, 2^+ state was found previously to be a doublet in proton scattering. Another narrow 2^+ resonance is found in the present experiment at $E_x(^{32}S) =$ 10.791 MeV, which is near the analog energy. The summed strength s_p agrees well with the

neutron strength s_n.

The analog of the $E_x(^{32}P) = 4.150$ MeV, 3^- state is a narrow resonance which has not observed previously, and is identified in the present experiment.

Above $E_x(^{32}P) = 4.200$ MeV, the (d, p) reaction does not provide the strength information. An early measurement by Holterbekk (1962) provided a few resonance strengths, but the experimental data was analyzed with the Butler-Born approximation instead of the now standard method – DWBA. These resonance strengths were not included in Endt and Van der Leun's (1978) compilation.

In the (d, p) measurements, there were some ambiguities in the J value assignments. This introduces an additional difficulty for the identification of the analog resonances. Fortunately, the relation (5.2) holds very well up to the $E_x(^{32}P) = 4.880$ MeV, 4^- state, whose analog is a sharp and prominent resonance at $E_x(^{32}S) = 12.037$ MeV. Thus, assuming the relation (5.2) is obeyed well by all the analog resonances, one can examine the J^π values of the resonances in the energy range in which the analog resonance is expected to occur. Together with the strength analysis, some of the ambiguities in the J values of the parent states might be removed.

The fluctuations in the Coulomb energy shifts in Table 5.1 can be qualitatively explained in terms of the "Thomas-Ehrman shift" (Lane and Thomas, 1958; Wilson *et al.* 1974). As discussed in chapter II, for an isospin resonance in the parent nucleus, the relation between the observed resonance energy E_{rN} and the energy eigenvalue $E_{\lambda N}$:

$$E_{\lambda N} - E_{rN} - \Delta_{\lambda N} = 0 ,$$

where $\Delta_{\lambda N} = \gamma_{\lambda N}{}^2 [S_N(E_{rN}) - B]$ is the energy shift, $\gamma_{\lambda N}{}^2$ is the neutron reduced width and B is the boundary condition defined by (2.21). The analog resonance observed in the daughter nucleus has the same relation. From the charge independence of the nuclear force, the reduced width γ^2 and the boundary condition B of the isospin resonance in two nuclei are expected to be the same. One can see this from the definitions (2.16) and (2.20); if the Coulomb force is negligible compared with the nuclear force, the interior wave functions are the same for the two nuclei. Thus, by subtracting the two relations, one obtains

$$E_{rP} - E_{rN} = (E_{\lambda P} - E_{\lambda N}) + [S_N(E_{rN}) - S_P(E_{rP})]\gamma_\lambda{}^2 . \qquad (5.3)$$

Table 5.1 T = 1 Analog Resonances

^{32}P			^{32}S						ΔE_x^{exp}	ΔE_x^{cal}
J^π	E_x (MeV)	$s_n(=s_{dp})$[a]	J^π	E_x (MeV)	E_p (MeV)	Γ_p (keV)	$\Gamma_{sp}/(2T+1)$ (keV)	s_p	(MeV)	(MeV)
2^-	3.260	0.44	2^-	10.075	1.250	1.50	3.53	0.42	6.815	6.884
3^-	3.320	0.44	3^-	10.223	1.403	0.016	0.037	0.43	6.913	6.946
4^-	3.443	0.78	4^-	10.257	1.438	0.035	0.048	0.73	6.814	6.922
			4^-	10.398	1.583	0.012	0.087	0.14	6.955	6.986
2^+	3.444	b	2^+	10.368	1.557	0.025	1.25	0.02	6.924	6.999
			2^+	10.791	1.989	0.08	5.18	0.015	6.911	6.999
2^+	3.880	0.056	2^+	10.823	2.022	0.17	5.57	0.030	6.943	6.997
			2^+	10.933	2.136	0.05	6.97	0.007	7.053	7.002
2^-	4.010	0.066 ($l=1$) 0.124 ($l=3$)	2^-	10.977	2.181	6.60 0.10	55.00 0.64	0.13 0.16	6.967	6.966
1^-	4.040	0.43	1^-	10.822	2.022[c]	19.0	42.00	0.45	6.782	6.864
3^-	4.150	0.026	3^-	11.092	2.300	0.03	1.03	0.029	6.942	6.998

a) Endt and Van der Leun (1978). b) Masked by the resonance at $E_x(^{32}P) = 3.443$MeV. c) See chapter V section C.

The second term on the right hand side is referred to as the Thomas-Ehrman shift. In proton scattering experiments, the shift function $S_P(E_{rP})$ is the real part of the logarithmic derivative of an unbound state wave function (2.4). The excitation energies of lowlying resonances in parent nuclei are usually lower than the last neutron separation energy; in these cases, $S_N(E_{rN})$ is the logarithmic derivative of a bound state wave function (Weidenmüller, 1965).

The first term on the right side of (5.3) contains the "real" Coulomb energy shift, electromagnetic spin-orbit effect, etc. This term is approximately a constant. If interest is focussed on relative shifts between the different pairs of analog resonances, the quantity $(E_{\lambda P} - E_{\lambda N})$ can be chosen as a fixed number, and the excitation energy differences of the analog resonances can be approximately predicted. In the present experiment, the Thomas-Ehrman shift for the first analog state (corresponding to the ground state of ^{32}P) is assumed to be zero. Therefore $(E_{\lambda P} - E_{\lambda N})$ is equal to 7.002 MeV, which is the excitation energy of the first analog resonance in ^{32}S. The shift functions are calculated with Coulomb wave functions and the bound neutron wave functions (Shiff, 1968), and the reduced widths γ_λ^2 are obtained with the relation $\gamma_\lambda^2 = \Gamma_{\lambda p}/2P$. The main uncertainty in the calculation is the choice of the radius. Again, standard values are used. Humblet and Lebon (1967) discussed in detail these effects and proposed another method which is independent of the nucleus radius to calculate the Thomas-Ehrman shift.

Calculated excitation energy differences are listed in Table 5.1. The agreement with experiment is fairly good. One can see that if two pairs of analog resonances are not far separated, and one of the pair is much stronger than the other, the position of the stronger resonance may be moved so much that the order of the resonances can be reversed. For example, the analog of $E_x(^{32}\text{P}) = 4.010$ MeV, 2^- state is identified at $E_x(^{32}\text{S}) = 10.977$ MeV ($\gamma^2 = 37.5$ keV), while the analog of $E_x(^{32}\text{P}) = 4.040$ MeV, 1^- state is identified at $E_x(^{32}\text{S}) = 10.822$ MeV ($\gamma^2 = 153.4$ keV).

B. Proton Strength

The resonance laboratory width $\Gamma = 2P\gamma^2$ contains the kinematic factor P, which as shown in figure 4.4, usually varies several orders of magnitude for the energy range of our experiments.

To better understand the nuclear structure, one needs to examine the reduced width γ^2. In figures 5.2 – 5.8 are plotted the reduced widths, cumulative reduced width and positions of the resonances versus the incident proton energy, for each l and J^π value. The reduced width $\gamma^2(E)$ plot gives the strength of the resonances and the strength distribution. The cumulative reduced width $\Sigma\gamma^2(E)$ shows the smoothness of the strength distribution; any large fluctuation in strength can easily be seen in this plot. As discussed in the last section, the analog resonances in the daughter nucleus are at high excitation energies, and usually they are fragmented (although not to a great extent) into the $T = 0$ background resonances. Thus the plot of $\Sigma\gamma^2(E)$ is very useful in the identification of an analog resonance.

Only one 0^- resonance was found in the present experiment; it is shown in figure 5.2a.

Figure 5.2b shows the strengths of ten 0^+ states. These states are evenly distributed in the present experimental energy range, except that there may be an analog resonance near $E_p = 3.050$ MeV. Shell model calculations (see section D of this chapter) predict a 0^+, $T = 1$ state at $E_p = 3.030$ MeV, but there are no (d, p) data available to help in the identification.

Figures 5.3a and 5.3b show the s-wave and d-wave strengths of ten 1^+states. The cumulative reduced width strongly suggests that there is an analog resonance near $E_p = 2.340$ MeV. A 1^+ state was found in the (d, p) reaction at $E_x(^{32}P) = 4.200$ MeV. The excitation energies in the two nuclei obey the relation (5.2) very well, but there is no reliable neutron strength information to confirm this state as an analog resonance.

Figures 5.4a and 5.4b show the strength of thirty-three 1^- resonances for channel spin $s = 0$ and $s = 1$, respectively. Many of these states have an α_0 decay. As discussed in chapter IV, the shape of a 1^- resonance in elastic scattering and the α_0 angular distribution are very sensitive to the channel spin mixing ratio. Thus the strengths of 1^- resonances for different channel spins are better determined than for the states with other J^π. The strengths are evenly distributed except near the analog resonance at $E_p = 2.100$ MeV. The level density is higher above $E_p = 3.000$ MeV than at lower energies.

For eleven 2^- resonances above $E_p = 1.400$ MeV, the states are evenly distributed both in position and strength, as shown in figures 5.5a and 5.5b for $l = 1$ and $l = 3$. The l-mixing is

Figure 5.2 (a) Proton reduced widths versus energy for 0^- resonances in ^{32}S. (b) Reduced widths for 0^+ resonances. In general these resonances are not strong.

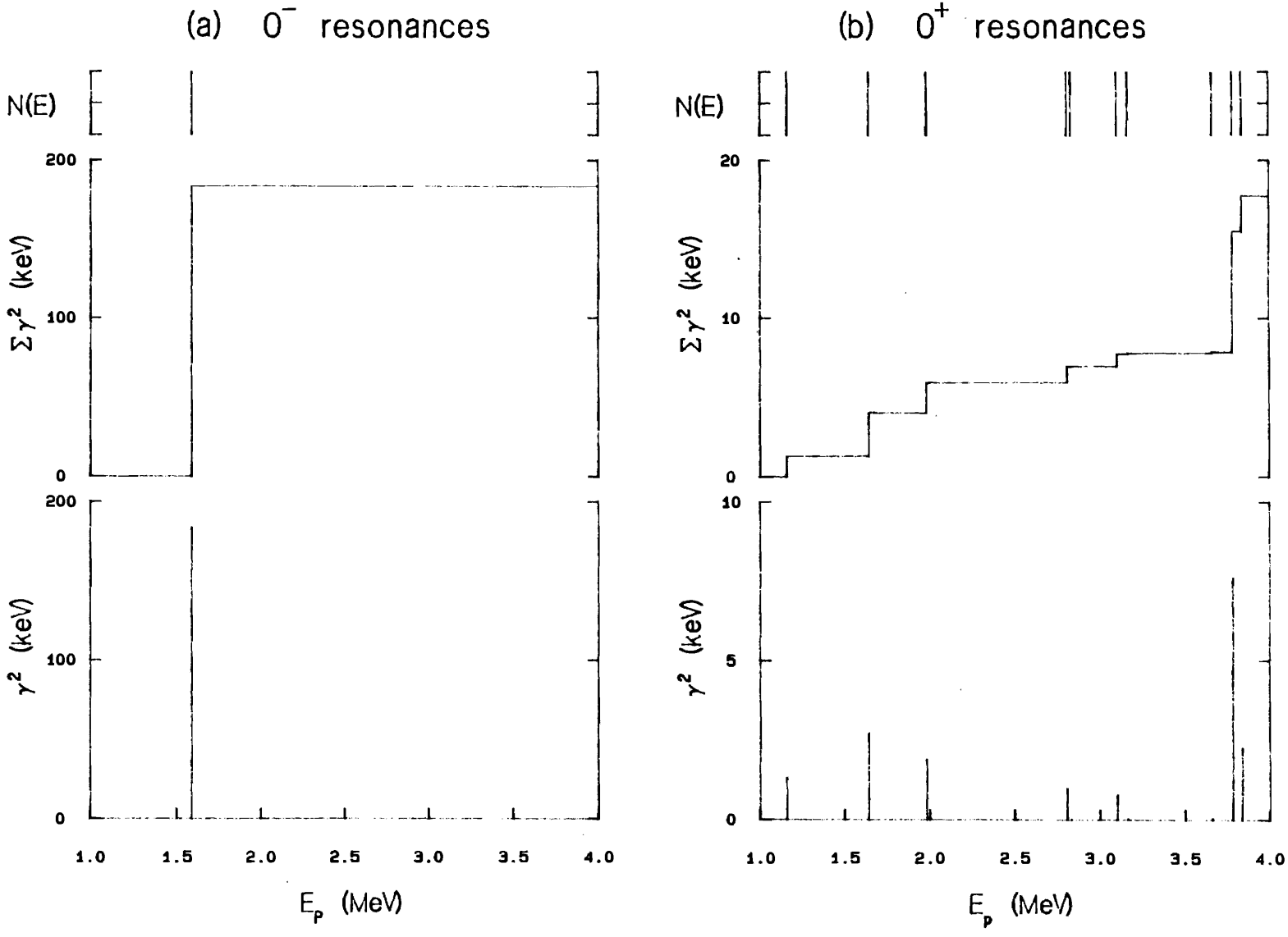
(a) 0^- resonances
(b) 0^+ resonances
N(E)
$\Sigma\gamma^2$ (keV)
γ^2 (keV)
200
100
0
20
10
5
1.0
1.5
2.0
2.5
3.0
3.5
4.0
E_p (MeV)

Figure 5.3 (a) Proton reduced widths versus energy for 1^+, $\ell = 0$ resonances in ^{32}S. Near 2.35 MeV there is strong evidence for an analog resonance. (b) Reduced widths for 1^+, $\ell = 2$ resonances.

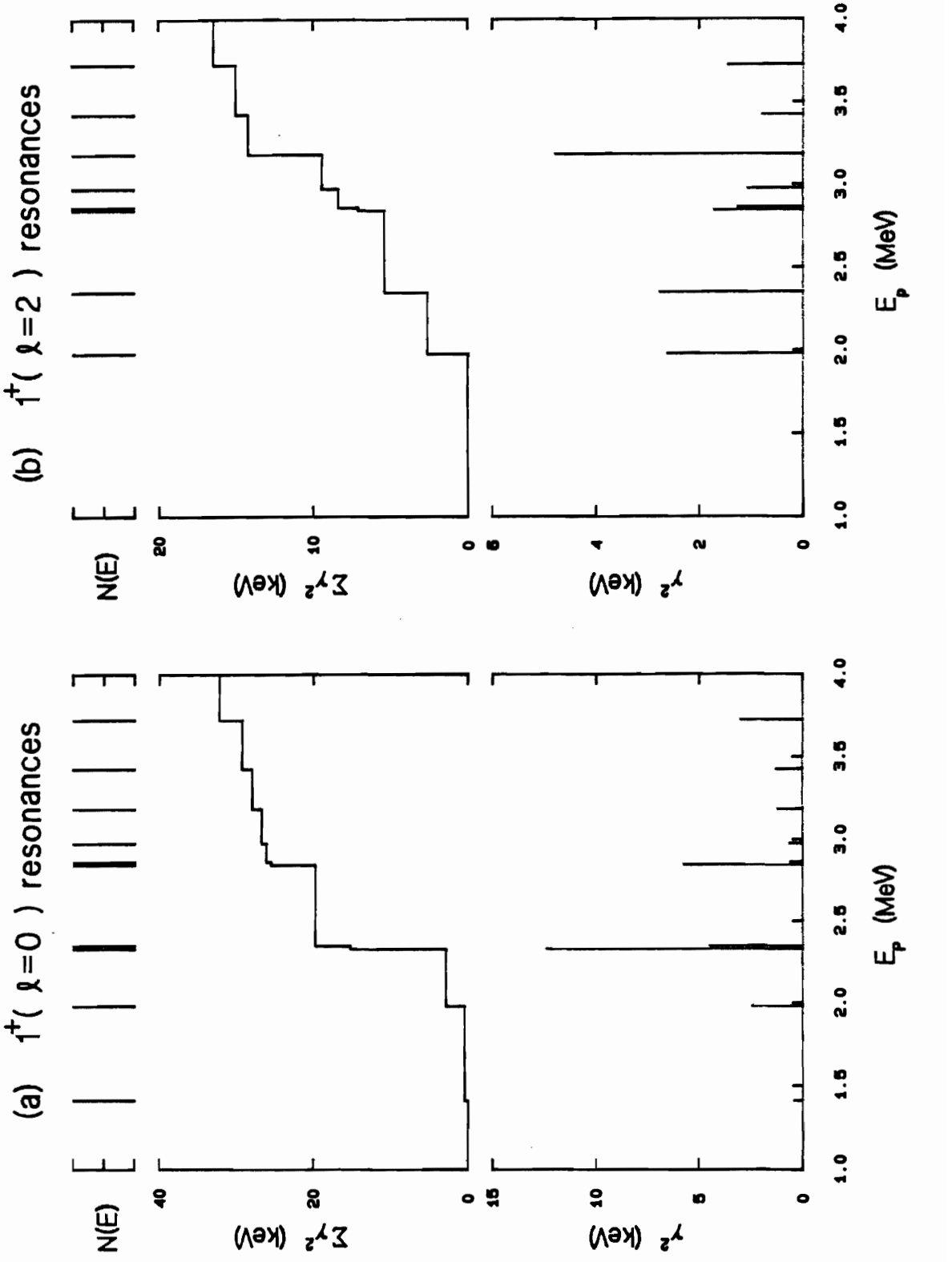
(a) 1+(ℓ=0) resonances
(b) 1+(ℓ=2) resonances
N(E)
Σγ² (keV)
γ² (keV)
Ep (MeV)

Figure 5.4 (a) Proton reduced widths versus energy for 1^-, $s = 0$ resonances in ^{32}S. There is an analog resonance near 1.98 MeV. (b) Reduced widths for 1^-, $s = 1$ resonances.

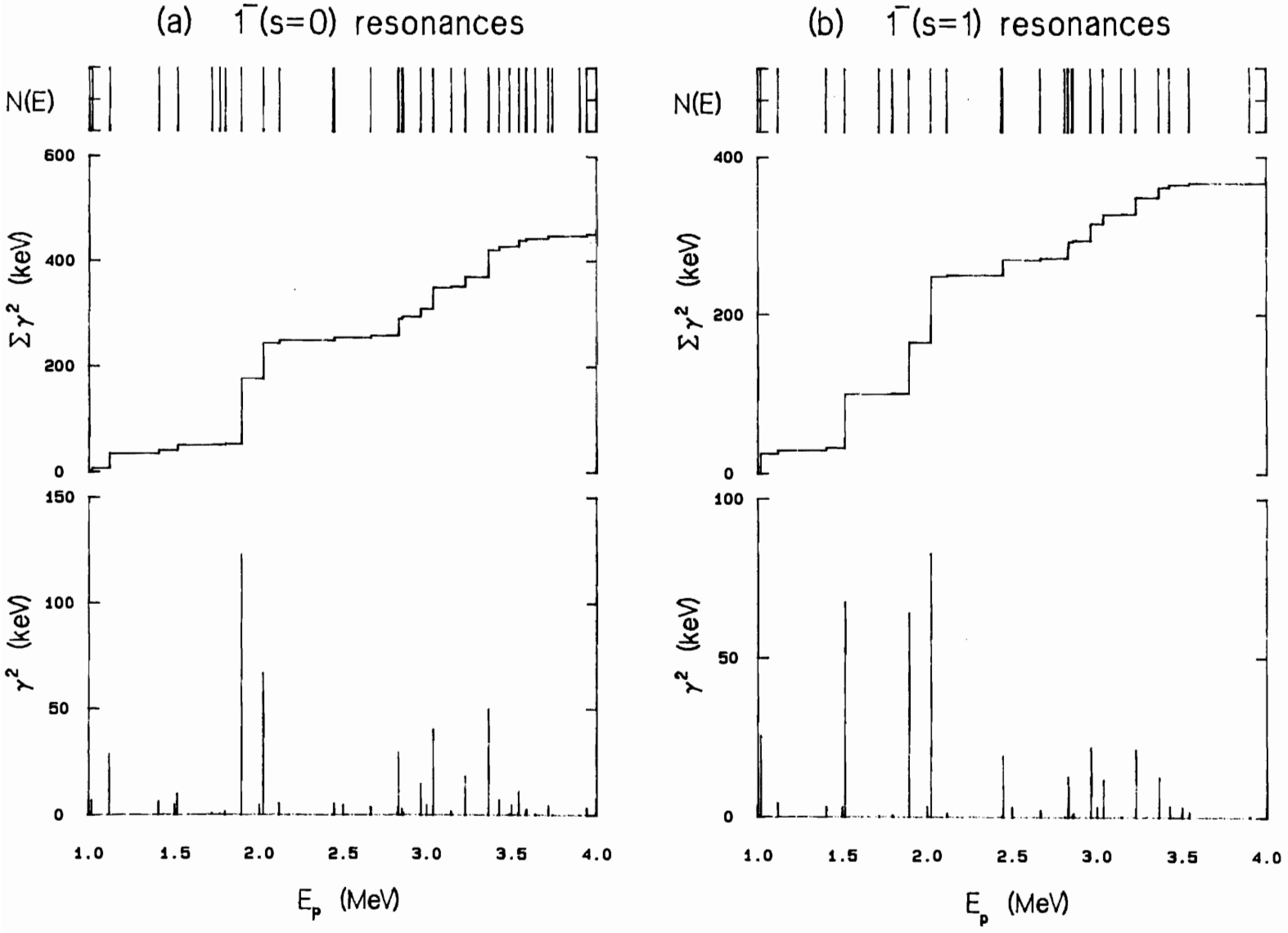
(a) 1⁻(s=0) resonances
N(E)
600
400
200
0
Σγ² (keV)
150
100
50
0
γ² (keV)
1.0
1.5
2.0
2.5
3.0
3.5
4.0
E_p (MeV)
(b) 1⁻(s=1) resonances
N(E)
400
200
0
Σγ² (keV)
100
50
0
γ² (keV)
1.0
1.5
2.0
2.5
3.0
3.5
4.0
E_p (MeV)

Figure 5.5 (a) Proton reduced widths versus energy for 2^-, $\ell = 1$ resonances in ^{32}S. A strong resonance is observed near 1.25 MeV. (b) Reduced widths for 2^-, $\ell = 3$ resonances.

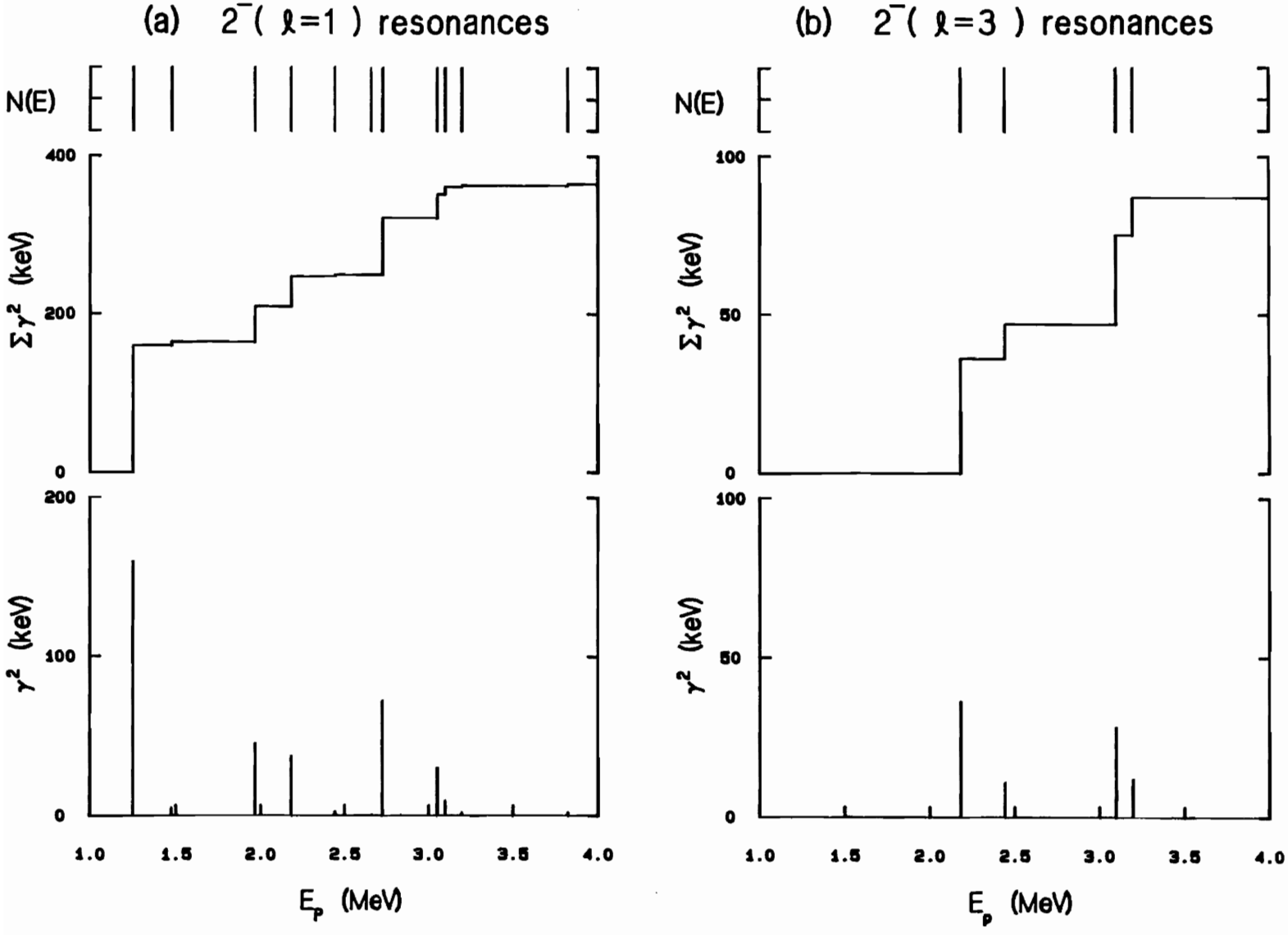
(a) 2⁻(ℓ=1) resonances
(b) 2⁻(ℓ=3) resonances
N(E)
Σγ² (keV)
γ² (keV)
E_p (MeV)
400
200
0
100
50
1.0
1.5
2.0
2.5
3.0
3.5
4.0

Figure 5.6 (a) Proton reduced widths versus energy for 2^+, $s = 0$ resonances in ^{32}S. Level clustering is seen near 2.00 MeV. (b) Reduced widths for 2^+, $s = 1$ resonances.

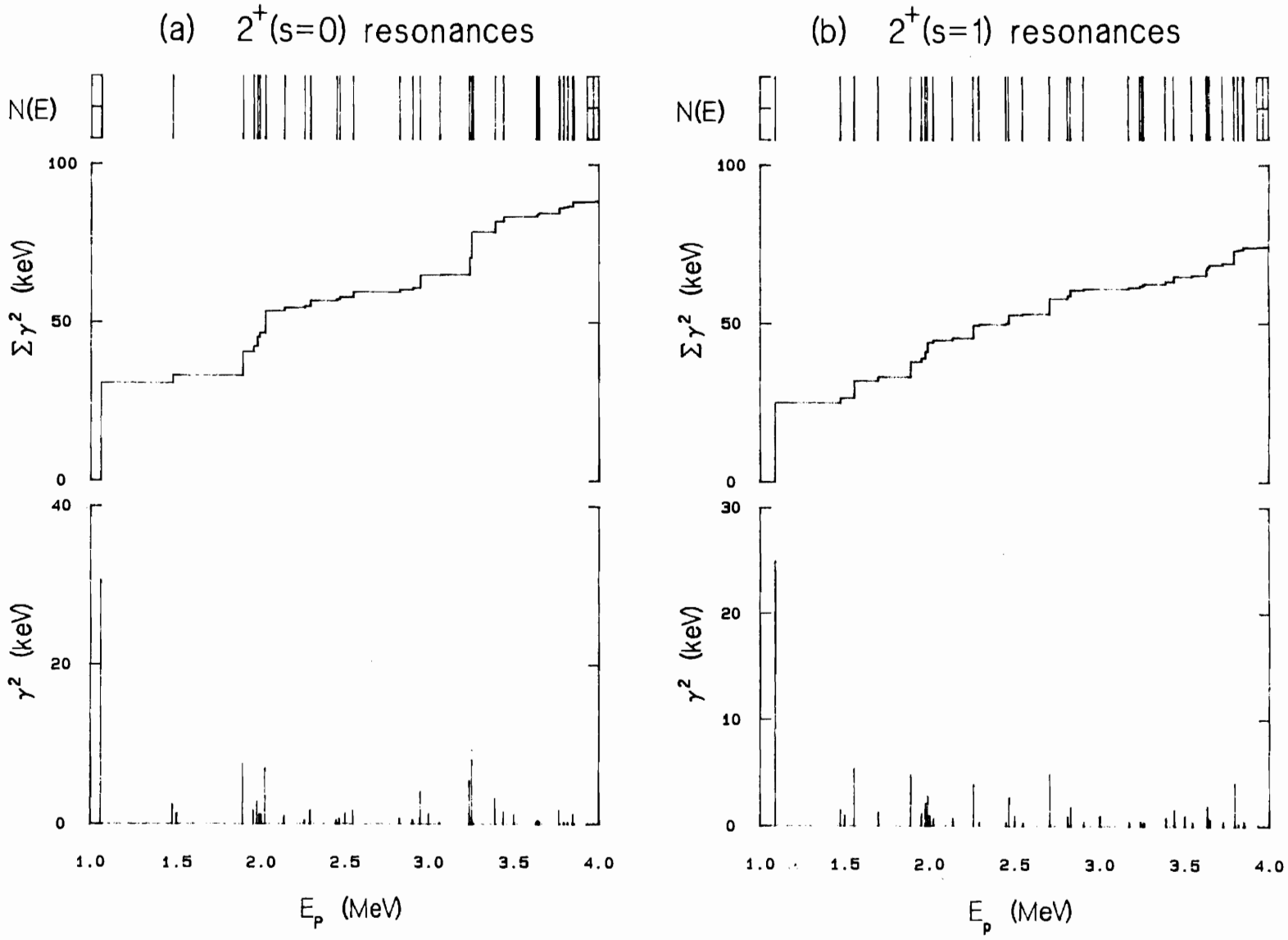
(a) 2+(s=0) resonances
(b) 2+(s=1) resonances
N(E)
Σγ² (keV)
γ² (keV)
E_p (MeV)
100
50
0
40
20
30
10
1.0
1.5
2.0
2.5
3.0
3.5
4.0

Figure 5.7 (a) Proton reduced widths versus energy for 3^-, $s = 0$ resonances in ^{32}S. Two strong resonances near 1.48 MeV are identified as analog resonances. (b) Reduced widths for 3^-, $s = 1$ resonances.

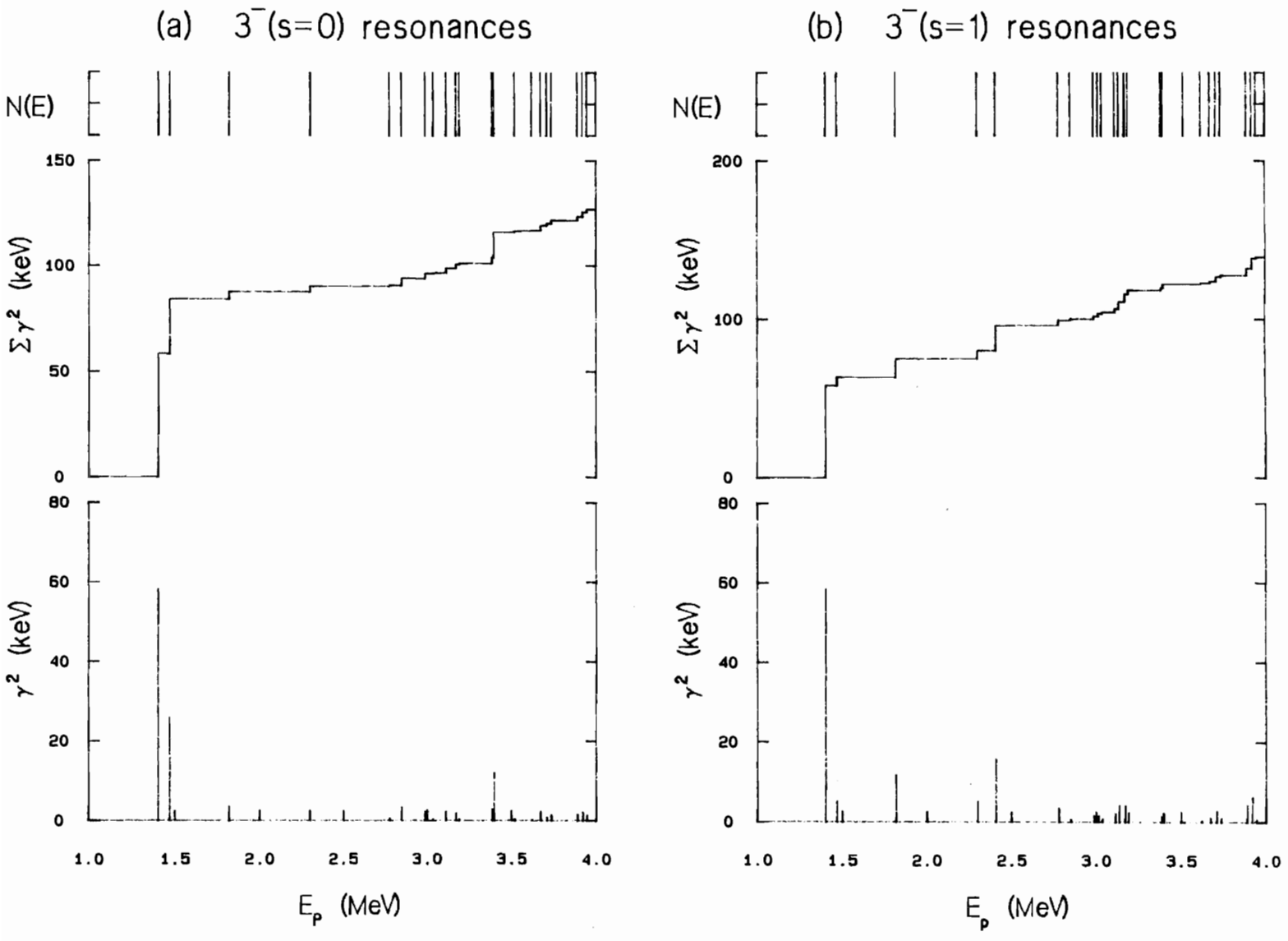
(a) 3⁻(s=0) resonances
(b) 3⁻(s=1) resonances
N(E)
Σγ² (keV)
γ² (keV)
E_p (MeV)
150
100
50
0
80
60
40
20
1.0
1.5
2.0
2.5
3.0
3.5
4.0
200

Figure 5.8 (a) Proton reduced widths versus energy for 3^+ resonances in ^{32}S. (b) Reduced widths for 4^- resonances. All the 4^- resonances are identified as analog resonances.

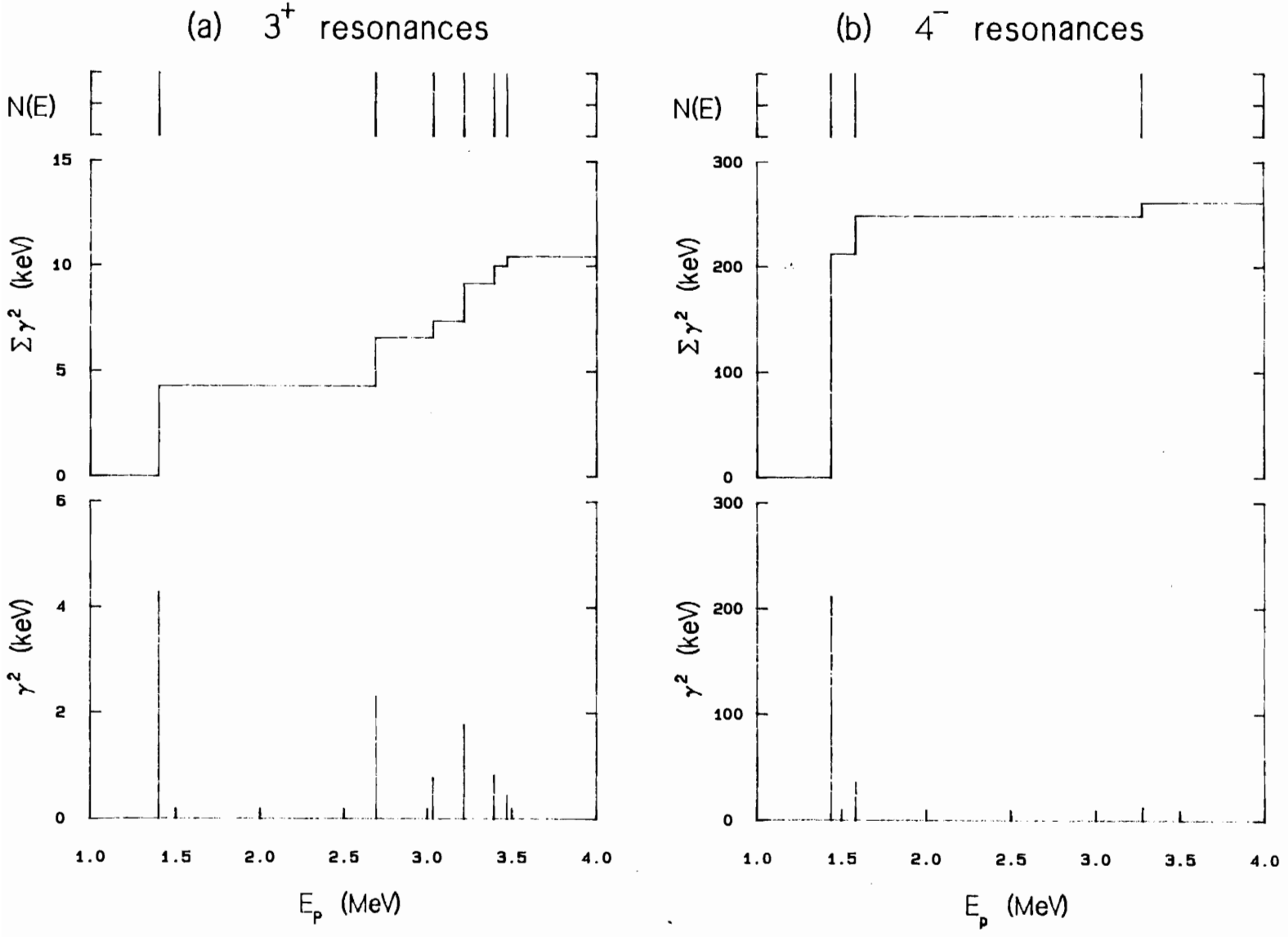
(a) 3+ resonances
(b) 4− resonances
N(E)
Σγ² (keV)
γ² (keV)
E_p (MeV)
1.0
1.5
2.0
2.5
3.0
3.5
4.0

usually small. The resonance at E_p = 1.250 MeV is an analog resonance, and the resonance at E_p = 2.181 MeV is identified as an analog resonance by the present experiment.

The strength distribution for thirty-six 2^+ levels is shown in figures 5.6a and 5.6b for different channel spin *s*. Since there is some ambiguity in determining the *s*-mixing ratio, the strengths presented for different *s* values are only approximately correct. The first two states near E_p = 1.06 MeV also have some uncertainties in the laboratory width, mainly because the quality of the experimental data is not good. The penetrabilities are very small at these energies, which results in a large variation of reduced widths for a small change in laboratory width. The resonances around E_p = 2.00 MeV are identified by the present experiment as fragmented analog resonances. There seems to be an analog state near E_p = 3.23 MeV, but there is no (*d, p*) data for comparison.

The strength information for twenty-five 3^- resonances is shown in figures 5.7a and 5.7b. The strengths are presented for different channel spins. There are some uncertainties in the channel spin mixing, especially for small resonances. The strong resonance at E_p = 1.403 MeV is an analog state, and the strength analysis suggests that there is no fragmentation of this state.

Only six 3^+ states are observed in the present experiment; their strengths are shown in figure 5.8a. The resonance at E_p = 1.400 MeV is barely seen in elastic scattering, and there is a large uncertainty in the laboratory width determination for this state. Overall the 3^+ states are fairly weak, agreeing with the sum-rule limits (see section D of this chapter).

The strengths for three 4^- states are shown in figure 5.8b. The resonances near E_p = 1.500 MeV are fragmented analog resonances. In Endt and Van der Leun's compilation (1978) the resonance at E_p = 3.2762 MeV was assigned T = 1, there are no (*d, p*) strength data.

C. Alpha Strength

Since ^{32}S is an alpha-nucleus, it is interesting to examine the ^{32}S structure from the viewpoint of α-clustering. The alpha-nuclei from ^{12}C to ^{24}Mg have been extensively studied for the last decade, and structure studies of ^{12}C to ^{20}Ne have made great progress, which was reviewed by Fujiwara *et al.* (1980). Alpha-nuclei with masses larger than A = 24 are not as well

studied theoretically. However, from the existing studies, some phenomena in nuclei with larger mass number can be explained by cluster correlations.

The excited states of ^{32}S can be divided into three regions: 1) The region from the ground state up to the α+^{28}Si threshold at 5.96 MeV (see figure 1.1). In this region the shell model structure is dominant. 2) The region from above the α+^{28}Si threshold to the energy near the ^{16}O+^{16}O threshold at 16.54 MeV. 3) The region higher than the top of the Coulomb barrier of the ^{16}O+^{16}O channel. Much experimental and theoretical work has been done in this region, and evidence for molecular structure was found in ^{32}S (Gay, 1987).

In the second region, which is the interest of the present experiment, the structure of ^{32}S is expected to be dominated by shell structure and by structure of the type α + residual α-nucleus. The α-clustering results in a higher probability for compound nuclear decay by emitting an α particle.

The α decay widths provide crucial information on the α-cluster structure. Usually, one examines the reduced widths and the spectroscopic factors of the alpha resonances. The plots for various J^{π} alpha resonance strengths extracted from the present experiment are shown in figures 5.9 and 5.10. The reduced width γ^2 is conventionally derived from the formula: $\gamma^2 = \Gamma/2P$, where Γ is the laboratory width and P is the penetrability of the α particles. To calculate the spectroscopic factor, one needs to know the "single particle width" for α decay from a compound nucleus. In this thesis the Wigner limit is chosen:

$$\gamma_W^2 = 3\hbar^2 / 2ma^2,$$

where a is the channel radius. However, there is some argument about the accuracy of this estimate, and in some analyses the factor 3/2 is omitted (Fifield, 1978).

In the present experiment, the α strengths are found to be generally small in units of the Wigner limit; the average spectroscopic factor is about 0.02. Several strong resonances are found with width about 10% of the Wigner limit. The strongest α resonance (at E_p = 1.516 MeV) has a reduced width of 0.27 γ_W^2.

Since the isospin of the ground state of both the α particle and ^{28}Si is zero, then if isospin is strictly conserved during α decay, the analog resonances (T = 1) can not have an α decay width.

Figure 5.9 (a) Alpha reduced widths versus energy for 0^+ resonances in ^{32}S. (b) Alpha reduced widths for 1^- resonances. Note there is a strong α resonance near 1.50 MeV.

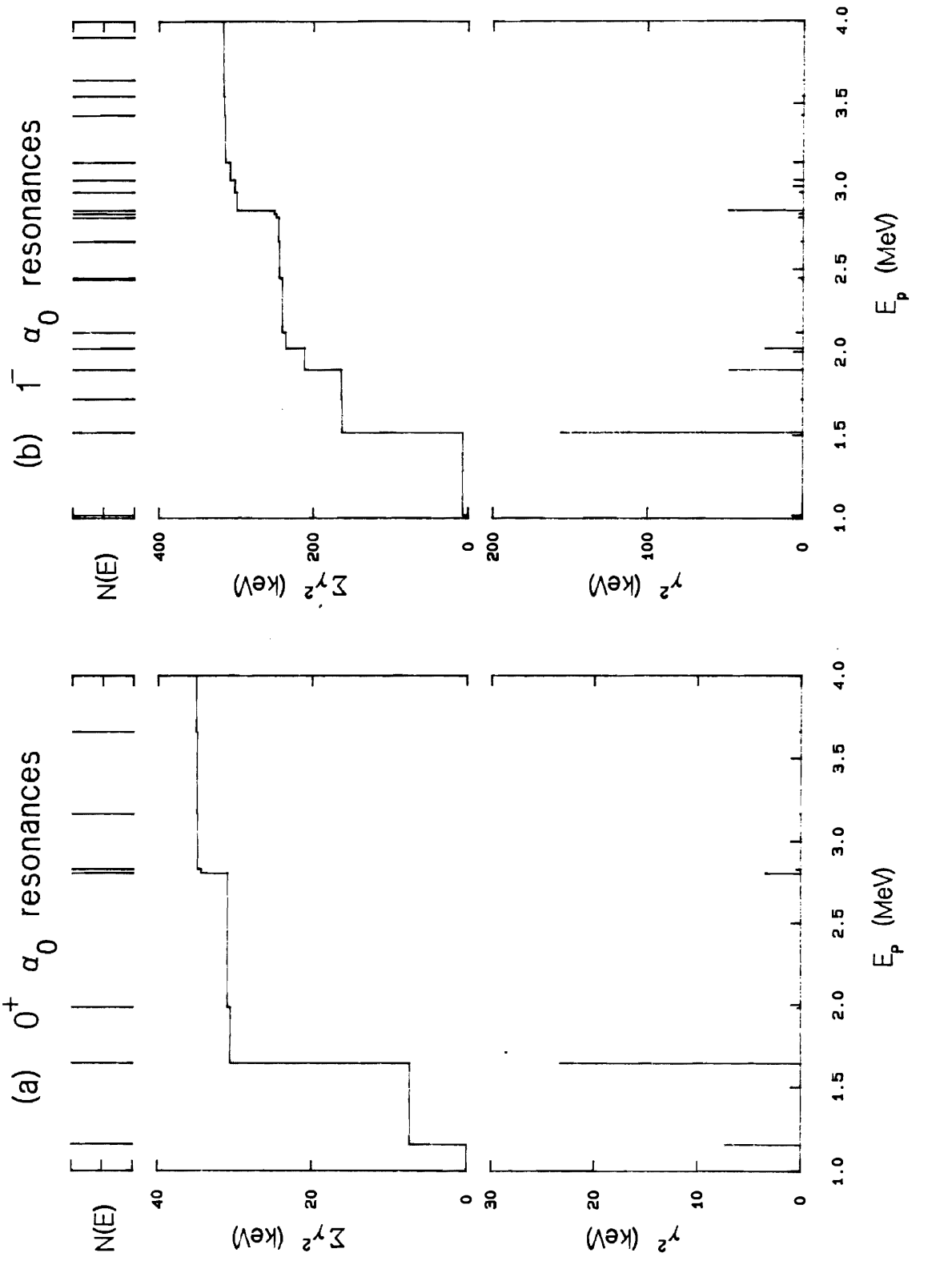
(a) 0^+ α_0 resonances
(b) 1^- α_0 resonances
N(E)
$\Sigma\gamma^2$ (keV)
γ^2 (keV)
E_p (MeV)

Figure 5.10 (a) Alpha reduced widths versus energy for 2^+ resonances in ^{32}S. (b) Alpha reduced widths for 3^- resonances. Three strong resonances were observed below 2.00 MeV.

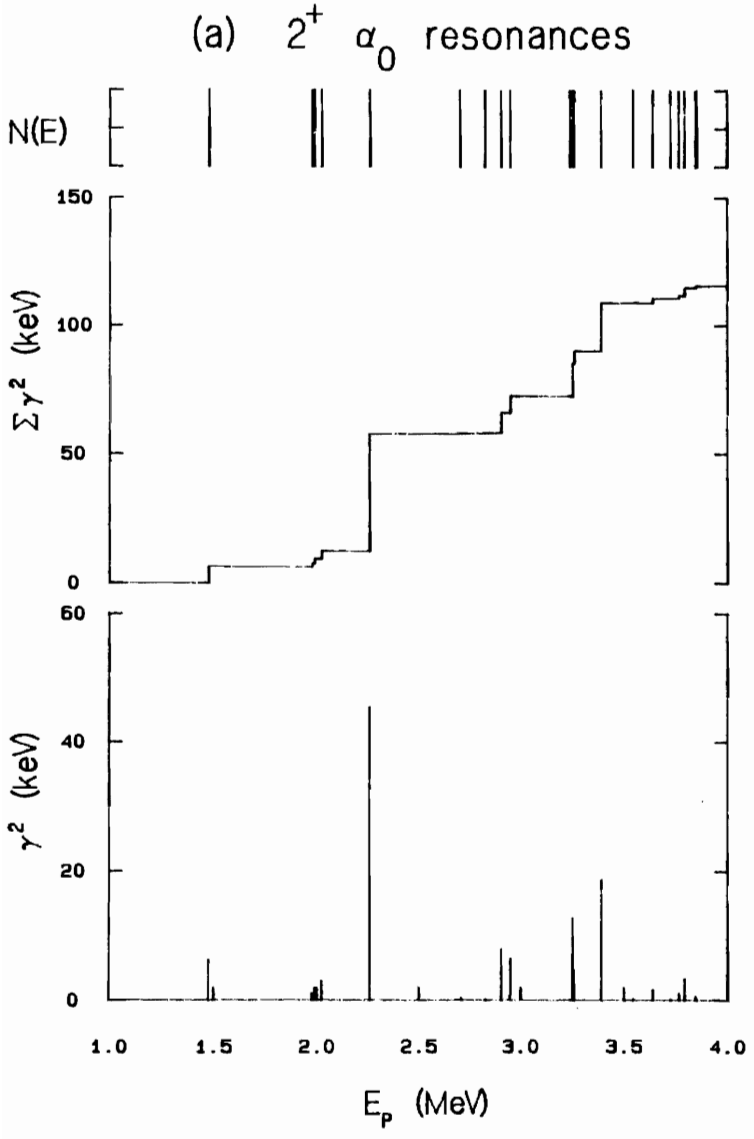
(a) 2^+ α_0 resonances
N(E)
$\Sigma\gamma^2$ (keV)
150
100
50
0
γ^2 (keV)
60
40
20
0
1.0
1.5
2.0
2.5
3.0
3.5
4.0
E_p (MeV)

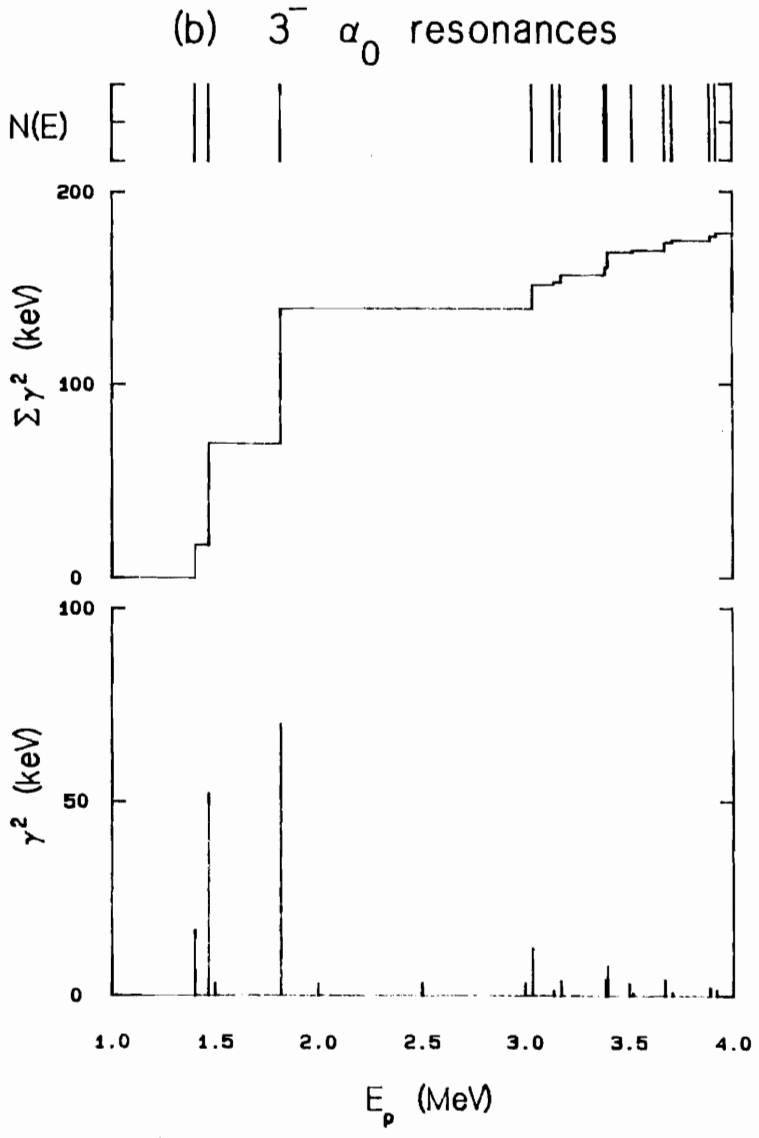
(b) 3^- α_0 resonances
N(E)
$\Sigma\gamma^2$ (keV)
200
100
0
γ^2 (keV)
100
50
0
1.0
1.5
2.0
2.5
3.0
3.5
4.0
E_p (MeV)

However, there are two 2^+ analog states near $E_p = 2.182$ MeV which have weak α decay, and the resonance at $E_p = 2.022$ MeV has a reduced width $\gamma^2 = 0.04\gamma_W^2$, which is nearly twice as large as the average reduced width. The energy position and the proton strength of this resonance derived from the present experiment agree well with the previous measurement (Kalifa *et al.*, 1978), which assigned this state as an analog resonance (see Table 5.1). This apparent contradiction may have several possible explanations: 1) The data quality is poor; 2) The isospin assignment is incorrect; 3) There is considerable isospin mixing. Since the data around this energy region were the best in the present experiment and the data are fit quite well, the first reason is very unlikely. Isospin conservation is violated by the Coulomb energy term in the Hamiltonian:

$$H_C = \sum_{i<j} (\frac{1}{2} - t_3^i)(\frac{1}{2} - t_3^j) \frac{e^2}{r_{ij}} \quad ,$$

where t_3^i is the isospin projection of the nulceon i in the nucleus. In general, isospin mixing is expected to be weak. For a uniform charged sphere of nucleus of radius R, the strength of the Coulomb potential averaged over the nucleus volume is $V_C = 3Ze^2/2R$. But if nucleon clustering exists, the isospin mixing may be "enhanced". This could be the reason for the observation of a comparatively large α decay width for the $T = 1$ state at $E_p = 2.022$ MeV, if the isospin assignment is correct. As an example, consider an α cluster in an extreme case in which two particles are formed separately inside of radius R with the uniform charge densities, the Coulomb potential is found to be $V_C = 2Z_\alpha Z_R e^2/R$, where Z_α is the charge number of α particle and $Z_\alpha + Z_R = Z$. One obtains

$$V_C^{\text{cluster}}/V_C^{\text{uniform}} = \frac{8}{3}(1 - \frac{2}{Z}) \sim \frac{8}{3} \qquad \text{for heavy nuclei.}$$

To prove this conjecture, one needs more detailed study.

It should be noted that the formation and decay of a comparatively long-lived compound nucleus in the reaction, at an energy where the density of states with different values of T is large, may result in severe breakdown of isospin selection rules (Browne, 1966).

The α_1 decay widths are plotted in figure 5.11. Note that the unnatural parity resonances can decay via the α_1 channel.

Figure 5.11 Reduced widths for $^{31}P(p, \alpha_1)$ resonances in the energy range E_p = 3.00 MeV to 4.00 MeV. In general the α_1 resonances are not strong.

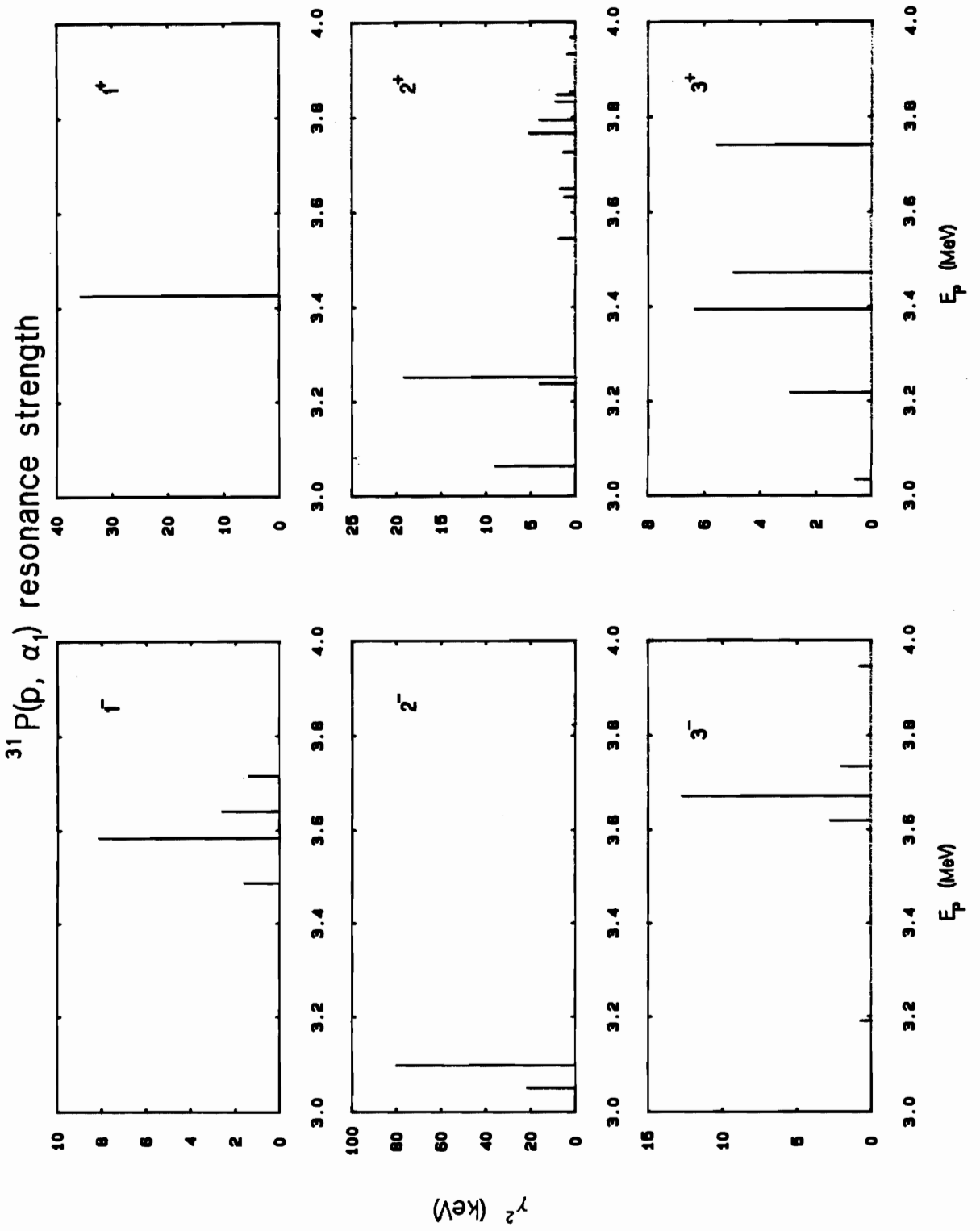
^{31}P(p, α_1) resonance strength
γ^2 (keV)
E_p (MeV)
1^-
2^-
3^-
1^+
2^+
3^+

D. Comparison with Shell Model Predictions and Sum-rule Limits.

When a single nucleon is added to a definite shell model orbit in a target nucleus, the total spectroscopic strength can be divided into two parts, with each characterized by the isospin value T. The summed spectroscopic strengths of the resonances are limited to a number which the specific nuclear configuration can provide. These limits are referred to as sum-rule limits (see chapter II C). The total strength in both T values is especially useful when the analog resonances are highly fragmented.

Consider the states produced when a proton is added to a specific shell model orbit *nlj*, and the target has a positive neutron excess $(N-Z) = 2M$. As discussed in section A, usually the isospin of the target is $T_t = M$. The addition of a proton leads to an excited state with isospin $T = T_t \pm 1/2$. The relation between the total spectroscopic strength for a proton added to the target and the number of the neutron and proton holes for the orbit *nlj* is (French and Macfarlane, 1962):

$$G_p(T_<) = \frac{1}{N-Z+1} < \text{neutron holes} >_{nlj}$$

$$G_p(T_>) = < \text{proton holes} >_{nlj} - \frac{1}{N-Z+1} < \text{neutron holes} >_{nlj} ,$$

where $< \text{holes} >_{nlj}$ is the average number of holes in the orbit *nlj*. Summing these two equations yields an interesting result:

$$G_p(T_<) + G_p(T_>) = <\text{proton holes}>_{njl} \quad .$$

In the present experiment M = 1/2, $T_< = 0$ and $T_> = 1$. The spectroscopic strengths are calculated by the relation $G_p = \Gamma_p / \Gamma_{s.p.}$, where Γ_p is the observed laboratory width and $\Gamma_{s.p.}$ is the single particle width. The single particle widths are estimated by a very simple equation (Bilpuch *et al.* 1976):

$$\Gamma_{s.p.} = 2P(R) \frac{5}{8} \hbar^2 / mR^2 , \qquad (5.4)$$

where $P(R)$ is the penetrability of the Coulomb barrier at the radius $R = 1.25(A^{1/3}+1)$. This equation reproduces of the values of single particle widths for the Woods-Saxon potential.

The resonance parameters derived from the present experiment are in the *LS* coupling

scheme, while the theoretical (shell model) calculations are usually based on the particle representation. In the two schemes the same three angular momenta, the spin of the incident particle s_p and the target s_t, and the orbital angular momentum l, are combined in two alternative ways:

$$s = s_t + s_p \qquad J = s + l \ , \qquad (1)$$

$$j = s_p + l \qquad J = s_t + j \ . \qquad (2)$$

The wave functions in the two bases are related by the unitary transformation

$$\psi_j = \sum_{lsJ} \hat{s}\hat{j} W(s_t s_p Jl; sj) \psi_{lsJ} \ , \qquad (5.5)$$

where $W(s_t s_p Jl; sj)$ is the Racah coefficient. From equation (2.20a), the reduced width amplitudes γ are directly linked to the channel spin wave functions. Thus the relation between the reduced width amplitudes in the two schemes is the same as (5.5), and the reduced widths γ^2 have the relation:

$$\gamma_j^2 = \gamma_j \cdot \gamma_j = \sum_{s'l'J', slJ} \hat{s'}\hat{j'}\hat{s}\hat{j} W(s_t s_p J'l'; s'l') W(s_t s_p Jl; sj) \gamma_{s'l'J'} \gamma_{slJ} \ . \qquad (5.6a)$$

Without complete information (including signs) about the reduced width amplitudes, one cannot actually perform this transformation. However, if the signs of the amplitudes are assumed random, the cross terms in (5.5) will cancel, and one obtains

$$\gamma_j^2 = \sum_{sJ} (2s+1)(2j+1) W^2(s_t s_p Jl; sj) \gamma_{slJ}^2 \ . \qquad (5.6b)$$

Since the spectroscopic strengths in the two schemes have the same relation, the strengths of various partial waves derived from the present experiment can be transformed to the j-representation to compare with the theoretical calculations.

Transformed strengths and shell model calculations in the energy range of the present experiment are listed in Table 5.2. The shell model predictions (Kalifa *et al.*, 1978) were obtained by diagonalizing in the complete $d_{5/2}$-$s_{1/2}$-$d_{3/2}$ basis space a Hamiltonian which reproduces the single-hole spectrum of A = 39 and simultaneously yields a root mean square best fit to a selected set of well known level energies in the A = 32 – 38 region. The spectroscopic factors for the ^{32}S

Table 5.2 Spectroscopic Strengths and Sum-rule Predictions

		Number	Present work		Shell model calculation[a]		Sum-rule
nlj	T	of levels	G_p[b]	$G_p\,(T_<+T_>)$[c]	G_p	$G_p\,(T_<+T_>)$[c]	limit
$1d_{5/2}$	0	41	0.096	0.106	0.032	0.132	0
$1d_{5/2}$	1	4	0.010		0.100		0
$2s_{1/2}$	0	21	0.046	0.046	0.002	0.05	1
$2s_{1/2}$	1	0	0.000		0.050		0
$1d_{3/2}$	0	44	0.099	0.109	0.001	0.085	2
$1d_{3/2}$	1	4	0.010		0.084		2
$2p_{3/2}$	0	41	0.539				2
$2p_{3/2}$	1	5	0.152				2
$1f_{7/2}$	0	21	0.075				4
$1f_{7/2}$	1	5	0.310				4

a) From Kalifa *et al.* (1978).

b) The spectroscopic strength G_p is dimensionless. The single particle widths are estimated with relation (5.4).

c) $T_< = 0$, $T_> = 1$.

resonances below $E_x(^{32}S)$ = 14.60 MeV were also calculated. From Table 5.2, one can see that the agreement of strengths between theory and experiment for different T values is not good, but the total strengths (sum over T values) agree very well. The reason may be that the analog resonances are not completely identified in the present energy range. For example, the shell model predicts that there is a 1^+, $T = 1$ state at $E_p = 2.1625$ MeV; experimentally a 1^+ resonance at the energy $E_p =$ 2.3316 MeV is observed and it is likely to be an analog resonance. A similar case is a 0^+ resonance (isospin undetermined) observed at $E_p = 3.055$ MeV; which the shell model predicts a 0^+ $T = 1$ state at $E_p = 3.0296$ MeV. These resonances, which have a contribution to the $2s_{1/2}$ strength, are treated as $T = 0$ states in Table 5.2.

The observed spectroscopic strengths are under the sum-rule limits except for the $1d_{5/2}$ and $2s_{1/2}$ shells. The simple shell model predicts that the total strength (including all the T values) in $1d_{5/2}$ is zero. The observed strength of 3^+ resonances, which in the excitation energy range of the present experiment can only be formed by placing a proton in $1d_{5/2}$ orbit, is about 0.01. Together with the contributions from 2^+ states, the measured spectroscopic strength G_p for the $1d_{5/2}$ shell is 0.1. This non-zero value may be caused by the oversimplified shell model description of the ground state of ^{31}P. The mixed configuration shell model predicts that there exists considerable vacancy in the $1d_{5/2}$ (1.76) and $2s_{1/2}$ (1.47) orbits for the ground state of ^{31}P, and that the vacancy in the $1d_{3/2}$ orbit will decrease due to the conservation of particles within the model space. The vacancy includes proton and neutron holes in that shell. To perform a direct quantitative comparison with the mixed configuration shell model, one needs to know the average number of holes for protons and neutrons separately.

However, there is a general question about the random sign assumption, which may not be valid in a selected energy region. Strong level-level interference effects (i.e., local correlations) are observed in the present experiment, and strong width amplitude correlations have been observed in resonance reactions in the *f-p* shell (Mitchell, 1985).

The ambiguity in the channel spin mixing ratio determination will result in uncertainties in the transformed reduced widths. To make a comprehensive comparison with sum-rule limits, one needs the complete spectroscopic information in the range in which the shell model theory is

effective. In the present case, one can only estimate the percentage of all the resonance strengths in this energy range.

E. Strength Functions

In the optical model of nuclear reactions, the incident particle is treated as in a complex potential, which is "absorptive". The Schrödinger equation has the form

$$\{ \frac{\hbar^2}{2m} \nabla^2 + [E-(V+iW)]\} \psi = 0 \ . \qquad (5.7)$$

The description of the nucleon-nucleus interaction in terms of an absorptive potential requires information about compound resonances. One approach to obtain a theoretical description of the resonances is with statistical methods, and of those methods, the simplest is to smooth the resonance fluctuations by taking an energy average. This procedure links the resonance expansion to the optical model. The consequent absorption calculated from (5.7) is proportional to the average probability of forming a compound nucleus. This is proportional to the fraction of the energy range occupied by the resonances, i.e., to the strength function

$$S = <\gamma^2>/D \ ,$$

where $<\gamma^2>$ is the average reduced width and D is the average energy between resonances (spacing). The averaging is accomplished experimentally by using poor resolution measurements or numerically by averaging good resolution data.

The optical potential $(V + iW)$ can be separated into several terms which are associated with physical quantities, such as isospin, spin-orbit coupling, spin-spin coupling, etc. Given a large enough set of resonances, the strength function will reflect the effects of all of these terms. Unfortunately, in the present experiment (and in almost all other experiments) the sample size is limited, and there are large statistical errors in the extraction of the numerical values. Thus before detailed discussion about measured strength functions, careful consideration should be given to the significance of strength function values (Lynn, 1965).

Suppose y and z are the two observables, or the sum of the observables, and the distribution

functions of y and z are $s(y)$ and $t(z)$. The joint distribution function of y and z is simply

$$p(y, z)dydz = s(y)t(z)dydz \quad .$$

From this joint function, one can calculate the probability of y being greater than a and z being less than y/b,

$$P(a, b) = \int_a^{\infty} s(y)dy \int_0^{y/b} t(z)dz \quad .$$

Thus, the probability of y/z being greater than b is $P(a, b)$. If the observable y (or z) is the summed reduced width of M (or N) resonances, then it can be assumed to obey the Porter-Thomas frequency function (note this is different from the ordinary Porter-Thomas distribution function) for a single resonance width:

$$p_M(y) = \Gamma(M/2)^{-1}(1/2\bar{x})^{M/2} y^{(N-2)/2} \exp(-y/2\bar{x}) \quad ,$$

where $x = y/M$. If the sample sizes M and N are even numbers, one obtains this expression for $P(0, b)$:

$$P(0, b) = 1 - \{(Mb)^M/(M-1)!\} \sum_{k=0}^{N-1} \frac{N^k(k+M-1)!}{k!\,(N+Mb)^{k+M}} \quad . \qquad (5.8)$$

This formula can be used to estimate the probability of the observed ratio for two strength functions with a value equal to or larger than b. In practice M and N are not always even. Calculations show that if b is fixed and M and N are not too small (~10), the probability $P(0, b)$ will change little as M (or N) change to $M\pm1$ (or $N\pm1$). Thus one can choose an even number of resonances by eliminating one of the weakest resonances. In the following subsections, the isospin dependence of the strength function, the s-wave, and p-wave strength functions will be discussed separately.

a) Isospin dependence

Lane (1962) proposed the addition of an isospin dependent term to the complex potential to explain a systematic feature in (p, n) reactions. If τ and T_t are the isospins of the incident nucleon and the target nucleus with mass A, then the additional term has the form

$$V' = V_1(\tau \cdot T_t)/A \quad , \qquad (5.9)$$

where V_1 is the strength of the potential and is independent of isospin. For proton scattering, this term is particularly interesting because $(\tau \cdot T_t)$ can be either T_3 or $-(T_3+1)$, where T_3 is the projection of T_t. If the isospin dependence is very strong, it will be reflected in a strength function difference between $S(T_<)$ and $S(T_>)$.

The strength function data from neutron experiments for different values of the neutron excess in the region of the $3s$ shell has been investigated (Lynn, 1965). A comprehensive review of the isospin dependence of the optical model was performed by Satchler (1969). He found that there is strong and convincing evidence for the existence of effects which can be adequately described in terms of (5.9) in the optical model. The number of resonances with $T_> = 1$ in the present experimental energy range is too small to eliminate the spin-orbit and possible spin-spin dependence of the optical potential. The comparison should be performed with the same J^π but different T states. This reduces the size of the samples. Together with the ambiguities in the isospin assignment, the significance of the comparison is poor.

No 0^+, 0^-, 1^+ and 3^+ resonances with $T = 1$ were observed in the present experiment; thus one cannot perform the comparison for these states. Two 1^-, $T = 1$ and thirty-two 1^-, $T = 0$ states are observed. The strength functions $S(T_<)$ and $S(T_>)$ are 0.68 and 0.17, respectively.

Four 2^+, $T = 1$ and twenty-six 2^+,$T = 0$ resonances were observed. The strength functions are $S(T_<) = 0.17$ and $S(T_>) = 0.02$.

The strength functions for ten 2^-, $T = 0$ and three 2^-, $T = 1$ resonances are 0.04 and 0.06, respectively.

Among twenty-three 3^- resonances two are identified as $T = 1$ states; the strength functions are $S(T_<) = 0.15$ and $S(T_>) = 0.13$.

All the 4^- resonances observed in the present experiment are identified as $T = 1$ states.

b) s-wave strength functions

The Bartlett spin-exchange force in the nucleon-nucleon interaction would result in a potential term which is dependent on the coupling of the spins of the incident nucleon and the target nucleus. It is assumed that this spin-spin term has the same form as in the isospin case,

$$V' = V_2 (i \cdot I)/A \quad .$$

Compared with the spin-orbit interaction term in the potential, this term is expected to be small. This may lead to the strength functions being insensitive to the spin-spin interaction effects. However, one can examine the s-wave cases, in which the V' becomes

$$V' = 0.5[J\,(J+1) - I\,(I+1) - i\,(i+1)]V_2/A\,,$$

where J is the spin of the compound nucleus. This extra potential term is zero for zero-spin targets. For non-zero-spin targets, one can obtain two s-wave strength functions with different J values. Neutron s-wave strength functions have been extracted from many measurements (Lynn, 1968). Previous measurements on s-wave proton resonances in ^{28}Si (Nelson, 1984) lead to a large ratio $S_{J=2}/S_{J=3} = 3.5$, while s-wave resonances in ^{24}Mg (Vanhoy *et al.* 1987) yielded $S_{J=1}/S_{J=2} = 0.61$. Proton resonance data on other odd-mass targets would be very important to establish systematics of the spin-spin dependence of the optical potential.

In the present experiment $J_< = 0$ and $J_> = 1$. Measured s-wave strength functions $S_{J=0}$ and $S_{J=1}$ are 0.005 and 0.013, respectively. The strength function ratio $S_{J=1}/S_{J=0}$ is 2.6 while the estimated probability for this ratio $P(0, b)$ is 0.017. This large difference in strength function is unlikely to reflect a true spin-spin effect. One of the ambiguities in the calculation is the possibility of analog resonances among the 1^+ states. These strong states might cause intermediate structure effects. The probability $P(0, b)$ estimation may be invalid since the Porter-Thomas distribution is then not suitable. If one eliminates those doubtful analog resonances, the s-wave strength functions are found to be $S_{J=0} = 0.005$ and $S_{J=1} = 0.007$ with $P\,(0, b) = 0.23$.

c) p-wave strength functions

The same arguments can be carried out for the p-wave resonances, except that the evidence for the angular momentum dependence of the p-wave strength function is much stronger due to the strong nucleon spin-orbit interaction.

Again the accuracy of the strength functions extracted from the present experiment is limited by the size of the samples. Only thirteen 2^- ($l = 1, s = 1$) states are observed, and of those three resonances are identified as analog resonances. Thirty-one 1^- ($l = 1, s = 1, T = 0$) resonances are satisfactorily analyzed. Calculated strength functions are: $S_{J=1}(l = 1, s = 1) = 0.11$ and $S_{J=2}(l = 1, s = 1) = 0.14$.

F. Applications to Nuclear Astrophysics

Nuclear astrophysics includes many aspects such as the structure and evolution of stars, the synthesis of the elements in stars, the structure and formation of neutron stars, etc. In this dissertation, only the thermonuclear reactions occurring during a certain stage of stellar evolution will be discussed.

Stellar evolution can be roughly divided into several stages, the earliest stage involving the reactions of hydrogen burning, the proton-proton chain, etc. These are the best studied topics in astrophysics. The hydrostatic helium burning becomes extremely important when the temperature of the star rises to $T_9 = 0.1$, where T_9 is in units of 10^9 K. During this stage 3α and $^{12}C(\alpha, \gamma)^{16}O$ reactions produce ^{12}C and ^{16}O and determine their abundance ratio, which is crucial for later evolution and for element abundances. When the helium is depleted and the temperature rises to $T_9 = 1.0$ as the star contracts, the third main burning reaction is carbon fusion with several exit channels:

$$^{12}C + {}^{12}C \longrightarrow {}^{23}Na + p + 2.24\ MeV$$
$$^{20}Ne + \alpha + 4.62\ MeV$$
$$^{23}Mg + n - 2.60\ MeV\ .$$

This process is the third great source of power for stellar evolution. During this stage many A<28 elements are synthesized or produced by a network of nuclear reactions. These elements are the "seeds" for future synthesis. The carbon burning can proceed hydrostatically or explosively, the latter case occurring at temperatures near $T_9 = 2.0$, with the carbon fusion and its secondary network reactions occurring vigorously for about 1/10 second. When the temperature in the star reaches $T_9 = 1.5$ the $^{16}O + {}^{16}O$ reaction becomes one of the main burning processes, which is usually referred to as the oxygen burning stage. Similar to the explosive carbon burning, explosive oxygen burning occurs at $3.0 < T_9 < 4.0$, with its secondary network of nuclear reactions which produce the elements around A = 32. The principle reaction in the oxygen burning stage is the interaction of two ^{16}O nuclei to produce the compound nuclear states of ^{32}S, which has four particle decay channels:

$$^{16}O + {}^{16}O \longrightarrow (^{32}S)^* \longrightarrow {}^{28}Si + \alpha + 9.59\ \text{MeV} \quad 34\%$$
$$^{31}P + p + 7.68\ \text{MeV} \quad 56\%$$
$$^{31}S + n + 1.45\ \text{MeV} \quad 5\%$$
$$^{30}P + d - 2.41\ \text{MeV} \quad 5\%\ .$$

These processes are also sources of power for stellar evolution. One can see that the nuclear structure of ^{32}S is very important for the thermonuclear reaction rate calculation.

It is assumed that the velocities of the particles inside a star obey a Maxwellian distribution. The $^{16}O + {}^{16}O$ reaction has a huge Coulomb barrier at low energies, which results in a very small entrance laboratory width. At the temperature of hydrostatic ($1.5 < T_9 < 2.5$) and explosive oxygen burning, only those ^{16}O particles in the long tail of Maxwellian distribution are involved in the reaction. The estimated center of mass energy for oxygen burning is in the range of 4.2 – 14.9 MeV (Clayton *et al.* 1974). This corresponds to ^{32}S excitation energy in the range of 20 – 30 MeV. Unfortunately, the present experiment cannot reach this region.

However, during the explosive oxygen (and the explosive silicon) burning, the reaction $^{28}Si(\alpha, p)^{31}P$ plays an important role which involves the structure of ^{32}S in the excitation energy range of 9.44 – 14.14 MeV. The present experiment provides information about the resonances in this region. The reaction $^{28}Si(\alpha, p)^{31}P$ is crucial for the final abundance of ^{31}P and ^{28}Si at the end of the oxygen burning stage, and the abundance of ^{28}Si is extremely important for future silicon burning.

The reaction rates at astrophysically interesting temperatures may be obtained by numerically integrating the equation (Woosley, 1973):

$$N_A\langle\sigma v\rangle = \int_0^\infty \sigma(v)\, v\, \phi(v, T)\, dv \qquad (5.10)$$
$$= 3.734 \times 10^{10} A^{1/2} T_9^{-3/2} \int E\sigma(E) \exp(-11.605E/T_9)\, dE \qquad \text{cm}^3\text{mole}^{-1}\text{sec}^{-1}.$$

where $\phi(v, T)$ is the Maxwellian distribution function, N_A is Avogadro's constant, $\sigma(E)$ is the measured reaction cross section in barns, A is the reduced mass of the interacting particles, and E is the center-of-mass energy in MeV.

From the detailed balance principle, the cross section of the reaction $1 + 2 \rightarrow 3 + 4 + Q_{12,34}$, and the cross section of the reaction $3 + 4 \rightarrow 1 + 2 + Q_{34,12}$ have the relation

$$(2J_1+ 1)(2J_2+ 2)\ \frac{\sigma(12, 34)}{\lambda_{12}^{2}} = (2J_3+ 1)(2J_4+ 1)\ \frac{\sigma(34, 12)}{\lambda_{34}^{2}} \quad ,$$

where λ_{12} and λ_{34} are wavelengths for particle pairs 12 and 34, respectively. One can show that the reaction rate for the inverse reaction is

$$<\sigma v>_{34, 12} = <\sigma v>_{12, 34}(\frac{M_{12}}{M_{34}})^{3/2}\frac{(2J_1+ 1)(2J_2+ 1)}{(2J_3+ 1)(2J_4+ 1)}\exp(-\frac{Q_{12, 34}}{kT}) \quad ,$$

where M is the reduced mass of the channel. From equation (5.10) one can see that the Maxwellian distribution requires that the majority of the particle pairs have low velocities, while the cross section $\sigma(v)$ is a function of relative velocity of the interacting pair, and the density of interacting pairs will drop exponentially as the interaction energy (velocity) decreases. Thus, at a certain temperature T_9 there exists a "most effective energy" range $(E_0 - \Delta E/2,\ E_0 + \Delta E/2)$ in which interacting particle pairs make the main contribution to the thermonuclear reaction rates at that temperature, i.e.,

$$E_0 = 0.122(Z_1^{2}Z_2^{2}A)^{1/3}T_9^{2/3}\ \text{MeV} \quad ,$$

where A is the reduced atomic mass and E_0 is the center-of-mass energy, and

$$\Delta E = 0.237(Z_1^{2}Z_2^{2}A)^{1/6}T_9^{5/6}\ \text{MeV} \, .$$

Assuming the temperature T_9 is in the range 1.0 – 10.0, then for the $^{28}Si(\alpha, p)^{31}P$ reaction the "most effective energy" range is $E_\alpha^{cm} = 1.26 - 10.95$ MeV. The thermonuclear reaction rates in this range can be obtained either by measuring (α, p) directly or by measuring the inverse reaction (p,α) in the energy range $E_p^{cm} = 0.0 - 9.0$ MeV. However, at the lower energy end the (α, p) measurement will have a very high Coulomb barrier. Thus, it is more practical to measure the inverse reaction. The present experiment provides the total cross section for $^{31}P(p, \alpha)^{28}Si$ in the range of $E_p^{cm} = 0.97 - 3.88$ MeV, as shown in figure 5.12 (a). If only the ground state reactions are considered, by integrating these cross sections with equation (5.10), one obtains the reaction rates for either direction at certain temperatures. Calculated results are listed in Table 5.3.

Direct measurement of the $^{28}Si(\alpha, p)^{31}P$ reaction was performed by Buckby and King

Figure 5.12 (a) Integrated cross section for the reaction $^{31}P(p, \alpha_0)$. Resonance parameters are from the present experiment. (b) Comparison of thermonuclear reaction rates for $^{28}Si(\alpha, p)$ with a theoretical calculation (Woosley, 1973).

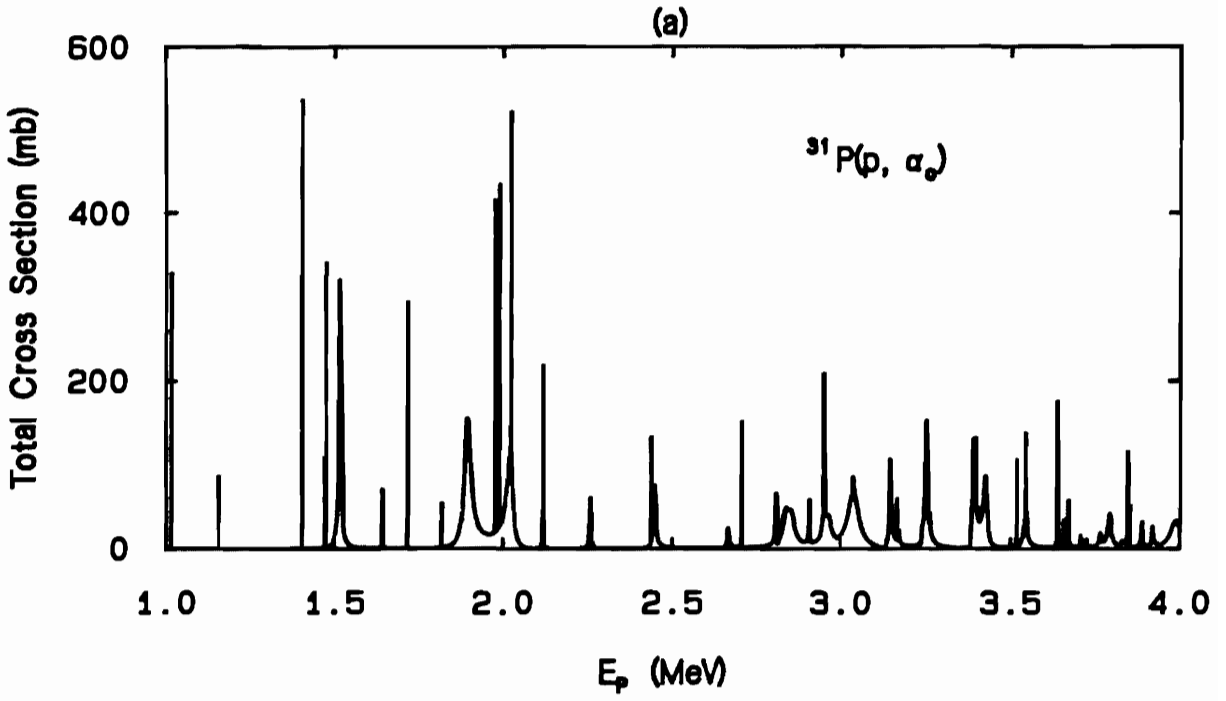
(a)
600
400
200
0
Total Cross Section (mb)
^{31}P(p, α_0)
1.0
1.5
2.0
2.5
3.0
3.5
4.0
E_p (MeV)

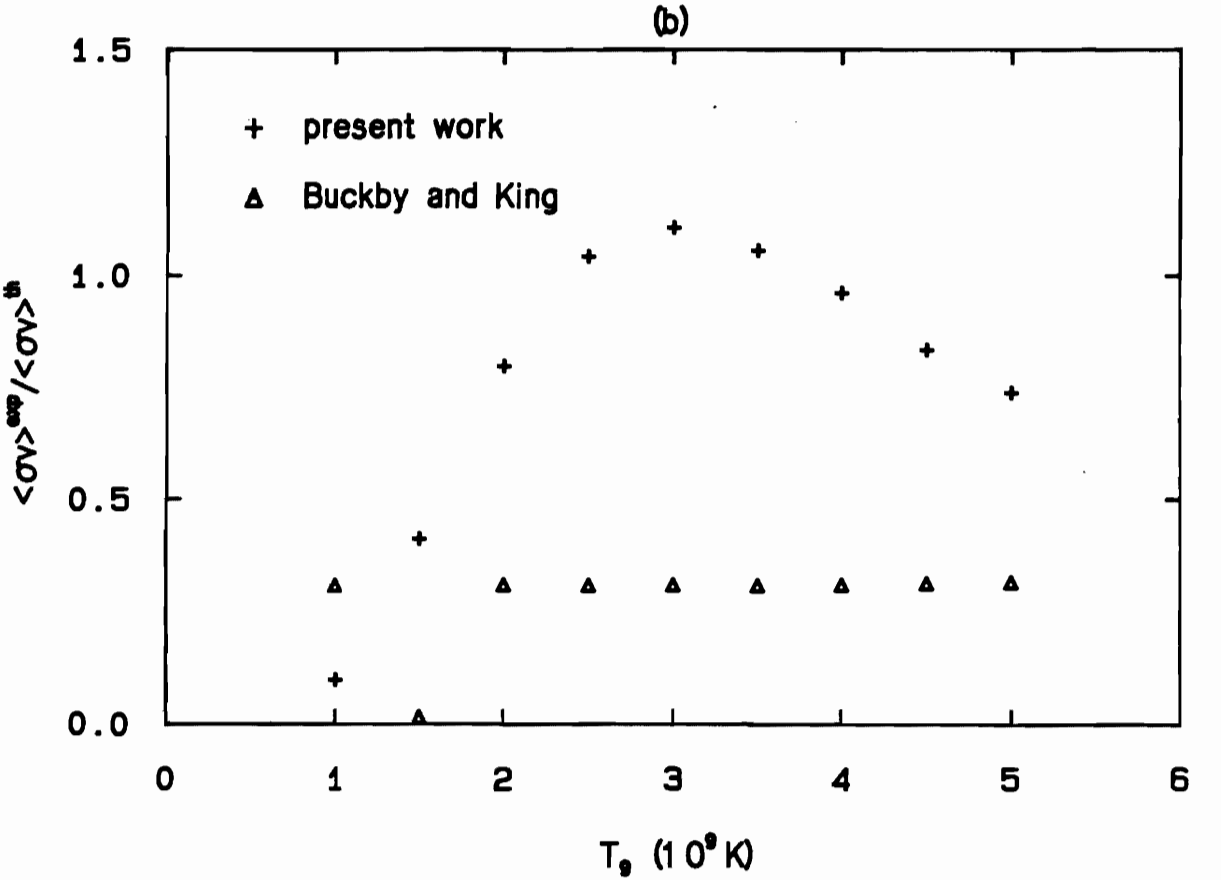
(b)
1.5
1.0
0.5
0.0
$<\sigma v>^{exp}/<\sigma v>^{th}$
+ present work
Δ Buckby and King
0
1
2
3
4
5
6
T_9 (10^9 K)

Table 5.3 Ground State Thermonuclear Reaction Rates

T_9 (10^9 K)	$N_A\langle\sigma v\rangle_{p\alpha}$ [a]		$N_A\langle\sigma v\rangle_{\alpha p}$ [a]			Main Burning [b]	Importance Value [e]
	Present work	Theory [c]	Previous work [a]	Present work	Theory [c,d]		
1.0	$2.54\ 10^{1}$		$1.24\ 10^{-8}$	$3.92\ 10^{-9}$	$4.04\ 10^{-8}$	HyC	
1.5	$1.59\ 10^{3}$		$3.11\ 10^{-4}$	$4.14\ 10^{-4}$	$1.01\ 10^{-3}$	HyC	
2.0	$1.57\ 10^{4}$		$6.74\ 10^{-2}$	$1.75\ 10^{-1}$	$2.19\ 10^{-1}$	ExC, HyOx	3
2.5	$6.43\ 10^{4}$		$2.04\ 10^{0}$	$6.94\ 10^{0}$	$6.66\ 10^{0}$	HyOx	3
3.0	$1.64\ 10^{5}$		$2.25\ 10^{1}$	$8.11\ 10^{1}$	$7.33\ 10^{1}$	ExOx	2
3.5	$3.20\ 10^{5}$	$2.50\ 10^{5}$	$1.36\ 10^{2}$	$4.28\ 10^{2}$	$4.43\ 10^{2}$	ExOx, ExSi	2
4.0	$5.26\ 10^{5}$		$5.58\ 10^{2}$	$1.74\ 10^{3}$	$1.81\ 10^{3}$	ExOx, ExSi	2
4.5	$7.66\ 10^{5}$	$4.88\ 10^{5}$	$1.76\ 10^{3}$	$4.73\ 10^{3}$	$5.67\ 10^{3}$	ExSi	3
5.0	$1.03\ 10^{6}$		$4.58\ 10^{3}$	$1.08\ 10^{4}$	$1.46\ 10^{4}$	ExSi	3
5.5	$1.31\ 10^{6}$		$1.03\ 10^{4}$	$2.09\ 10^{4}$			

a) $N_A\langle\sigma v\rangle_{p\alpha}$ stands for the thermonuclear reaction $^{31}P(p, \alpha)^{28}Si$ rates. Reaction rates are in units of $cm^3 mole^{-1} sec.^{-1}$

b) HyC, ExOx... stands for the hydrostatic carbon burning, explosive oxygen burning...

c) Woosley *et al.* (1973)

d) Buckby *et al.* (1984)

e) Clayton *et al.* (1974)

(1984). They measured the absolute cross sections for the laboratory bombarding energies over the range $5.52 \leq E_\alpha \leq 12.0$ MeV (or $4.83 \leq E_\alpha^{cm} \leq 10.5$ MeV) and deduced rates for the reaction over the range of energies relevant to nucleosynthesis. Their results were found to be lower by as much as a factor of three compared with statistical model calculations, and these results are shown in figure 5.12 (b) (reaction rates are normalized to the theoretical calculation). This is not surprising since their energies are quite far beyond the effective energy range for $T_9 = 2.0 \sim 5.0$ ($2.0 \leq E_\alpha^{cm} \leq$ 6.7 MeV).

Figure 5.12 (b) also shows the reaction rates deduced from the present experiment. The agreement between the present work and the theoretical predictions is good except at the lower end and higher end of the temperatures. This may be due to the lack of resonance parameters below 0.98 MeV and above 3.88 MeV in the calculation. Fortunately, the $^{28}Si(\alpha, p)^{31}P$ reaction is assumed to occur mostly at the stage of explosive carbon and explosive oxygen burning, as shown in Table 5.3, so the reaction at lower temperatures is not very important. The importance values for the reaction are adopted from Clayton's (1974) notation, in which a value of 2 indicates that the cross section value has direct effects on the observed abundance, and 3 indicates the cross section measurement is desirable because the cross sections has measurable effects on the observed abundance.

To determine $^{28}Si(\alpha, p)^{31}P$ reaction rates at the explosive silicon burning ($3.5<T_9<5.5$) stage, one needs either to measure the (α, p) reaction directly, or to measure the (p, α) reaction at higher energies than in the present experiment.

Chapter VI

Summary

Differential cross sections were measured for $^{31}P(p, p)$, (p, p_1), (p, α_0) and (p, α_1) in the range E_p = 1.00 to 4.01 MeV. Resonance parameters were extracted for 143 resonances in ^{32}S in this energy range with a multi-level, multi-channel R-matrix analysis code. These parameters include resonance energies, spins and parities, partial elastic and reaction widths, channel spin or orbital angular momentum mixing ratios, and relative signs of resonance width amplitudes for some resonances.

The R-matrix theory and the angular correlation theory were briefly discussed as they relate to the present analysis. Theoretical expressions for level-level interference were derived with the level expansion method.

Seven analog resonances were identified, and an inversion of levels in the parent and daughter nuclei was qualitatively explained by the Thomas-Erhman shift. Several other resonances are probably analogs. Since there is no strength information for these states from stripping reactions, firm identification is not possible.

Shell model calculations and sum-rules were discussed and comparison was made with the present data. Comparison for T values separately is unsatisfactory due to the incompleteness of the identification of analog resonances, but comparison with the summed strength $(T_> + T_<)$ is excellent.

The strength functions for elastic scattering were obtained to investigate the nucleon-nucleus dependence on isospin, spin-spin and spin-orbit interactions. The measured s-wave strength function ratio $S_{J=1}/S_{J=0}$ = 1.4. Several strong α_0 resonances were observed, and a relatively strong isospin forbidden α_0 decay was observed and qualitatively explained in terms of α-clustering.

The application of the spectroscopic results to astrophysics was described. By using the principle of detailed balance, the thermonuclear reaction rates of $^{28}Si(\alpha, p_0)^{31}P$ were calculated

with the resonance parameters extracted from the present (p, α) experiment. Comparison with theoretical predictions and the previous (α, p) measurement was made.

Results from the present experiment show agreement with the shell model calculations, but suggest that more detailed studies are needed. Since many detailed theoretical calculations require identification of the analog resonances, the spectroscopic information about ^{32}P through the (d, p) reaction should be extended. More detailed and systematic studies on sign effects of level-level interference would be interesting. The α-cluster model calculation should be extended to ^{32}S to better understand the strong α decay. A systematic investigation on isospin mixing in α_0 decay (or isospin forbidden transitions) would be very interesting. Several resonances in ^{32}S were found to have large proton inelastic decay widths. It would be very interesting to investigate these states in the future. Study of the nuclear spectroscopy of ^{32}S at higher energies would also be very interesting. For example, information near the Coulomb barrier for ^{16}O + ^{16}O (about 16.0 MeV excitation energy in ^{32}S) would be extremely important for astrophysics.

Bibliography

Adams, G. *Proton Resonance Spectroscopy in ^{26}Al*. M. S. thesis, North Carolina State University, 1983

Biedenharn, L. C., Blatt, J. M. and Rose, M. E. *Rev. Mod. Phys.* **32**, 249 (1952)

Biedenharn, L. C. *Nuclear Spectroscopy* part B, ed. F. Ajzenberg-Selove (Academic Press, New York, 1960)

Bilpuch, E. G., Lane, A. M., Mitchell, G. E., and Moses, J. D. *Phys. Reports* **28**, 145 (1976)

Bohr, N. *Nature* (London) **137**, 344 (1936)

Browne, C. D. *Isobaric Spin in Nuclear Physics* ed. D. Robson (Academic Press, Now York, 1966)

Buckby, M. A. and King, J. D. *Can. J. Phys.* **62**, 134 (1984)

Clayton, D. D. and Woosley, S.E. *Rev. Mod. Phys.* **46**, 755 (1974)

Devons, S. and Goldfarb, L. J. B. *Angular Correlations* in *Handbuch der Physik* Vol. **42** ed. S. Flügge (Springer-Verlag, Berlin, 1957)

Endt, P. M. and Van der Leun, C. *Nucl. Phys.* **A310**, 1 (1978)

Ferguson, A. J. *Angular Correlation Methods in Gamma-ray Spectroscopy* (North Holland, Amsterdam, 1965)

Fifield, L. K., Garman, M. J., Hurst, M. J., Symons, T. J. M., Watt, F., Zimmerman, C. H. and Allen, K. W. *Nucl. Phys.* **A322**, 1 (1979)

Freedman, S. J., Gagliardi, C. A., Oothoudt, M. A., Nero, A. V., Roberson, R. G., Zutavern, F. J., Adelberger, E. G. and McDonald, A. B. *Phys. Rev.* **C19**, 1907 (1979)

French, J. B. and Macfarlane, M. H. *Nucl. Phys.* **26**, 168 (1962)

Fujiwara, Y., Horiuchi, H., Ikeda, K., Kamimura, M., Katõ, K., Suzuki, Y. and Uegaki, E. *Prog. Theo. Phys. Suppl.* (Japan) **68**, 29 (1980)

Gay, D. L., Fletcher, N. R. and Penins, L. C. *Phys. Rev. Lett.* **58**, 1512 (1987)

Gould, C. R. and Roberson, N. R. *IEEE Trans. Nucl. Sci.* Ns-32 (1985) 1447

Harney, H. L. *Nucl. Phys.* **A119**, 591 (1968)

Harney, H. L. and Weidenmüller, H. A. *Nucl. Phys.* **A139**, 241 (1969)

Holterbekk, T. *Nucl. Phys.* **37**, 353 (1962)

Hooton, B. W. *Nucl. Instrum. Methods* **27**, 338 (1964)

Humblet, J. and Lebon, G. *Nucl. Phys.* **69**, 113 (1965)

Jänecke, J. *Isospin in Nuclear Physics* ed. D. H. Wilkerson (North Holland, Amsterdam, 1969)

Kalifa, J., Verrotte, J., Deschamps, Y., Poughou, F., Rotbard, G., Vergnes, M. and Wildenthal, B. H. *Phys. Rev.* **C17**, 1961, (1978)

Kapur, P. L. and Peierls, R. E. *Proc. Roy. Soc.* **A166**, 277 (1938)

Keyworth, G. A. *A High Resolution Study of Isobaric Analog States in ^{41}K and ^{23}Na .* Ph. D. dissertation, Duke University, 1968

Lane, A. M. and Thomas, R. G. *Rev. Mod. Phys.* **30**, 257 (1958)

Lane, A. M. *Phys. Rev. Lett.* **8**, 171 (1962)

Lynn, J. E. *Phys. Lett.* **18**, 31 (1965)

Lynn, J. E. *The Theory of Neutron Resonance Reactions* (Clarendon Press, Oxford, 1968)

Macfarlane, M. H. and French, J. B. *Rev. Mod. Phys.* **32**, 567 (1960)

Marion, J. B. *Rev. Mod. Phys.* **38**, 660 (1966)

McCarthy, I. E. *Introduction to Nuclear Theory* (J. Wiley and Sons, New York, 1968)

Mitchell, G. E., Bilpuch, E. G., Shriner, J. F. Jr. and Lane, A. M. *Phys. Reports* **117**, 1 (1985)

Moses, J. D. *A High Resolution Study of Isobaric Analog Resonances in ^{51}Mn ,^{53}Mn and ^{55}Mn .* Ph. D. dissertation, Duke University, 1969

Nelson, R. O. *Proton Resonance Spectroscopy in ^{28}Si and ^{30}P.* Ph. D. dissertation, Duke University, 1983

Nelson, R. O., Bilpuch, E. G., Westerfeldt, C. R. and Mitchell, G. E. *Phys. Rev.* **C30**,755, (1984)

Parks, P. B., Newson, H. W. and Williamson, R. M. *Rev. Sci. Instrum.* **29**, 834 (1958)

Roman, P. *Advanced Quantum Theory* (Addison-Wesley, Boston, 1965)

Satchler, C. R. *Isospin in Nuclear Physics* ed. D. H. Wilkinson (North Holland, Amsterdam, 1969)

Sellin, D. L. *Excited States in ^{19}F* . Ph. D. dissertation, Duke University, 1968

Shiff, L. I. *Quantum Mechanics* . 3rd ed. (McGraw-Hill, New York, 1968)

Tobocman, W. *Theory of Direct Reactions* . (Oxford University Press, London, 1961)

Vanhoy, J. R. *Proton Resonance Spectroscopy in ^{24}Mg* . Ph. D. dissertation, Duke University, 1986

Vanhoy, J. R., Bilpuch, E. G., Westerfeldt, C. R. and Mitchell, G. E. *Phys. Rev.* **C** (to be published)

Venotte, J., Gales, S., Langevin, M. and Maison, J. M. *Phys. Rev.* **C8**, 173 (1973)

Vogt, E. *Phys. Rev.* **112**, 203 (1958)

Warthen, B. J. *Nuclear Resonance Spectroscopy in ^{40}Ca* . Ph. D. dissertation, Duke University, 1987

Weidenmüller, H. A. *Nucl. Phys.* **69**, 113 (1965)

Westerfeldt, C. R., Nelson, R. O., Bilpuch, E. G. and Mitchell, G. E. *The TUNL High Resolution Laboratory System and Operating Procedures.* Duke University, 1986

Wigner, E. P. and Eisenbud, L. *Phys. Rev.* **72**, 29 (1947)

Wilson, W. M., Moses, J. D., Bilpuch, E. G. and Mitchell, G. E. *Nucl. Phys.* **A227**, 277 (1974)

Wimpey, J. F. *Electromagnetic Decay of Fragmented Analog States in ^{45}Sc and ^{65}Cu* . Ph. D. dissertation, North Carolina State University, 1974

Woosley, S. E., Arnett, W. D. and Clayton, D. D. *Astrophys. J. Suppl. ser.* **26**, 231 (1973)

Zaidi, S. A. A. and Darmodjo, S. *Phys. Rev. Lett.* **19**, 1446 (1967)

BIOGRAPHY

FANG DUFEI

Personal: Born November 16, 1956, Hunan, China

Married Wu Shiming January 1, 1984

Education: B. S. in Physics, University of Science and Technology of China, Hefei, China, 1981

M. S. in Physics, University of Science and Technology of China, Hefei, China, 1984

Positions: Teaching Assistant, 1981 – 1983

Research Assistant, 1985 – present (at TUNL)

Abstracts: "Levels of ^{32}S from High Resolution Proton Scattering"

D. F. Fang, C. R. Westerfeldt, E. G. Bilpuch and G. E. Mitchell, Bull. Am. Phys. Soc. **30**, 1769 (1985)

"Rayleigh Scattering from Atoms at Small Momentum Transfers"

D. F. Fang, X. W. Tang and B. Z. Yang, Fifth National Nuclear Physics Meeting of the Chinese Physical Society, Wuhan, 1984